HELSINGIN YLIOPISTO
HELSINGFORS UNIVERSITET
UNIVERSITY OF HELSINKI

Master's thesis
Department of Geoscience and Geography
Solid Earth Geophysics

SOUTHERN CONTINUATION OF THE SIILINJÄRVI CARBONATITE COMPLEX AT THE SIILINJÄRVI PHOSPHATE MINE IN FINLAND, BASED ON GEOPHYSICAL DATA

Bláthnaid McKevitt

November 2020

Supervisors:
Emilia Koivisto (University of Helsinki)
Pietari Skyttä (University of Turku)

UNIVERSITY OF HELSINKI
FACULTY OF SCIENCE
DEPARTMENT OF GEOSCIENCES AND GEOGRAPHY

PL 64 (Gustaf Hällströmin katu 2)
00014 Helsingin yliopisto

HELSINGIN YLIOPISTO
HELSINGFORS UNIVERSITET
UNIVERSITY OF HELSINKI

Tiedekunta – Fakultet – Faculty Faculty of Science	Koulutusohjelma – Utbildningsprogram – Degree programme Master's programme in Geology and Geophysics

Opintosuunta – Studieinrikting – Study track
Solid Earth Geophysics

Tekijä – Författare – Author
Bláthnaid Marie McKevitt

Työn nimi – Arbetets titel – Title
Southern continuation of the Siilinjärvi Carbonatite Complex at the Siilinjärvi Phospahte Mine in Finland, Based on Geophysical Data

Työn laji – Arbetets art – Level Master's thesis	Aika – Datum – Month and year 11/2020	Sivumäärä – Sidoantal – Number of pages 111

Tiivistelmä/Referat – Abstract
Phosphate is reported to be subject to "high supply risk" by the EU Commission (European Commission 2017). At present, the Siilinjärvi mine in Finland is the only mine in the EU producing phosphate. Optimising the productivity of the Siilinjärvi mine is crucial to address the demand for phosphate within the EU. The current production prognosis of the mine is to the end of 2035. To improve the prognosis of the mine, an exploration program is being undertaken to investigate the extent of the deposit and possible locations for new pits. The main area of interest is the area south of the current Särkijärvi pit. Exploration drilling is limited in this area due to obstacles created by infrastructure of the mine, including the factory area and gypsum pile. To address this, 3D passive source seismic, 2D active-source reflection seismic, Ground Penetrating Radar (GPR) and magnetic surveys were conducted at the Siilinjärvi mine site as part of the H2020 Smart Exploration project.

This study focuses on two of the acquired active-source seismic reflection profiles, SM2 and SM3. The aim of the study is to determine the depth and lateral extent southern continuation of the deposit in the area south of the Särkijärvi pit, next to the gypsum pile, and create a 3D model of the Siilinjärvi deposit based on the obtained results. In addition, obtaining information on waste rocks and zones of weakness, such as shear and fracture zones, is also of interest as this information is critical for mine planning. The main focus for seismic data processing was to improve the signal-to-noise ratio. Strong amplitude S-waves and unclear first-breaks were limitations found in the data. As a consequence, in addition to bandpass filtering, seismic line SM2 required a combination of attenuation and muting to supress the impact of S-waves. Seismic line SM3 had a lower data quality in comparison to that of SM2. The suppression of S-waves had a negative impact on the near-surface reflections along SM3 and therefore was not carried out. The GPR and magnetic data were processed using standard workflows.

The active-source seismic survey was successful in determining the depth and the lateral extent of the southern continuation of the Siilinjärvi deposit. A 3D model of the deposit was created based on the obtained seismic images. This model expands on the previous model and indicates that the carbonatite-glimmerite deposit expands towards the W, beneath the gypsum pile. This information can be used as a guide for future drilling in the area. In addition, information was obtained on zones of weakness and the waste-rock dike network. Sub-horizontal to gently dipping reflections observed in the seismic data were interpreted as diabase dikes. On a smaller scale, GPR measurements detected shallower near-surface features which are also interpreted to possibly be dikes. For some features, a correlation could be made between the various geophysical measurements. The carbonatite-glimmerite deposit was found to be associated with elevated magnetic total field (nT) values.

Avainsanat – Nyckelord – Keywords
Reflection Seismic, Mineral Exploration, Siilinjärvi phosphate mine, GPR, Magnetic, Carbonatite complex, Diabase Dike, 3D Model

Säilytyspaikka – Förvaringställe – Where deposited
HELDA- Digital repository of the University of Helsinki

Muita tietoja – Övriga uppgifter – Additional information
52 Figures and 7 Tables

TABLE OF CONTENTS

1. INTRODUCTION

1.1 Background of Study

Phosphate is listed as one of 27 critical raw materials (CRMs) for the EU and is reported to be subject to “high supply risk” by the EU Commission (European Commission 2017). At present, the Siilinjärvi carbonatite complex in Finland hosts the only mine in the EU producing phosphate. Open pit mining for phosphorus ore was commissioned in 1979 by Kemira OY. Since 2007, the deposit has been under the ownership of Yara International ASA, presently mining >10Mt of ore and producing approximately 1Mt of apatite concentrate per annum (O’Brien 2015). The Siilinjärvi mine is one of the largest open pit mines in Finland and is currently comprised of two pits: the Särkijärvi main pit (~250 m deep), and the Saarinen satellite pit (~60 m deep).

1.1.1 Exploration Activities at Siilinjärvi

The main application for phosphate is agricultural fertilizer, for which there is no recycled input and no possible alternative, therefore optimising the productivity of the Siilinjärvi mine is crucial to address this demand within the EU. To do this, exploration is conducted at the Siilinjärvi mine area in addition to the mining activities. An extensive drilling project was carried out at the mine between 2012-2015 to investigate the extent of the deposit. Based on the drilling results, Yara opted to open a new pit, Jaakonlampi, located north of the main pit. Production in the Jaakonlampi pit is set to start in 2021-2022. This pit will eventually progress to the south to merge with the Särkijärvi pit (Kaivosvastuu: Yara Suomi Oy, 2019). Production in the Saarinen satellite pit will cease in 2021, however with this extension, the current production prognosis of the Siilinjärvi mine is to the end of 2035. The goal for the future is to further investigate the extent of the deposit so that production can continue beyond 2035.

Drilling projects carried out in the Saarinen and Jaakonlampi mine areas proved to be a success by producing better estimates on the mill feed. Following on from this success, Yara Suomi Oy was granted a permit in 2015 to carry out exploration in the areas surrounding the Sillinjärvi mine. The exploration program includes the use of deep

drilling, geophysical measurements, and bedrock mapping (Kaivosvastuu: Yara Suomi Oy, 2019). The main area of focus for this exploration program is the area south of the Särkijärvi pit. The overall goal of the program is to determine the extent of the complex further towards the south and improve the knowledge on the lithological units and structures controlling the location of the mineralisation. Extensive drilling has already been carried out as part of this program. However, drilling locations are limited due to obstacles created by infrastructure of the mine, including the factory area and gypsum pile. Consequently, other means are required to map the southern continuation of the deposit and to guide the drilling efforts.

Geophysical measurements were conducted at the Siilinjärvi mine site in the Autumn of 2018 as part of the ongoing exploration program. The aim of this work was to further investigate the area south of the main pit and expand on the information obtained from drilling**.** The measurements were carried out as part of the Smart Exploration project (section 1.2). During the field work period of the Smart Exploration project, three 2D active-source seismic profiles, an in-tunnel active-source seismic profile and 3D passive source seismic data were acquired (Figure 1). Ground penetrating radar (GPR) and magnetic measurements were also collected during the field work period in southern part of the Särkijärvi pit and along seismic lines SM1 and SM2 by the University of Helsinki. Magnetic measurements along SM2 were collected by Uppsala University. The work presented in this thesis focuses on two of the 2D active-source seismic profiles: SM2 and SM3. In addition, the GPR and magnetic data acquired along seismic profile SM2 will be presented to complement the seismic data and aid in the interpretation. The overall objective of this study was to investigate the depth and the lateral extent of the southern continuation of the carbonatite complex at Siilinjärvi, with an end goal of creating a 3D model of the extension based on the data interpretation. Obtaining information on the waste rock network and any other structural elements present that might affect the future mine planning was an additional aim.

The work presented in this thesis is closely linked to the MSc thesis work carried out by Viveka Laakso, at the University of Helsinki (Laakso 2019). The basis of Laakso's work was testing the application of reflection seismics, GPR and magnetic methods for mineral exploration and mine planning at the Siilinjärvi mine. Imaging the sub-horizontal diabase dikes for mine planning was the main topic of interest. The area of focus for the study

was the southern end of the Särkijärvi pit, including active-source reflection seismic profile SM1 acquired by the Smart Exploration project (Figure 1). This survey line therefore acts as a good reference line for this study, and the results obtained along SM1 were compared with the results obtained from this study to aid the interpretation work. Furthermore, profile SM1 was used along with profile SM2 and SM3 when producing the final 3D model of the southern continuation of the Siilinjärvi deposit.

In addition to the acquisition of geophysical data, geological data was also acquired as part of the Smart Exploration work at Siilinjärvi. This work was conducted by Tuomas Kauti at the University of Turku. The first goal of Kauti's work was to produce a detailed 3D model on the waste-rock dike network within the Särkijärvi open pit. In addition to this, the geophysical results obtained at Siilinjärvi, including those which are presented in this thesis, will be used in conjunction with the geological data to produce a Common Earth Model, which will provide further information on the depth and lateral extent of the ore body and the diabase dike network south of the Särkijärvi pit.

1.1.2 Seismic Methods in Mineral Exploration

In hard-rock environments, the reflection seismic method has the potential to produce high-resolution images of the subsurface to depths exceeding the current maximum depth of mining, approximately 4 km (Manzi et al. 2015). Conventional surface geophysical methods, mainly potential field and electromagnetic methods, which have traditionally been utilised for mineral exploration are typically not capable of penetrating depths greater than 500 m in a hard-rock environment (Salisbury and Snider 2007). Smart Exploration project especially focuses on the development of seismic methods as well as electromagnetic methods.

The seismic reflection method utilises reflected waves which are produced at interfaces of contrasting elastic properties. The measured reflected waves can provide high-definition images of geological structures hosting mineral deposits. From previous studies, the method has proven to be effective for both mineral exploration and mine planning (Salisbury and Snyder 2007, Malehmir et al. 2012, Koivisto et al. 2015). For complex geological environments such as mining areas, three-dimensional surface

seismic surveys are ideal for imaging the subsurface structures. However, due to economic restrictions 2D surveys are often carried out as a more cost-effective alternative (Malehmir et al. 2012). Additionally, 2D surveys may be used in areas where terrain restrictions do not allow for a full 3D survey, as was the case in Siilinjärvi.

2D surveys are beneficial in the initial exploration stages for mapping the structures and contacts associated with or controlling the location of the mineral deposit (Malehmir et al. 2017). However, previous studies have shown (e.g., Pretorius et al. 2003) that the success of seismic surveys in hard-rock environments is site and geology- dependent. To date, there have been several successful examples of the application of seismic reflection methods for mineral exploration (Salisbury and Snider 2007, Kukkonen et al. 2012, Wright et al. 1994, Koivisto et al. 2015). Due to this, the use of seismic methods for mineral exploration is becoming more popular. There has also been an increase in the application of geophysics for mine planning, development and risk reduction (Pretorius et al. 2007). The first successful application of a 3D seismic survey for mine planning and development was conducted by Pretorius et al. (1997). This study successfully delineated a 3D structure of the reflective Ventersdorp Contact 'Reef' (VCR) gold ore body at depths ranging between 1000 to 3500 m. Following the success of this survey, there have been numerous applications of 3D seismics for mine planning (Pretorius et al. 2000, Malehmir and Bellefleur 2009 and Malehmir et al. 2012). Despite the overall potential of seismic methods for mineral exploration and mine planning, the methods are not routinely used by exploration and mining companies. One of the main reasons behind this is the relatively high cost associated with these surveys. However, this cost is lower in comparison to drilling costs and due to the superior depth of penetration of seismic methods, the data can be used to complement drilling and exploration programs. Another, perhaps more pressing reason is due to the complexity of seismic processing and the lack of expertise in exploration and mining companies.

1.2 Smart Exploration Project

Smart Exploration 2018-2020 is a Horizon 2020 project which is an EU programme for research and innovation. The overall focus of the project is the development of cost-effective, environmentally friendly tools and methods for geophysical exploration in

highly challenging brownfield areas (Smart Exploration 2020). An additional aim of the project is to test new innovative ideas for greenfield exploration to increase the potential of discovering new major deposits of relevance to the EU (Smart Exploration 2020). Smart Exploration consists of a multi-disciplinary consortium of research institutes, academics, SMEs, mining companies and civil society organisations. The project encompasses 27 partners from across Europe and 6 different test sites in Sweden, Portugal, Greece, Kosovo and Finland. As previously mentioned, the geophysical dataset discussed in this thesis is from the Siilinjärvi mine, which is one of the Smart Exploration test sites, located in eastern central Finland.

The Smart Exploration survey at Siilinjärvi mine site was performed during September-October 2018 (Figure 1). Due to numerous access constraints in the area (e.g. lakes, ponds and mine infrastructure), a site visit was conducted prior to the commencement of the survey in order to finalise the plans for data acquisition. As previously stated, during the fieldwork period at Siilinjärvi, three 2D active-source seismic lines, active source in-tunnel seismic data, passive seismic 3D data, GPR and magnetic data were acquired. The overall objective of the Smart Exploration study at the Siilinjärvi mine site was to determine the depth and lateral extent of the southern continuation of the Siilinjärvi carbonatite deposit. An additional aim of the survey was to test methods in order to obtain information on waste rock distribution and image subsurface structures such as faults and shear zones, which are essential for mine planning.

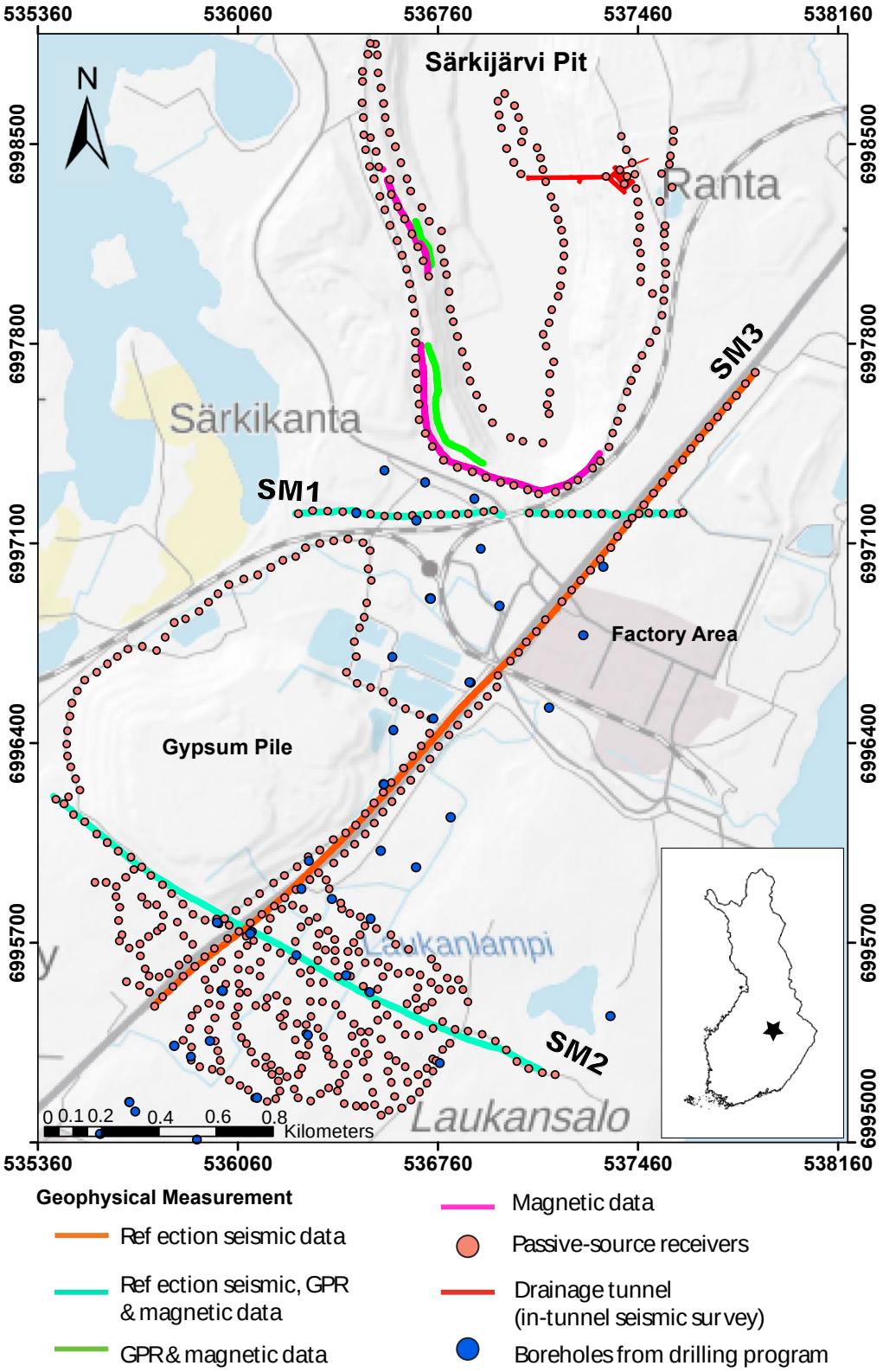

Figure 1. Location map of the Siilinjärvi mine site with the positions of the geophysical measurements acquired as part of Smart Exploration in Autumn 2018. Borehole locations from the ongoing drilling program are illustrated on the map. Coordinates are in the EUREF-FIN ETRS-TM35FIN system. Elevation data: Elevation model 2008-2019, 2 m x 2 m © National Land Survey of Finland.

One particular area of interest of this survey was the area beneath the Gypsum pile. The pile of gypsum (Figure 1), which is a by-product of phosphoric acid concentrate, covers an area of 2 x 1 km south of the main Särkijärvi pit. The central aim of the project is to map the continuation of the ore body beneath the gypsum pile, and in addition, any shallow fractures which could possibly be infiltrated by the highly acidic (pH <2) water from the gypsum pile (Da Col et al. 2019). To date, several research studies have been carried out on the Smart Exploration dataset acquired at Siilinjärvi. These studies include; surface-wave analysis based on the active-source seismic data (De Col et al. 2019), imaging of shear-zones from the in-tunnel seismic survey (Donczew 2019), suppression of surface-waves through seismic interferometry (Balestrini 2020), extraction of surface-wave dispersion curves from the collected ambient noise (Colombero 2020), illumination diagnosis retrieval of reflections from ambient-noise seismic data (Papadopoulou 2020) and testing of geophysical methods for mineral exploration and mine planning using 2D active-source seismic line SM1, along with GPR and magnetic data (Laakso 2019). In this thesis, the other two 2D active-source seismic lines will be discussed and additional GPR and magnetic data will be presented.

One of the additional goals of Smart Exploration is to develop and implement innovative approaches for mineral exploration with the aim of generating new technological and methodological markets and to obtain results that would allow for improved exploration in the EU and even further afield (Malehmir et al. 2019). As part of this, numerous prototypes are being developed. One of these prototypes is an Unmanned Aircraft Vehicle (UAV). As part of the Smart Exploration project, it is planned to use the UAV at the Siilinjärvi mine site to obtain magnetic measurements over the area. The magnetic data acquired at Siilinjärvi during the fieldwork period of this project will provide a source of reference for future work as the measurements will provide information on the magnetic signatures associated with the area.

1.3 Aims and Objectives of Study

The primary aim of this study is to investigate the depth and lateral extent of the Siilinjärvi carbonatite complex south of the current main pit (Särkijärvi pit). The planning of the future extension of the mine is a complicated task due to the presence of infrastructure

related to the mining operations (the factory area, gypsum pile and road network) south of the main pit. Therefore, the motivation behind this is to obtain information to aid in mine planning.

An additional aim of this study is to infer information on the waste rock network, as well as any other major structure which might affect the planning of the future mine. By obtaining a knowledge of the distribution and location of these features, excavation and extraction in the mine would be more efficient and safer.

To achieve these aims, the study had the following objectives:

- Utilise the seismic reflection method on two intersecting survey lines, to obtain information on the deposit to aid in the planning and guide the drilling efforts (which is required for resource estimation).

- Create a 3D model of the carbonatite-glimmerite deposit based on the obtained results.

- Conduct a GPR survey to aid in the interpretation of the seismic data by correlating the observed geological features with the surface geology.

- Utilise magnetic data to aid in the overall interpretation.

- Use surface geology, borehole lithology and rock quality information to interpret the geophysical results.

2 GEOLOGICAL BACKGROUND AND PREVIOUS WORK

2.1 Geological Background

The Siilinjärvi carbonatite-glimmerite complex is one of the oldest carbonatites on Earth (2601 ± 4 Ma) and is currently the oldest being mined for phosphorous. It is named after the village of Siilinjärvi, located 20 km north of the city of Kuopio in Eastern Central Finland. The complex is composed of a steeply dipping, north-south oriented tabular body that is approximately 16 km in length, up to 1.5 km in width and covers an area of 14.7 km^2 (Puustinen 1971). The main carbonatite-glimmerite intrusion is a central tabular body of carbonatite and glimmerite that runs the length of the complex and is approximately 900 m wide. The complex is intruding into the surrounding country rock, granite gneiss and is surrounded by a metasomatically produced fenite margin (Figure 2 & 3).

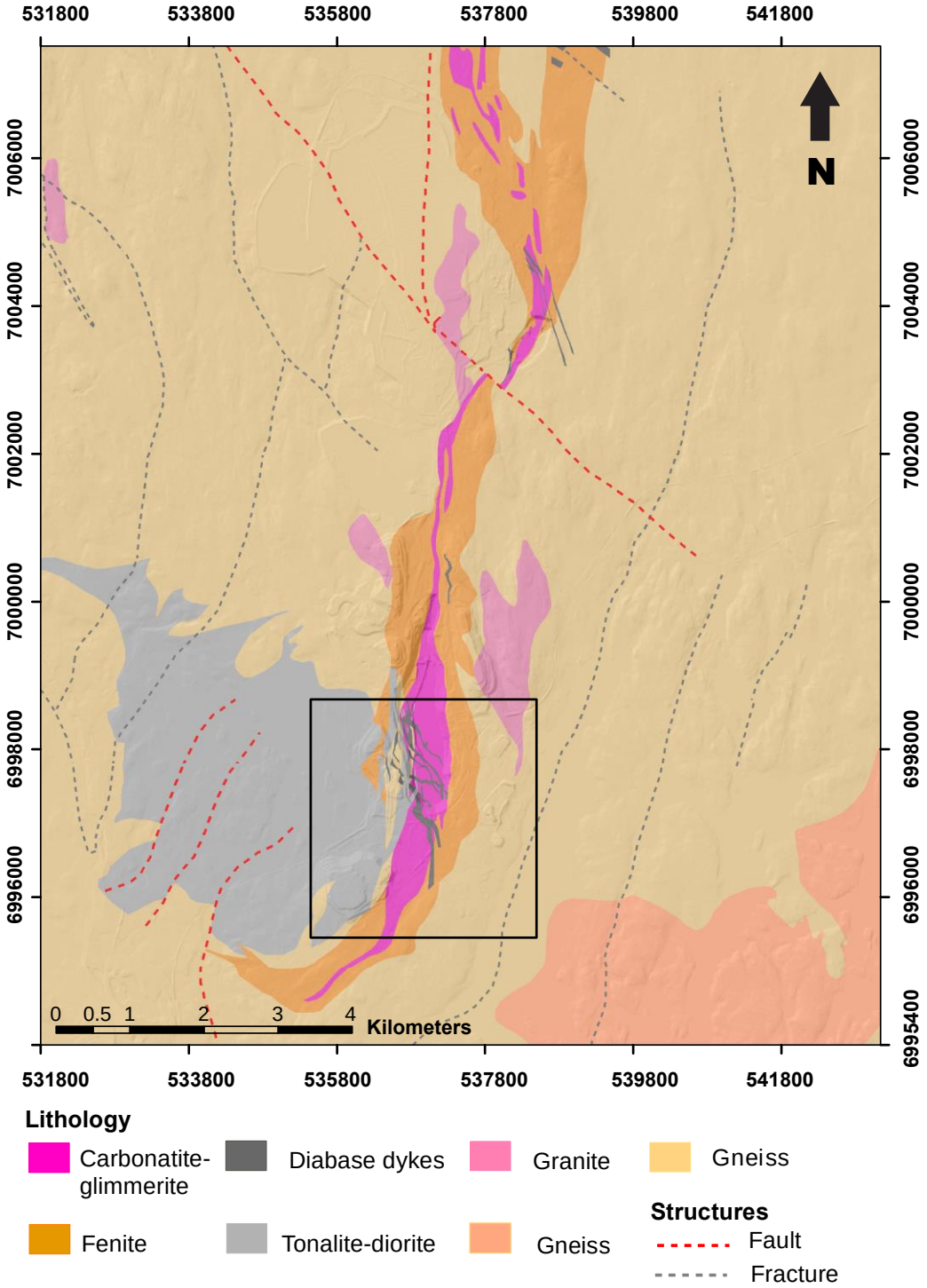

Figure 2. Geological map of the study area with a black box highlighting the location of the survey (Figure 3). Geological map of Finland, pre-quaternary 1:100 000, modified data © Geological Survey of Finland 2014. Structure data: Bedrock of Finland 1:200 000 © Geological Survey of Finland 2016. Base map: Elevation model 2008- 2019, 2 m x 2 m © National Land Survey of Finland.

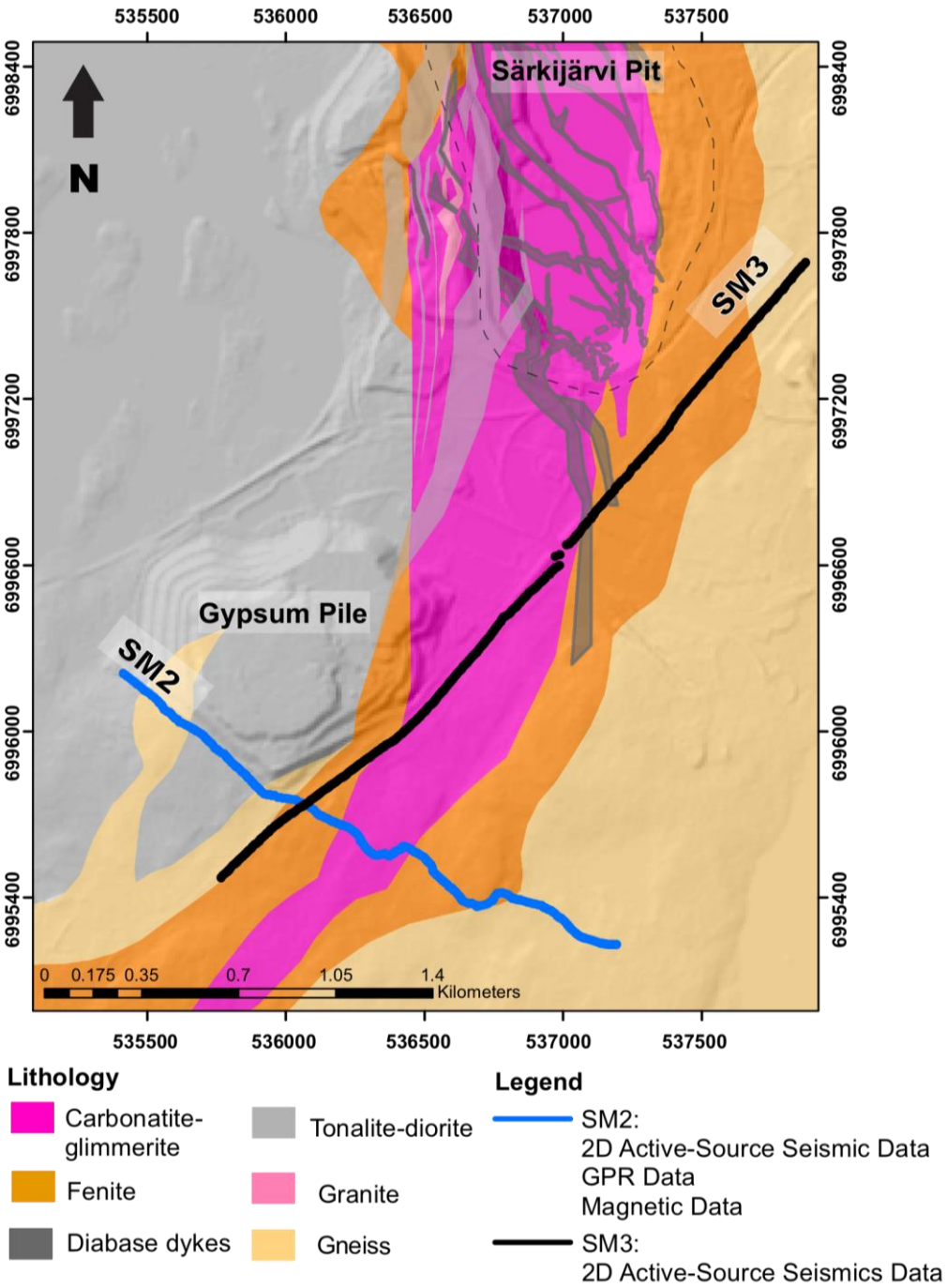

Figure 3. Geological map of the study area with the two survey lines discussed in this thesis. The location of the Särkijärvi pit is outlined with a dashed line. Geology information is from Yara. Base map: Elevation model 2008- 2019, 2 m x 2 m © National Land Survey of Finland.

The core of the Siilinjärvi complex is comprised of a large variety of mixed rocks which vary from glimmerite (phlogopite rock) to carbonatite (sövite). In addition to these, amphibole- and apatite-rich varieties also occur (Puustinen 1971). The carbonatites and glimmerites within the deposit are intimately mixed, varying between nearly pure glimmerites (tetraferriphlogopitites), to nearly pure carbonatites, with a well-developed

subvertical to vertical lamination. The complex is not strictly zoned, however generally the greatest volume of carbonatites is seen near the centre of the intrusion, which is cut by numerous subvertical carbonatite veins. Near the outer edges of the ore body, the glimmerites are nearly absent of carbonatite but still contain ore-grade amounts of apatite (Puustinen 1971). The average composition of the carbonatite-glimmerite portion of the complex is: 65% phlogopite, 19% carbonates, 5% richerite, 10% apatite and 1% accessory minerals (mainly magnetite and zircon) (O'Brien et al. 2015). Magnetite is the most common accessory mineral and is found in almost all varieties of the carbonatite-glimmerite rocks (Puustinen 1971). Mineralisation is known to continue to a depth of approximately 800m, based on several deep boreholes drilled in the area (Malehmir et al. 2017). The fenite halo encompassing the carbonatite-glimmerite intrusion formed as a result of metasomatism in the surrounding granitic and gneissic bedrock. This alteration was caused by the alkali fluids released during the formation of the intrusion (Carlsson 2020).

Contacts between the Siilinjärvi complex and the surrounding country rock are either primary magmatic or sheared, due to fracturing in the contact zone (Puustinen 1971 and O'Brien et al. 2015). For example, in the eastern part of the main pit the contact between the fenite and ore deposit is sharp and well preserved, whereas in the southwest corner of the pit, a mosaic of sheared blocks containing mingled tonalite-diorite, diabase, fenite and the carbonatite-glimmerite ore is observed (O'Brien et al. 2015).

The age of the Siilinjärvi carbonatite complex is a topic of debate. A number of studies have been carried out to investigate the age of the complex (Basu and Puusinen 1982, Bayanova 2006, and Zozulya et al. 2007). U-Pb analysis of zircon from the complex, measured by Kuovo (GTK unpublished report, 1984) reveals an age of 2610 ± 4 Ma, indicating that this complex is one of the oldest carbonatites on Earth. However, younger ages of 1785-2030 Ma and 1754-2031 Ma, respectively, have been obtained from K-Ar data (Puustinen 1971) and Rb-Sr isochron data (Tichomirowa et al. 2006), suggesting a Svecofennian origin.

The Siilinjärvi complex is intersected by a large number of dioritic and diabase dikes of varying width from a couple of centimetres to tens of meters. Diabase dikes intersect the intrusion and basement rocks in a NW-SE orientation. For mining, these dikes are waste

rocks and therefore locating these dikes is essential for mine planning. As previously mentioned, a study is being carried out currently as part of Smart Exploration by the University of Turku (Kauti et al. manuscript in preparation) to build a 3D model of the diabase dike network in the southern part of the Särkijärvi pit. The goal of the work is to provide information on the depth extent of the ore body by creating a Common Earth Model from the geological data and the geophysical data acquired as part of Smart Exploration.

2.2 Geophysical Background

2.2.1 Seismic Measurements

Malehmir et al. (2017) carried out a seismic survey in conjunction with a physical property study (see section 2.2.2) at Siilinjärvi in 2014. The seismic survey consisted of four seismic profiles with a total length of approximately 2.5 km, two of which were located inside the pit and two on its margins (Figure 4). The aim of the survey was to test the applicability of a microelectromechanical systems (MEMS) -based broadband seismic landstreamer for mine planning, by acquiring seismic profiles in combination with wireless recorders connected to 10 Hz geophones. For acquisition of streamer data, a source-receiver spacing of 2-4 m was used with a fixed geometry spread, whilst a spacing of 10 m was utilised for the wireless receivers. The combination of wireless and streamer data was advantageous as it increased the offset, allowing for deeper penetrations. As a result, imaging of the subsurface was achieved to a depth of 400-500 m. A Bobcat mounted drop hammer (500 kg) was the seismic source for the survey.

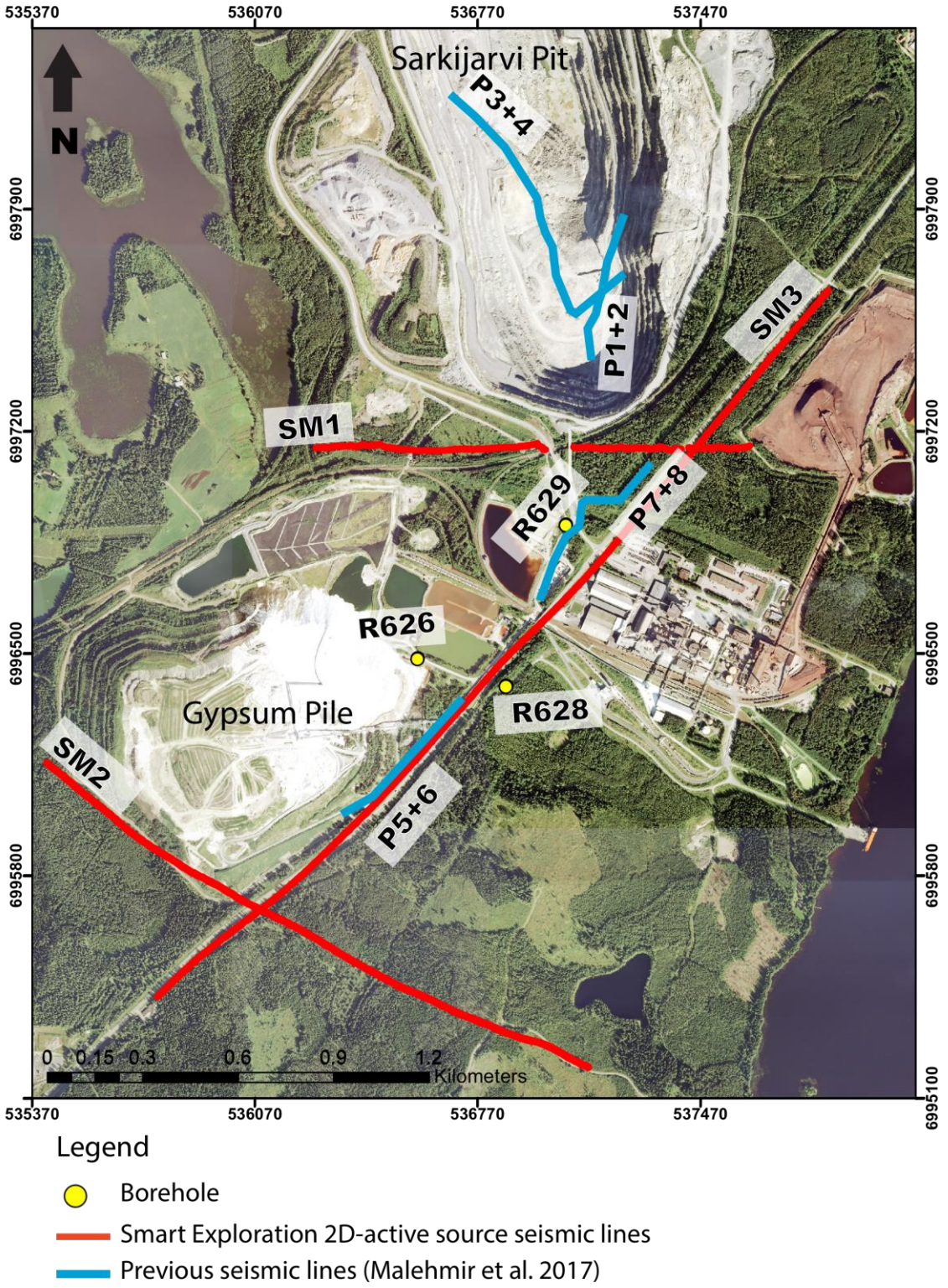

Figure 4. Aerial photograph map of the Siilinjärvi mine area with the location of the seismic survey and physical property measurements (three boreholes) acquired as part of previous work carried out in the area by Malehmir et al. 2017. The three 2D active-source seismic lines acquired as part of Smart Exploration during Autumn 2018 are also shown for reference. Base map: Aerial photography 2008- 2019, 2 m x 2 m © National Land Survey of Finland.

The data obtained by Malehmir et al. (2017), showed good-quality first arrivals. Due to the quality of the first arrivals, two processing methods were applied to the data: reflection imaging and travel-time tomography. For the reflection imaging method, a conventional processing flow was applied to the data, with the exception of migration which was not applied in order to preserve steep reflections. The observed reflections in the data showed a general south-west orientation and a dip angle of approximately 70° or more. Reflection imaging of the data was reported to be quite challenging due to the complexity of the near surface and the steeply dipping reflectors. The seismic velocity model created by the travel-time tomography processing method provided information on possible weakness zones in the survey area. Low-velocity depressions, approximately 40-50 m in thickness were observed. These depressions were interpreted as being possible weakness zones, for example fracture or shear zones.

Seismic profiles P5 + 6 (Figure 5) and P7 + 8 are of particular interest in relation to the work presented in this thesis due to the close proximity to the survey area (Figure 4). The interpretation of these profiles was largely based on the drill hole logs obtained from boreholes R626, R628 and R620 (Figure 7), which were located nearby. The reflectivity pattern, which was observed along both of the aforementioned sections, was interpreted as a being due to a series of low- and high-density diabase dikes, which were observed in the drill hole logs. A seismically transparent region was observed along P7 + 8 which was believed to represent an area of carbonatite-glimmerite (highly fractured). The low-velocity zone which is observed in the seismic tomography results does not show a clear connection with any strong reflections in the seismic sections. However, Malehmir et al. (2017) noted that this zone has a consistent dip with the observed reflections, possibly representing a weakness zone at a lithological contact or a water bearing diabase dike.

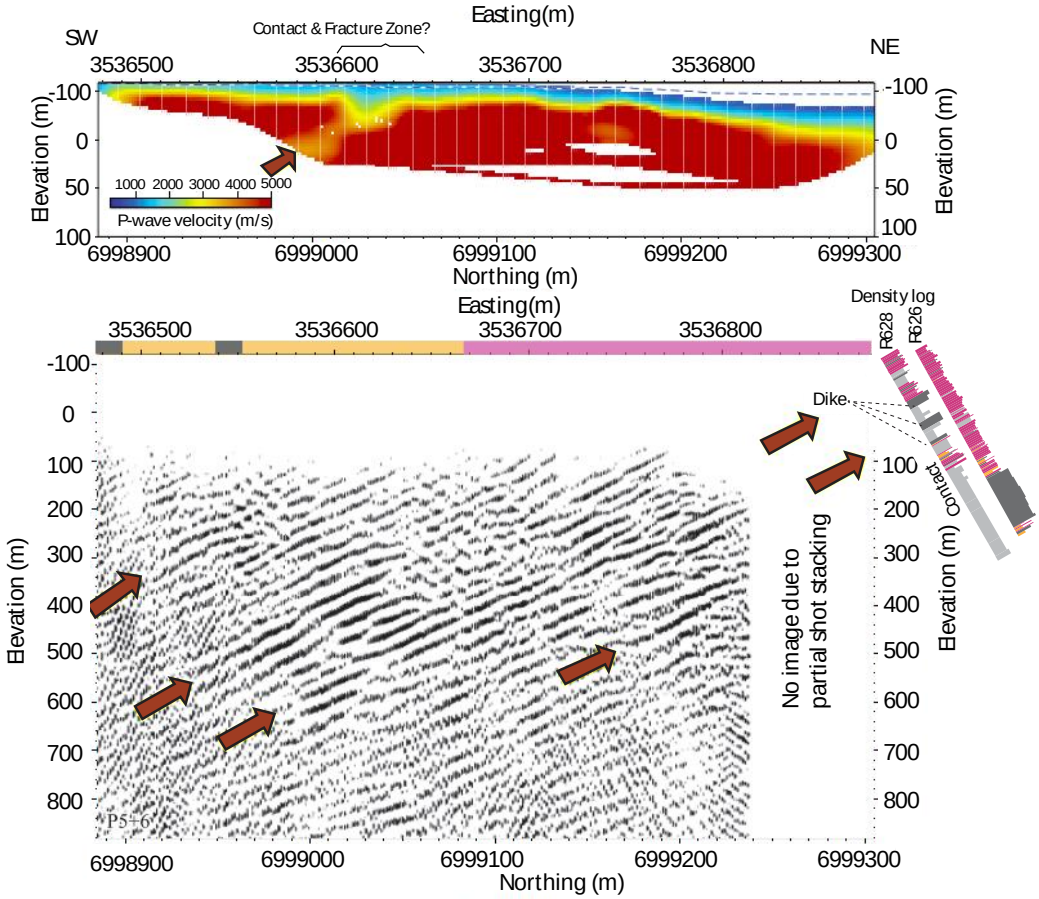

Figure 5. (a) Tomography results and (b) unmigrated reflection seismic stack obtained by Malehmir et al. (2017) along seismic profiles of P5 + 6 (see location in Figure 4). Results are showing a series of southwest-dipping reflections which are interpreted to be due to the presence of a sequence of diabase-diorite-carbonatite dikes which are observed in boreholes R626 and R628 (Figure 7). In the tomography results, a consistent dip is observed in the low-velocity zone and the reflections. The lack of information in the northwestern section of this profile is due to a partial (selected number of shots) stack being used for obtaining this section.

2.2.2 Physical Property Measurements

Seismic reflections may occur at interfaces of contrasting density and/or elasticity properties such as lithological contacts or shear zones. The occurrence of a reflection is dependent on the magnitude of contrast across the interface, specifically the contrast in acoustic impedance. Therefore, information on the physical properties of the geological material in the survey area is extremely important for understanding the nature of seismic reflections. Fortunately, in addition to the seismic measurements carried out by Malehmir et al. (2017) (see section 2.2.1), physical property measurements were also completed as part of the survey. By utilising the values obtained by this study, the expected seismic response at the lithological contacts in the area can be predicted.

The physical property study was carried out on 65 samples of an assortment of rocks that were collected from Siilinjärvi drill cores. Density, P-wave velocity and porosity measurements were carried out on each sample. The results showed a wide range of variations in the measured velocities and densities within each sample group (Figure 6). The measured P-wave velocities were in the range of approximately 4400 – 6500 ms^{-1}. Carbonatite-glimmerite and diabase dike samples were found to have the highest P-wave velocities, with the highest measured value being approximately 6500 ms^{-1}. However, these rock types also yield the largest range in P-wave velocity measurements. For diorite samples, P-wave velocity values were found to be in the range of 5400- 6500 ms^{-1} and for fenite samples, 5300-6200 ms^{-1}. In regard to the average P-wave velocity, fenite was found to have the lowest value, which was approx. 4850 ms^{-1}. Dioroite had the highest average P-wave velocity, ~5400 ms^{-1}. The large variations in velocities for each sample group may be due to a significant degree of fracturing in the rocks. Therefore, the measured velocities do not accurately represent the different rock types. Densities are less affected by fracturing and as a result, the density variation within each rock group is more distinct. The density of the samples was in the range of approximately 2500- 3050 kg/m^3. Fenite was found to be the rock group with the lowest density, with results ranging between approximately 2550 and 2700 kg/m^3. Samples of diabase were found to yield the highest densities, however the measured densities for this sample group varied greatly, with a density range of approx. 2700-3050 kg/m^3. The general conclusions made from the density measurements were that the fenite has the lowest densities and the diabase dikes yield the highest densities. Diorite and carbonatite-glimmerite samples show intermediate values. All samples were measured to have a porosity below 1.2%. In general, fenite was found to have the highest level of porosity, whereas carbonatite-glimmerite had the lowest.

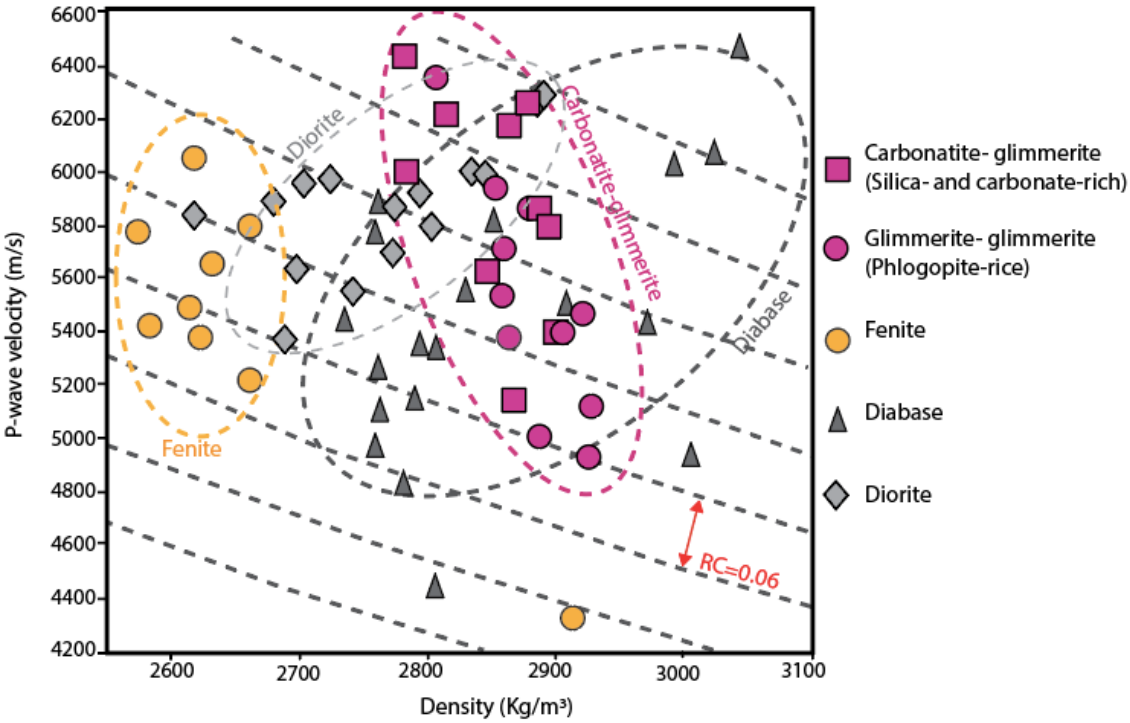

Figure 6. P-wave velocity and density measurements from a selection of drill core samples from the Siilinjärvi deposit obtained from the physical property laboratory study. Lines of constant acoustic impedance are shown on the plot and are separated by a reflection coefficient of 0.06. Plot is modified from Malehmir et al. (2017).

Downhole logging measurements were taken from three boreholes (R626, R628 and R629) located outside the main pit (see Figure 4). The holes were approximately 300m long and were drilled at a significant incline between 35° and 40°. Measurements were taken using the Robertson Geologging system and included triple full-waveform sonic, magnetic susceptibility, formation resistivity, temperature, fluid conductivity and natural gamma measurements. In addition, the cores were used for geologging, density measurements and rock quality studies (e.g., rock-quality designation [RQD] index). The data proved to be helpful for understanding the nature of geophysical anomalies by showing the locations of substantial changes in the physical properties.

The physical properties measurements (Figure 7) showed strong variations in density and P-wave velocities. The in-situ P-wave velocity measurements were in the range of approximately 2600-6000 ms^{-1}, with an overall average of approximately 5000 m/s for most rock types. Slightly higher values were measured for diabase and diorite. On average, carbonatite samples were found to have the overall lowest density and diabase dikes show the highest. Magnetic susceptibility values do not show significant fluctuations throughout the logs however, elevated values are seen to be associated with

carbonatites (due to fine-grained magnetite). This therefore suggests that a high-resolution ground magnetic survey may be useful for delineating the lateral extent of the mineralisation. Results also show that diorite is magnetically ‘stable’ and the contacts between diorite and other geological units is easily distinguishable in the magnetic measurements. Natural gamma measurements were also found to be relatively high for carbonatites and glimmerite and low for diabase dikes and diorite. No relation was seen between resistivity and rock type but based on rock quality studies, it was evident that the main control on resistivity is the degree of fracturing in the rock. Rock quality studies also indicated that fracture zones, if large enough, can be reflective due to the reduction in density and velocity.

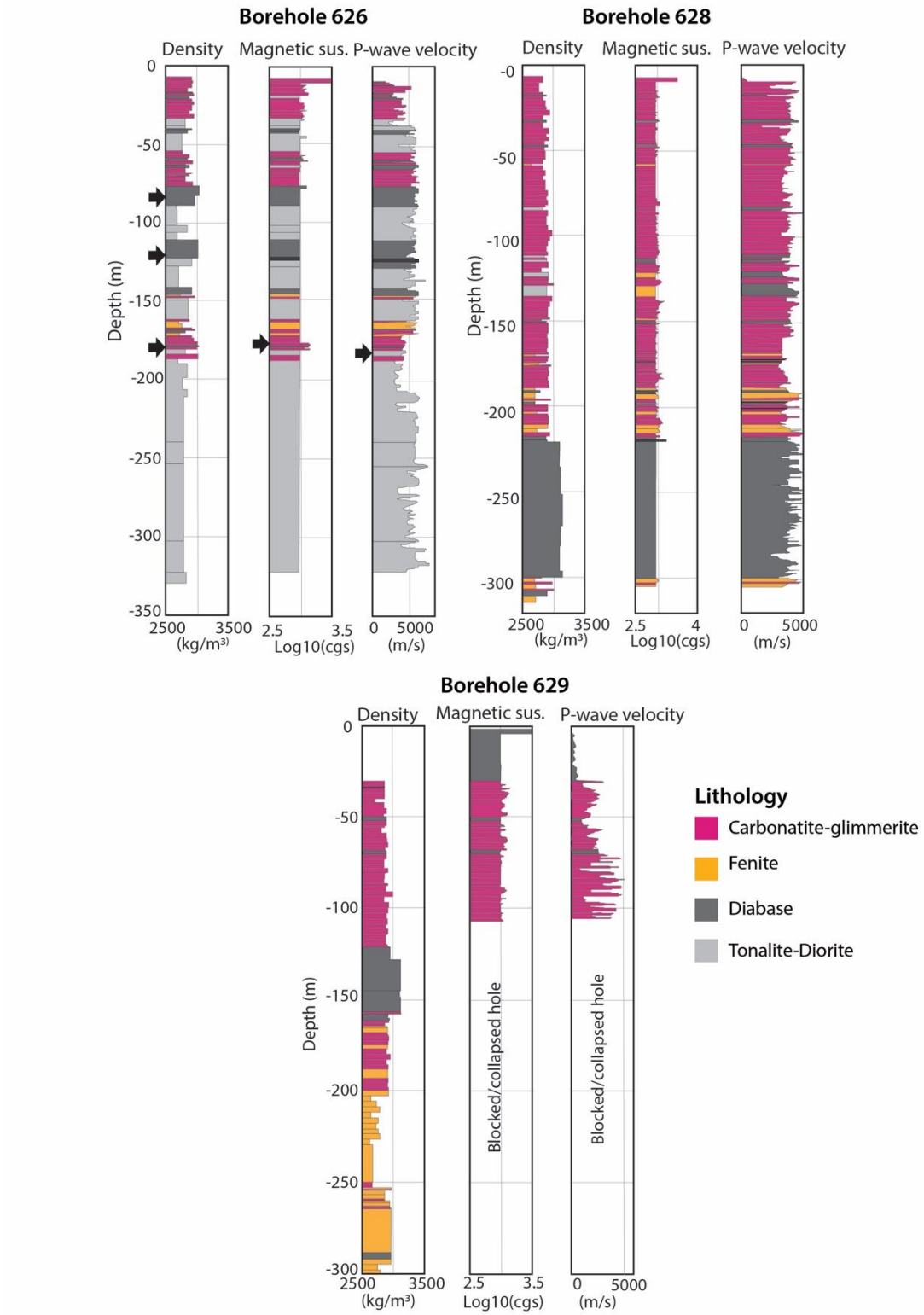

Figure 7. Results of magnetic susceptibility, P-wave velocity and density measurements and core logging carried out by Malehmir et al. (2017) from boreholes R626, R268 and R629 (locations shown in Figure 4). Downhole logging was limited to a depth ~100 m in borehole 629 due to a collapse/blockade. Black arrows indicate areas of reduced RQD. Modified after Malehmir et al. (2017).

2.2.3 Ground Penetrating Radar (GPR) Measurements

A GPR survey was carried out in the Siilinjärvi area in 2014 by Luoma et al. (2014) to determine the topography of the bedrock surface and characteristics of the overlying Quaternary sediment. 47 GPR lines were acquired throughout the survey area, including the main geological deposits and areas of mining activities (e.g. gypsum pile and calcine pile areas). The GPR survey was conducted using the Malå – Ramac ProEx Rough Terrain radar system with 25 MHz and 100 MHz frequency antennae. In addition to the GPR investigation, available hydrogeological data were utilised to aid in the interpretation of the GPR profiles.

The GPR survey was successful in most of the surveyed areas. However, in areas such as the gypsum area, the Quaternary overburden is mainly clay. The high electrical conductivity of the sediment in such areas resulted in poor depth of penetration of the radar. In the areas where the GPR survey was a success, a sharp contact between the bedrock surface and the overlying Quaternary sediments was observed.

Luoma et al. (2014), concluded that the thickness of Quaternary sediment in the area is fairly thin, varying between 1.05 to 17.7 m, with an average thickness of 2.30 m. It was established that the Quaternary sediments, mainly consisting of fine-grained till, covers approximately 60% of the total survey, while 11% is exposed bedrock and 13.8% is surface water. Fine-grained sediments such as clay, silt and peat are located in close proximity to areas of surface water and cover 8.3% of the total area.

In addition to the overburden-bedrock contrast reflections, reflections within the bedrock were also visible in some of the GPR scans. These reflections were not discussed in the report produced by Luoma et al. (2014) however, we tentatively interpreted them as being diabase dikes. Based on this, it was concluded that GPR measurements would be a beneficial addition to the Smart Exploration field campaign. The additional information on the shallow subsurface from GPR measurements could then be used to complement the seismic data.

2.2.4 Magnetic Measurements

As part of a long-term airborne geophysical survey conducted by the Geological Survey of Finland (GTK), geophysical data including magnetic, electromagnetic and gamma-ray spectrometric measurements were acquired country-wide (Airo 2005). Data was collected at a low altitude, between 30-40m and with a survey line spacing of 200m. The data coverage included high-resolution magnetic data across the entire Siilinjärvi area, results of which are shown in Figure 8.

As can be seen on the magnetic map, elevations in total magnetic field values coincide with the locations of the open pits of the Siilinjärvi mine. These elevations are due to the presence of magnetite in the carbonatite-glimmerite deposit. Magnetite is the most common accessory mineral of both the carbonatites and the glimmerites. The increased values associated with the deposit seem to extend south of the main pit and gypsum pile, possibly indicating a southern continuation of the complex. The highest magnetic anomaly values (approx. 600 nT) in the survey area are seen to be east of the main pit. This anomaly corresponds to the presence of a pile of burnt iron oxide.

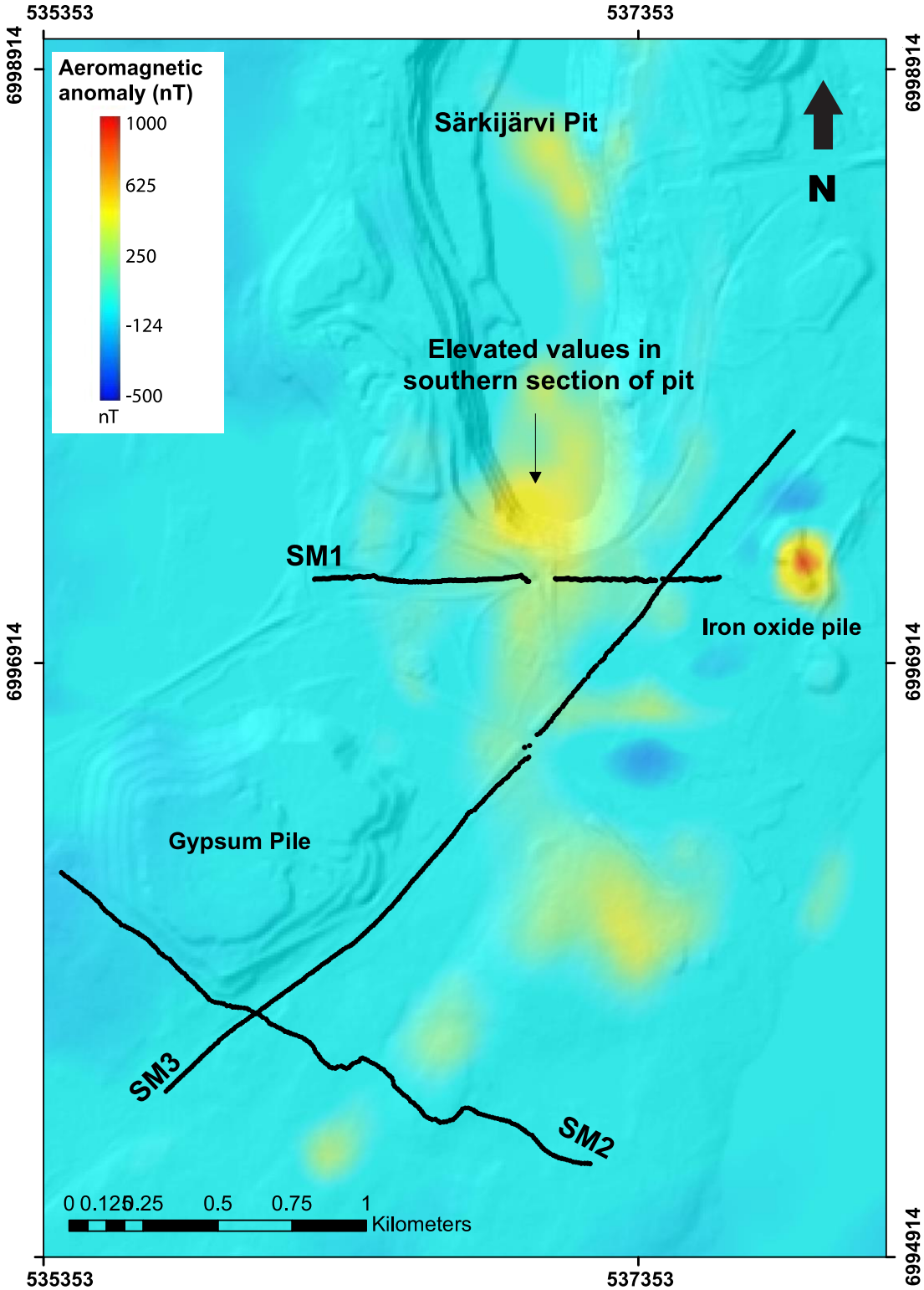

Figure 8. Low-altitude aeromagnetic anomaly map of the Siilinjärvi mine area. Locations of the 2D survey lines acquired as part of Smart Exploration are presented are shown with black lines. Coordinates are in the EUREF-FIN ETRS-TM35FIN system. Aeromagnetic anomaly map of Finland © Geological survey of Finland 2007. Base map: Elevation model 2008-2019, 2 m x 2 m, © National Land Survey of Finland.

3 2D REFLECTION SEISMIC METHOD

3.1 Fundamentals of the Seismic Reflection Method

3.1.1 Background Theory

Seismic methods are based on the behaviour of seismic wave propagation through the subsurface. The essential background theory of the seismic reflection method, specifically related to this study, will be presented in this section. Further discussion of the theory associated with the seismic method is presented by Sheriff (1995) and Yilmaz (2001).

A seismic wave is an elastic disturbance that propagates from point to point within a material. Events such as explosions or earthquakes generate seismic waves by releasing energy which propagates from the source through the Earth. There are several possible types of particle motion associated with wave propagation from an energy source. Body waves and surface waves are the two main types of seismic waves. Surface waves propagate along a boundary between two different media with contrasting physical properties. Surface waves are largest at the surface and decrease in amplitude with depth. Body waves travel through the elastic material in the subsurface as either compressional (P-waves) or shearing (S-waves) waves. Particle motion associated with P-waves occurs in the direction of wave propagation due to dilation or compressional strain. Whereas, S-waves, which are caused by pure shear strains, have particle motion that is aligned perpendicular to the direction of wave propagation. S-waves are made up of two components, SV-waves, which are vertically polarised S-waves and SH-waves, which are horizontally polarised S-waves. P-waves are the fastest waves and are the first arrivals in the recorded data.

The velocity of propagation and polarisations of motion of P- and S-waves can be derived from the relationship between stress, strain and displacement. The velocities of P- and S-waves are defined by the density ρ and elastic properties, i.e. Lamé's parameters λ and μ of a material. From the elastic wave equations for P- and S-waves in a homogenous isotopic solid, velocities can be derived by taking the divergence and curl of the equation of motion. The equation for P-wave velocity V_p is:

$$V_P = \sqrt{\frac{\lambda + 2\mu}{\rho}} \tag{3.1}$$

And the equation for S-wave velocity V_s is:

$$V_s = \sqrt{\frac{\mu}{\rho}} \tag{3.2}$$

P-waves are typically used for reflection seismic surveys. However, S-waves, being body waves, can also be used for reflection seismic studies. One advantage of using S-waves for reflection seismic studies, is that a higher spatial resolution can be obtained. Additionally, S-waves are more sensitive to fluids in comparison to P-waves, therefore information on pore fill could be obtained to enhance lithological studies. Nevertheless, reflection seismic studies most often utilize P-waves and S-waves are considered noise.

Seismic wavefronts propagate radially, expanding as they travel further from the source. The waves propagation can be understood with the Huygen's principle, (Sheriff 1995, p. 44) meaning that every point along the propagating wavefront is a point source for a new spherical wavefront. This principle explains how seismic disturbances are transmitted through the Earth and how future positions of the wavefront can be determined. As a consequence of the initial energy being spread over a larger area, the amplitude decreases with increasing distance (Reynolds 2011, p. 152). This dilution of amplitude is referred to as spherical divergence (Sheriff 1975, p. 127). The energy density *E* decreases as the inverse square of the distance travelled *r* and therefore, the amplitude *A* of the wavefront decreases linearly with the propagation of the wavefront. This can be expressed as:

$$E \approx \frac{1}{r^2} \ , A \approx \frac{1}{r} \tag{3.3}$$

Several other factors such as; absorption, peg-leg multiples, signal scattering and transmissivity losses, also impact the amplitude of propagating seismic waves (Sheriff 1975).

Absorption is a significant factor in relation to amplitude loss, and as waves propagate through the media, it eventually becomes the dominant factor. Absorption occurs as a

result of internal frictions within media. Absorption in relation to elastic waves in rocks leads to an exponential decrease in amplitude. This loss of amplitude due to absorption can be written as:

$$A = A_0 e^{-\eta x} \tag{3.4}$$

where A is the amplitude at a distance x away from the original amplitude, A_0 and η is the absorption coefficient. Absorption increases with higher frequencies.

3.1.2 Seismic waves at an interface

When a seismic wave reaches an abrupt change in acoustic impedance at an interface of two materials, reflected and refracted waves arise as a result. A portion of the energy from the incident wave is reflected back to the surface and a portion is transmitted through the interface as a refracted wave. When a P-wave hits a boundary, both reflected and refracted P- and S-waves are generated. The angles at which the reflected and refracted waves travel, are based on Snell's law (Figure 9). Snell's law can be expressed by:

$$\frac{\sin\theta_1}{V_{p_1}} = \frac{\sin\delta_1}{V_{s_1}} = \frac{\sin\theta_2}{V_{p_2}} = \frac{\sin\delta_2}{V_{s_2}} = p \tag{3.5}$$

where p is the ray parameter, which is the component of slowness of each ray parallel to the interface, θ_1 is the incident and reflection angle of the P-wave, θ_2 is the refraction angle of the P-wave. δ_1 and δ_2 are the reflection and refraction angles of the S-wave. V_{p_1} and V_{p_2} are the velocities of the P-waves in the two mediums (1 and 2) and V_{s_1} and V_{s_2} are the velocities of the S-waves in the two mediums.

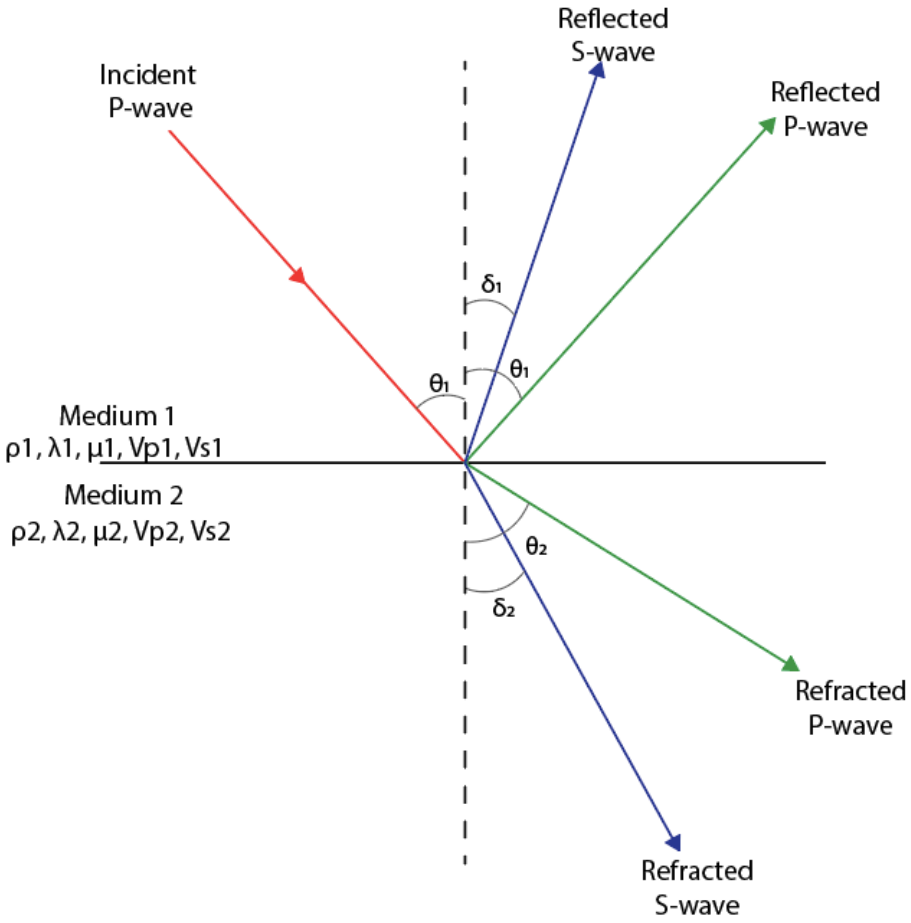

Figure 9. Reflected and refracted P- and S-waves resulting from a transmitted P-wave reaching an interface of two different mediums, where ρ_1 and ρ_2 are densities, λ_1, λ_2, $\mu_1$and $\mu_2$are Lamé parameters, Vp_1 and Vp_2 are the P-wave velocities and Vs_1 and Vs_2 are the S-wave velocities. θ_1 is angle of the incident P-wave and reflected P-wave, θ_2 is the angle of the refracted angle. δ_1 is the angle of the reflected S-wave and δ_2 is the angle of the refracted S-wave.

When a P-wave hits the interface at a critical angle, for which the angle of refraction is 90°, no refracted wave emerges through the interface into the second layer. Instead, the energy travels along the boundary of the two layers and back to the upper layer from each point along the boundary at an angle equal to the angle of incidence.

$$\sin i_c = \frac{V_1}{V_2} \tag{3.6}$$

Where V_1 and V_2 are the velocities of the two different mediums and i_c is the critical angle. For reflection seismic surveys, the arrival of these waves is important because they are the first arrivals (with the exception of the receivers closest the source where the direct

wave is the first to arrive) from the subsurface boundaries. These first arrivals are utilized in the processing of the reflection seismic data to carry out static corrections.

For reflection and refraction waves to be produced at an interface, boundary conditions must be satisfied. Stresses and particle displacements must be continuous over the boundary between the two media. Due to the boundary requirements, i.e. when both media are solids, four waves arise from the compressional (P-) incident wave; reflected P- and SV-waves and transmitted P- and SV-waves. When the incident wave is a SV-wave, four waves also occur as a result; a reflected and transmitted SV-wave and a reflected and transmitted P-wave. The SV-wave is converted into a P- and SV- reflection wave by mode conversion. However, in the case where a SH-wave is the incident wave, only two waves arise as a result; reflected and transmitted SH-wave.

The reflection and transmission coefficients of the produced waves are determined from a system of linear equations (Zeoppritz equations) resulting from the boundary conditions mentioned previously. The equations show that the reflection *R* and transmission *T* coefficients are dependent on the angle of incidence. Full derivations of the equations are presented in Shuey (1985), only the end result for a special case of normal incidence is presented in this thesis. For P-waves at normal incidence on an interface (i.e. vertical travel path), the Zeoppritz equations reduce to

$$R = \frac{V_2\rho_2 - V_1\rho_1}{V_2\rho_2 + V_1\rho_1} = \frac{I_2 - I_1}{I_2 + I_1} = \frac{A_1}{A_i} \tag{3.7}$$

$$T = \frac{2V_1\rho_1}{V_2\rho_2 + V_1\rho_1} = \frac{2\,I_1}{I_2 + I_1} = \frac{A_2}{A_i} \tag{3.8}$$

where ρ_1 and ρ_2 are the densities and V_1 and V_2 are the velocities of the two media. I_1 and I_2 are the acoustic impedances of the materials. Acoustic impedance is the product of density and velocity, ρV, of a material. Therefore, the relative amplitudes of the reflected and transmitted waves are dependent on the contrast in the acoustic impedances of the two materials. A_i is the amplitude of the incident wave, A_1 is the amplitude of the reflected wave, and A_2 is the amplitude of the transmitted wave. The level of the contrast determines

if the reflected and transmitted waves will be visible or not. In general, reflection coefficients are in the range of +1 to -1. The sign specifies the polarity of the reflected wave. A reflected wave which has a reflection coefficient of approximately zero, will have an amplitude which is too weak to be visible. Larger reflection coefficient values produce higher amplitude reflections. Salisbury et al. (1996) estimated that for most hard-rock environments an impedance difference of 2.5 x10^5 g/cm^2 s, which corresponds to a reflection coefficient value of 0.06, is the minimum value required to produce a detectable reflection.

Detection of a reflector also depends on the geometry of the reflector. Resolution of the survey is the ability to differentiate between two adjacent features. This depends on the distance between features in comparison to the wavelength.

Vertical resolution is the minimum vertical distance between two interfaces to show as separate reflectors (Sherrif et al. 1975), meaning that thinner layers ($h < h_{min}$) can be detected, but the thickness of the layers cannot be determined from the data.

$$h_{min} = \frac{V}{4f_d} \tag{3.9}$$

where V is the seismic velocity and f_d is the dominant frequency of the seismic wave.

Horizontal resolution is the minimum separation d_f required between two horizontal features for them to be imaged as separate planar reflecting surfaces. For unmigrated seismic data, the Fresnel zone is often taken as the minimum horizontal resolution.

$$d_f = \frac{2zV}{f_d} \tag{3.10}$$

where z is depth, V is the velocity and f_d is the frequency. A reflector with dimensions smaller than the Fresnel zone will act as a diffracting point, causing energy to scatter and the amplitude of the reflection to diminish (Sheriff et al. 1995).

3.1.3 Seismic Reflection Method

The seismic reflection method involves the use of an energy source such as dynamite or a seismic vibrator (Vibroseis), to generate seismic waves. A network of geophone receivers is deployed on the surface to detect any reflected energy which is recorded and saved for future processing. The amplitude of the recorded reflections is dependent on the reflection coefficients of the subsurface interfaces (as discussed in section 3.1.2). Two-way travel time is the time required for a seismic wave to travel from the source at the surface, through the subsurface to a reflector and back to the receiver on the surface. In seismic surveys, the distance x that separates the source and receiver, the offset, has an impact on the arrival times of the reflected waves. In a survey where the position of the source is changed to different locations along the survey line, the same reflection point in the subsurface is detected by different source-receiver pairs. This common reflection point is referred to as the Common Depth Point (CDP). For horizontal reflectors, CDP is equivalent to the point on the surface which is half way between the source and receiver, referred to as the Common Mid-Point (CMP) (Figure 10). In the case of a dipping reflector these terms are not equivalent to one another, regardless of this the terms are often used interchangeably. Seismic data can be sorted by grouping together traces which have the same midpoint location to form CMP gathers that collect recordings that sample the same subsurface reflection points. Offsets vary for each trace within a CMP gather. This impacts the two-way travel time associated with the individual traces due to the offset dependence of the travel-time. CMP gathers are corrected so that each trace represents a zero-offset recording. This correction is referred to as the Normal MoveOut (NMO) correction, it is discussed in more detail in section 5.2.4. Recordings of each CMP gather are then summed together to create a CMP stack. This is an effective way for improving the signal-to-noise ratio of the data.

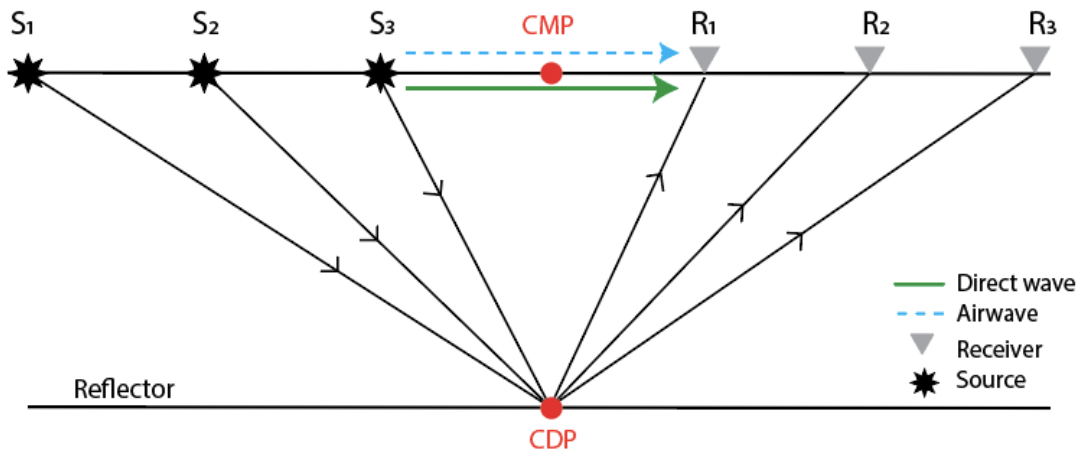

Figure 10. Diagram showing a reflection seismic survey. Sources and receivers located on the surface are illustrated in the drawing. The ray paths of reflected waves are also shown in the diagram along with the common mid-point and common depth point of the waves. The airwave, which travels through air from source to the nearest receiver and the direct wave, which travels from source to receiver through the ground, are also presented.

3.2 Acquisition of Active-Source Seismic Data at Siilinjärvi

Three active-source seismic profiles were acquired at Siilinjärvi as part of the Smart Exploration project. This thesis focuses on two of these profiles, SM2 and SM3. The other seismic profile, SM1, is presented by Laakso (2019).

Seismic profile SM2 is located south of both the main pit and the gypsum pile, running in NW-SE direction (Figure 11). The total length of SM2 is approximately 2.2 km and the elevation of the line is in the range of approximately 110-142m above sea level. SM2 perpendicularly crosses the carbonatite-glimmerite deposit, in addition to crossing other known geological units such as fenite, gneiss and the tonalite-diorite intrusion (Figure 18). Several known diabase dikes are also crossed.

Seismic profile SM3, located south of the main pit and SE of the gypsum pile, runs alongside the national road 75 (Figure 11). The total length of the line is approximately 3.0 km and is oriented in NE-SW direction. Elevation along the line ranges between 99 to 122m above sea level. As can be seen on Figure 18, the profile cuts through the carbonatite-glimmerite ore deposit. As is the case with seismic line SM2, SM3 crosses over other known geological units including fenite, gneiss, the tonalite-diorite intrusion

and several known diabase dikes. Both seismic profiles overlap one another, crossing south of the gypsum pile along the road. A summary of the survey parameters is shown in Table 1.

Table 1. Survey parameters for the 2D active-source seismic lines SM2 and SM3 (Figure 10)

Survey parameters	**Value**	
Acquisition type	2D Active-source seismic survey	
Acquisition system	Sercel Lite 428 (GPS time stamping/sampling)	
Spread type	Fixed spread	
	SM2	**SM3**
Profile length	2.03 km	3.06 km
Receivers	140 wireles, 81 cabled	138 wireless, 168 cabled
Source	Explosives	Explosives & drop hammer
Offset range	Max offset 2032 m	Max offset 3064 m
Nominal CMP fold	111	153
Active Channels	221	306
Recording length	30 sec	30 sec
Sampling interval	1 ms	1 ms
Receiver parameters		
Receiver interval	10m	
Geophone type	10 Hz	
Cabled receiver type	Sercel Lite^{TM} (Uppsala University)	
Wireless receiver type	Sercel UNITE	
Source parameters		
Source	Explosives & Drop hammer	
Source interval	20 m	
Dynamite charge weight	125 or 250 g	
Shot hole depth	~2.5 m	
Bobcat Weight	520 kg	
Bobcat source pattern	4 to 5 records per source location	
Calculated (theoretical) survey resolution ***(using velocity range of 5000ms^{-1} and 60 Hz frequency)***		
Horizontal resolution	200 m at 250 m depth, 290 m at 500 m depth and 500 m at 1.5 km depth	
Vertical resolution	0.8- 1.1m	

The acquisition system used for the survey are all owned by Uppsala University. 10 m receiver spacing was implemented for both lines and a 10 Hz geophone was used at each location (Figure 12). Data was recorded using a combination of both cabled receivers (with the SercelLiteTM system) and wireless receivers (part of the UNITE, cable-free system from Sercel (2020)) (Figure 11). Along SM2, 140 wireless and 81 cabled recorders were utilized to record the data (221 receivers in total along the line). For SM3, 138 wireless and 168 cabled receivers (306 in total) were used.

Due to access restrictions such as railway tracks and roads, crooked line geometry was used for both lines. Wooden pegs were used as station flags for each receiver and shot location. A high precision GPS was employed to record the coordinates of each of these locations.

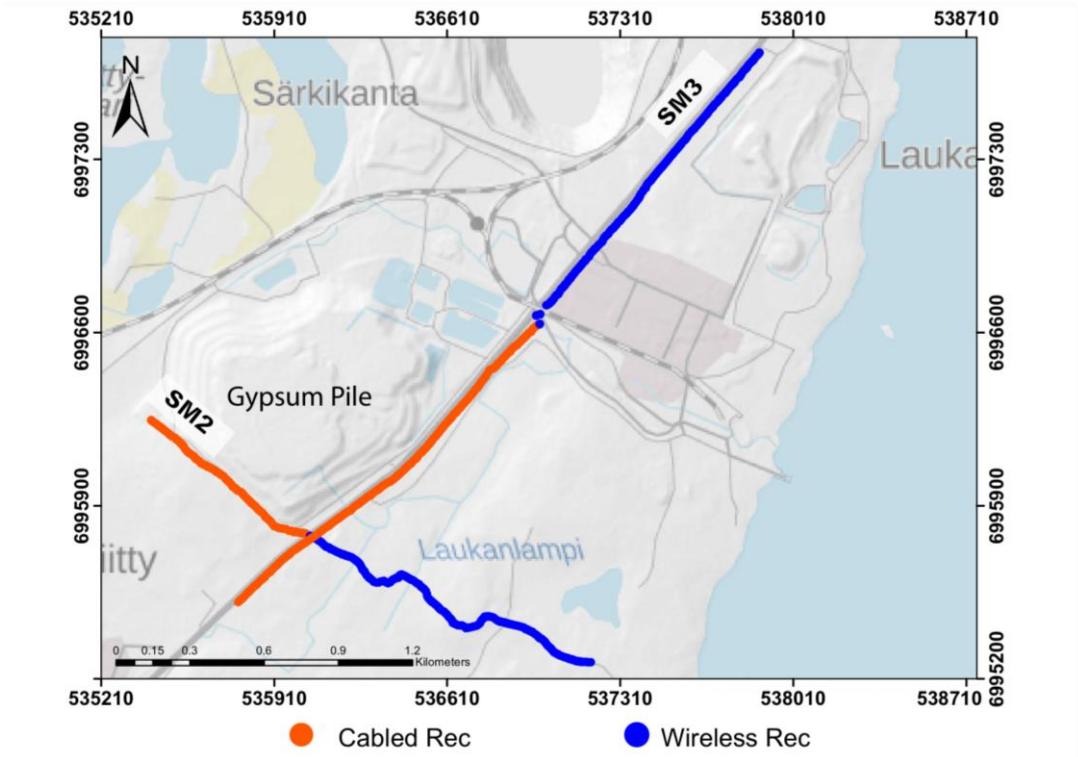

Figure 11. Locations of receiver type (cabled and wireless) used for the 2D active-source seismic surveys along survey lines SM2 and SM3. Coordinates are in the EUREF-FIN ETRS-TM35FIN system. Elevation data: Elevation model 2008-2019, 2 m x 2 m © National Land Survey of Finland. Basemap: © National Land Survey of Finland.

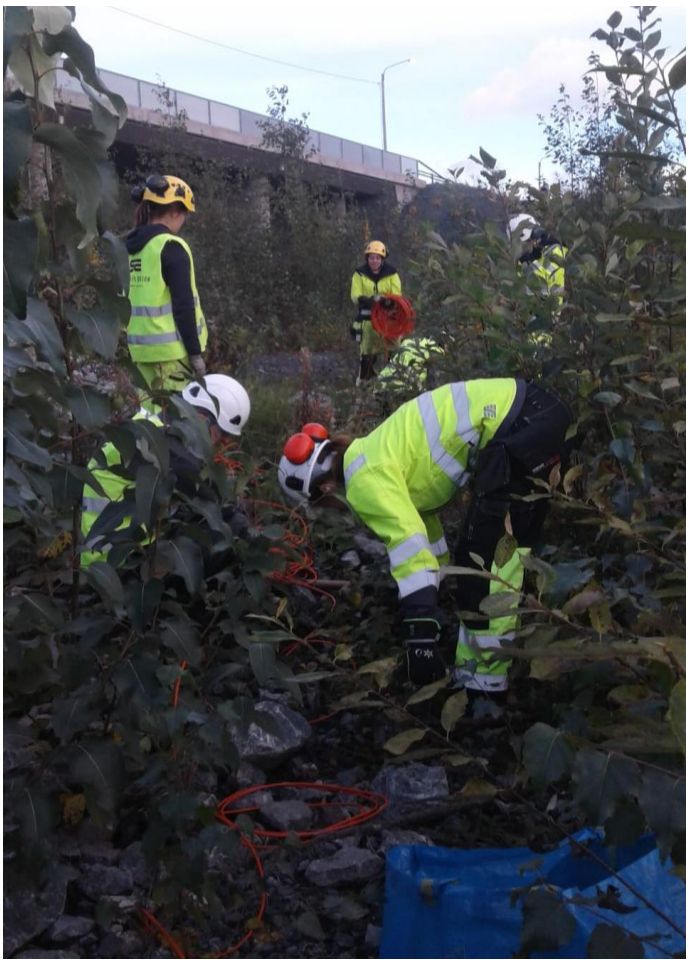

Figure 12. Example field photograph of Smart Exploration team setting up the Uppsala University Sercel LiteTM cabled receiver system.

Explosives were primarily used as the seismic source for both SM2 and SM3. 20 m spacing was used for source locations. Dynamite with a charge size of 250 g was detonated in holes at approximately 2-3 m depth using Orica's blasting device and Uni Tronic TM 600 detonators (Orica Limited 2020) (Figure 14). 102 explosive shots were used along SM2, and 128 were used along SM3. In addition to explosive shots, 24 drop hammer shots (520 kg) were used along SM3 in areas unsuitable for explosives (Figure 13).

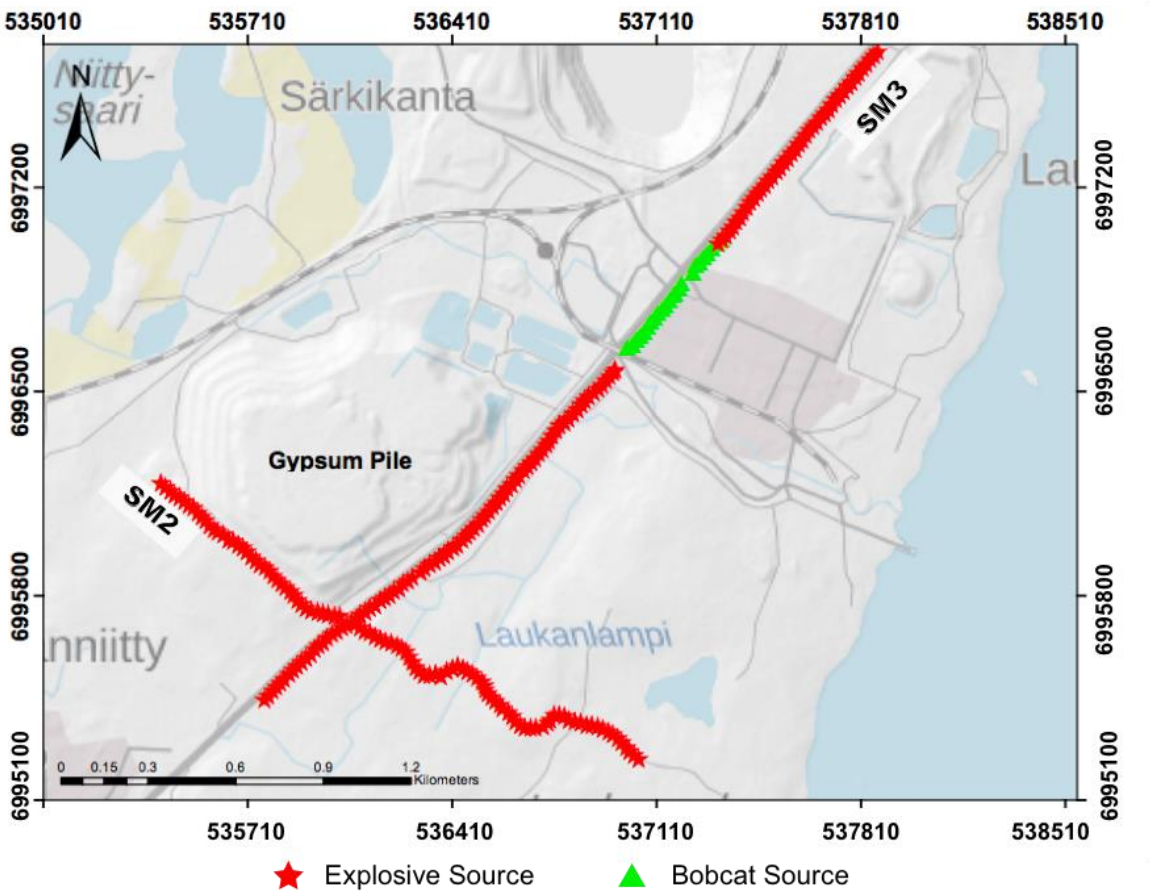

Figure 13. Locations of sources (explosive and bobcat drop-hammer) used for the 2D active-source seismic surveys along survey lines SM2 and SM3. Coordinates are in the EUREF-FIN ETRS-TM35FIN system. Elevation data: Elevation model 2008-2019, 2 m x 2 m © National Land Survey of Finland. Basemap: © National Land Survey of Finland.

The Bobcat-mounted hammer, owned and operated by Uppsala University, was used to generate 4 to 5 shot records during a 30 second recording time (Figure 14). Shots were later vertically stacked to increase the signal-to-noise ratio. In two source locations, the drop hammer and explosives were used so that the acquired data could be compared.

Figure 14. Example field photographs showing the sources used for the active-source seismic survey Left: Members of the Smart Exploration team operating Orica's blasting device for detonating explosive source. Right: Bobcat-mounted drop-hammer (from Uppsala University).

Seismic Data Processing

Seismic data acquired in hard-rock environments requires extensive processing. It is a lengthy process involving multiple steps. The objective of data processing is to reduce or remove unwanted components in the data, and to enhance the signal-to-noise ratio to obtain a clearer image of the subsurface. The software GLOBE Claritas (GLOBE Claritas, 2020) was used for processing the seismic data acquired from Siilinjärvi. The processing steps which were carried out on seismic lines SM2 and SM3 are presented in a processing workflow (Figure 15). The main processing steps that were applied will be discussed in this section. For further detail on seismic data processing see Yilmaz (2001) and Sheriff (1995).

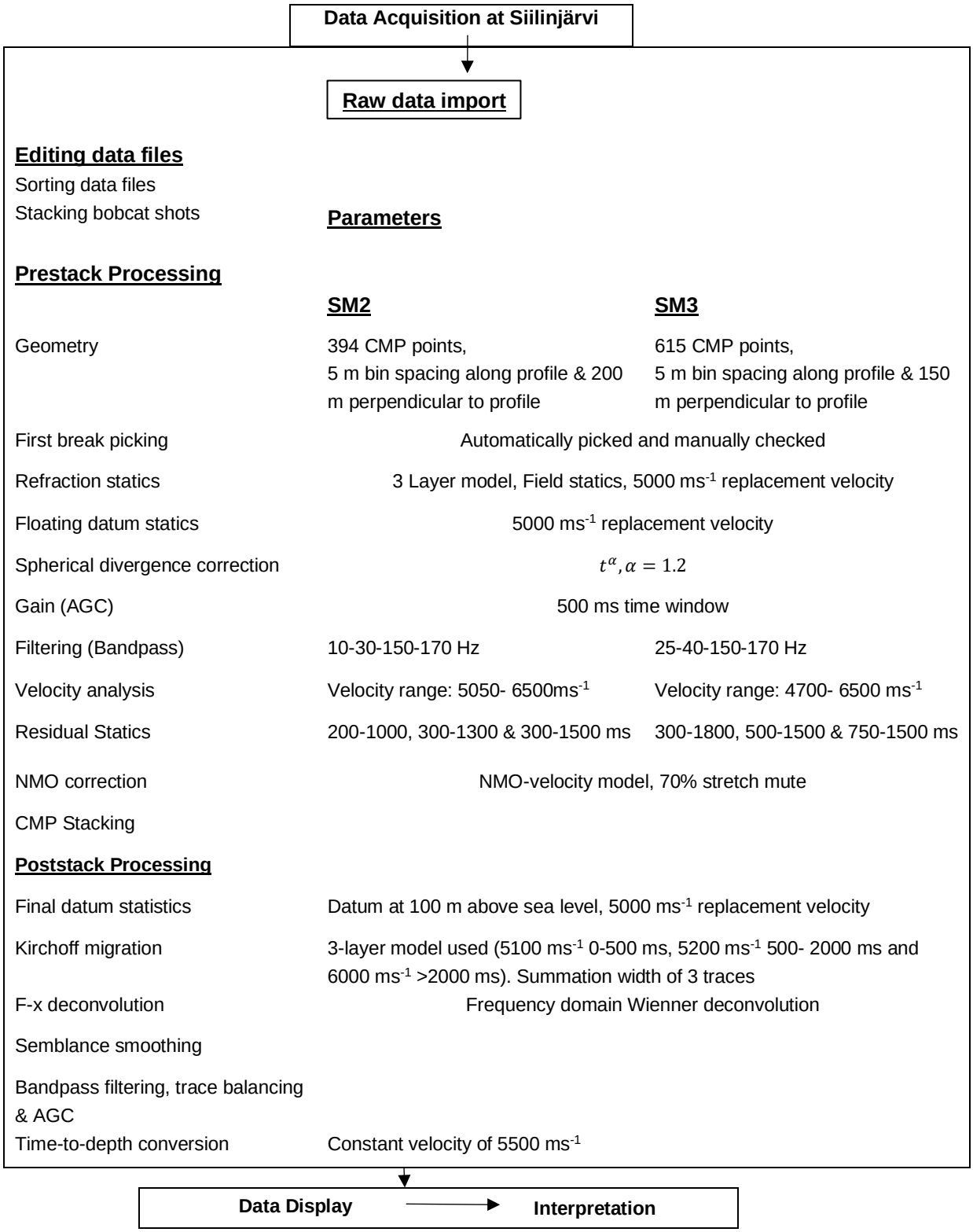

Figure 15. Processing flow applied to the seismic data (SM2 and SM3).

The raw seismic data from both seismic profiles, SM2 and SM3, contained traces with excessive noise and traces that were dead/zeroed. To test and compare the performance

of the sources used in this survey, explosives and drop-hammer sources, both were used at the same shot location along SM3. This was done at three different locations to ensure the analysis was validated. In the raw explosive shot gathers (Figure 16), first-breaks, S-waves, surface waves and air waves are all clearly visible. In drop-hammer shot gathers (Figure 17), first-breaks are weaker and less distinguishable, S-waves appear as the most dominant arrivals and air waves are not visible. Drop-hammer shot gathers show a lower signal-to-noise ratio in comparison to explosive shot gathers.

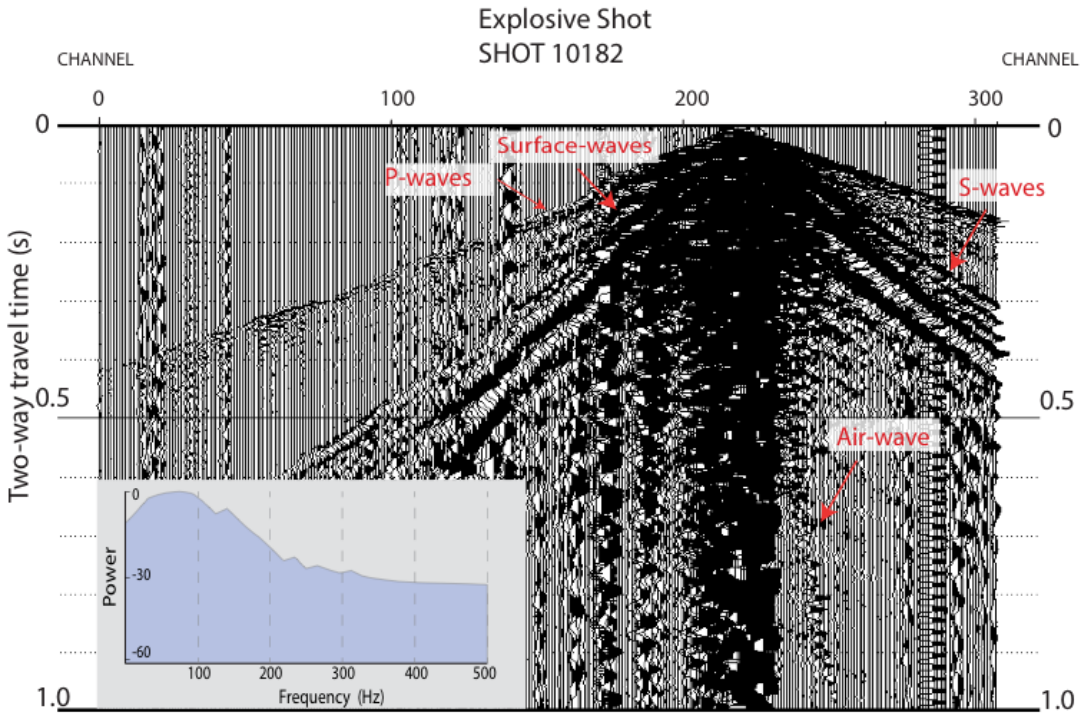

Figure 16. Shot gather from explosive source acquired along SM3 with amplitude spectrum. Bobcat drop-hammer source was also used in this location to test and compare the two types of sources (Figure 17).

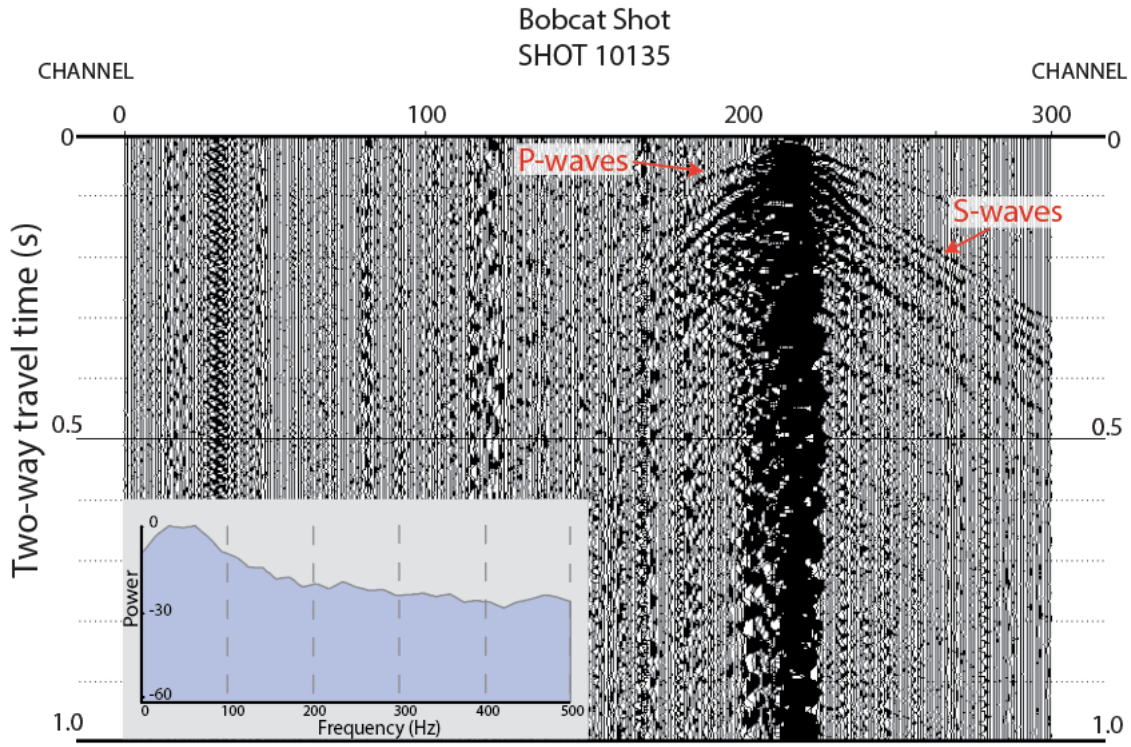

Figure 17. Shot gather from bobcat drop-hammer source acquired along SM3 with amplitude spectrum. Explosive source was also used in this location to test and compare the two types of sources (Figure 16).

As can be seen in the amplitude spectrums shown in Figure 16 and 17, the drop-hammer source generates more high frequencies. The frequency band for the drop-hammer source is wider in comparison to that of the explosive source and has a flatter spectrum.

3.2.1 Geometry and Static Corrections

Prior to processing the raw seismic data, the recording geometry of each seismic line was added to the datasets. To add geometry, information on the survey set up was required. This included information on; coordinates of the sources and receiver locations, Field File ID (FFID) numbers, and active channels. This geometry information was utilised to create seismic processing lines (or CMP/CDP lines) (Figure 18).

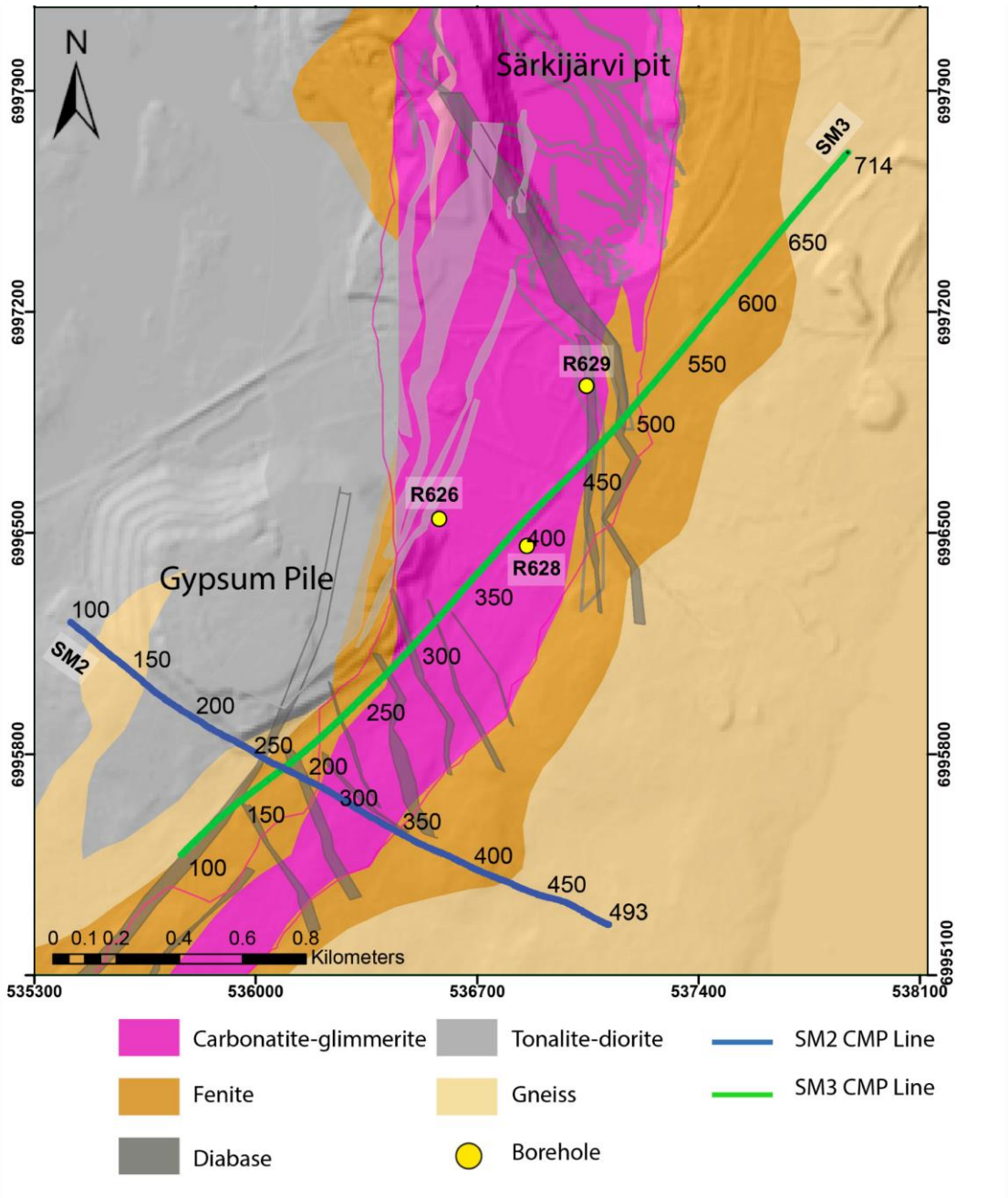

Figure 18. CMP lines created for processing seismic lines SM2 and SM3 overlain on a geology map. SM2 processing line consists of 394 CMP points in total (ranging from 100 to 493) with a spacing of 5m between points. SM3 processing line consists of 615 CMP points in total (ranging from 100 to 714) with point spacing of 5m. Locations of boreholes used in the physical property study by Malehmir et al. 2017 are also displayed on the map. Coordinates are in the EUREF-FIN ETRS-TM35FIN system. Geology provided by Yara. Basemap: © National Land Survey of Finland.

The geometry created for SM2 had 393 CMP points with 5 m bin spacing. The bin spacing perpendicular to the line was 200 m. All 22,542 traces fitted into the bins. The processing line created for line SM3 had 615 CMP points with 5 m bin spacing. The bin spacing perpendicular to the line was 150 m. All 46206 traces fell within the bins. The CMP geometry for both lines were then applied to the data.

Static time shifts (elevation, refraction and residual static corrections) were applied to the data to compensate for time delays caused by variations in topography, near surface heterogeneities and varying thickness of the low-velocity weathering layer. The objective of the long-wavelength static corrections were to determine the arrival times of reflections if all measurements were acquired on a flat plane (i.e. with no weathered or low-velocity layer present) (Yilmaz, 2001). This prevents near surface variations from possibly distorting or obscuring the reflected signals and therefore, increases the quality of the data. These corrections were applied to the data after the geometry was applied. Any remaining shorter-wavelength misalignments were removed by applying residual reflection-static corrections prior to stacking.

Refraction-static corrections were derived from the inversion of near surface velocity models based on first-break tomography. First-arrivals are associated with the head wave which travels at the interface of the near-surface weathered layer and the bedrock (Yilmaz, 2001). The quality of the first-break picks is dependent on the near-surface conditions and the source. As stated previously, first-breaks were not very clearly distinguishable in drop-hammer source shot gathers. High levels of noise in traces adjacent to the source also made it difficult to distinguish first-breaks. Various models with different levels of simplification were tested for both seismic lines to determine the 'best-fit'. The inversions were carried out using a ray-tracing approach (Woodward 1991).

Field- and residual-statics were computed and extracted from the calculated models. 3-layer models were found to yield the best results for both seismic line SM2 and SM3 (Figure 19). As can be seen in Figure 19, velocity profile SM2 is very basic and has no lateral velocity variations. More complex models were created and tested with lateral velocity variations, however it was found that these complex models had a negative impact on the quality of the reflections observed in the data at later stages in data processing. Final stacks from both the simplified model and the more complex model were compared. The final stack produced from the simplified version was significantly better. For this reason, this simplified model was selected. Various models were also tested for seismic profile SM3. Figure 19 shows the model which was found to yield the best results. Field and residual refraction statics for each line were extracted from the models shown in Figure 19. However, it was established after testing, that superior results

were obtained for both seismic lines when only field static corrections were applied. Therefore, residual refraction static corrections were not applied to either seismic line.

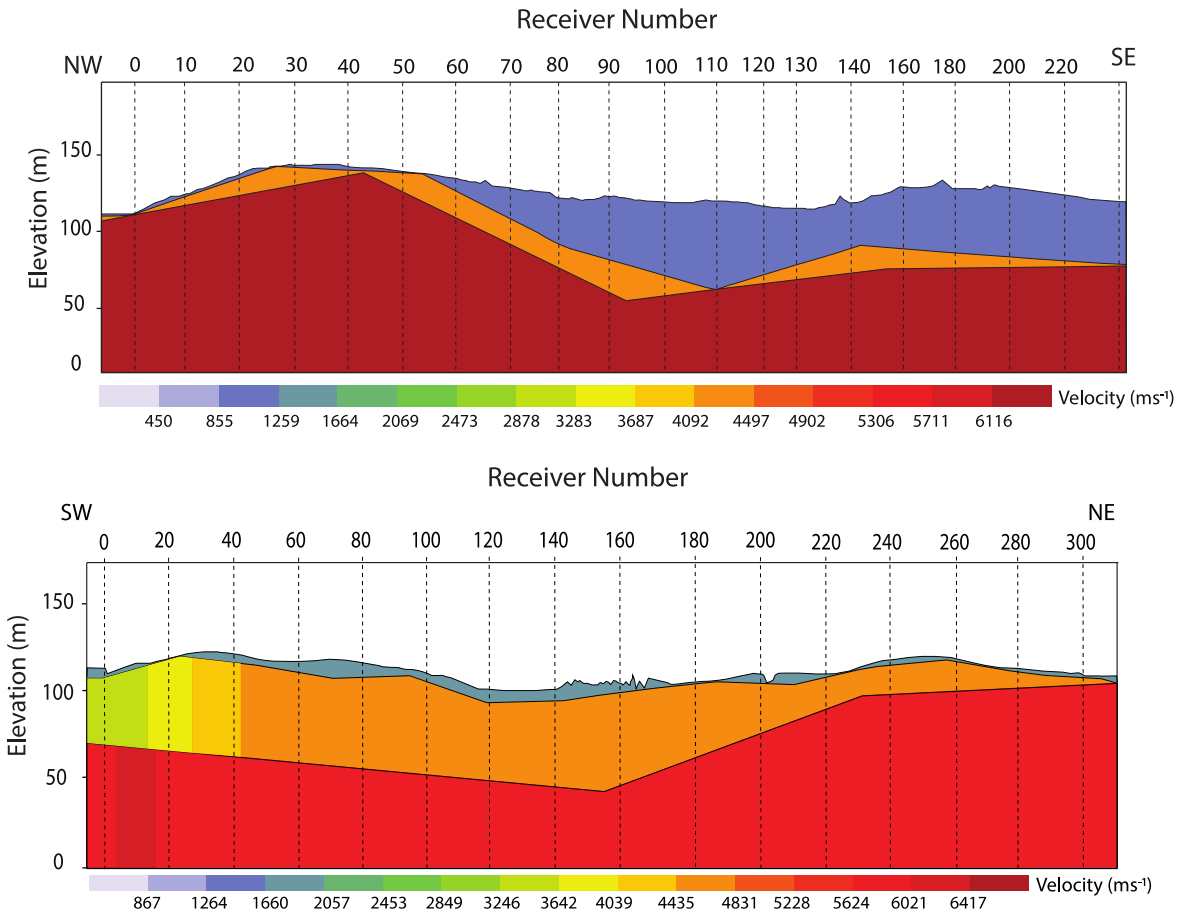

Figure 19. Near-surface velocity model solutions for SM2 (upper) and SM3 (lower). Models were generated based on the first-break picks, geometry information and assumed P-wave velocities.

Field-static corrections were applied to the data, data was moved to a floating datum where the travel-times were no longer affected by the low-velocity layer (Figure 20). A replacement velocity of 5000 ms^{-1} was used.

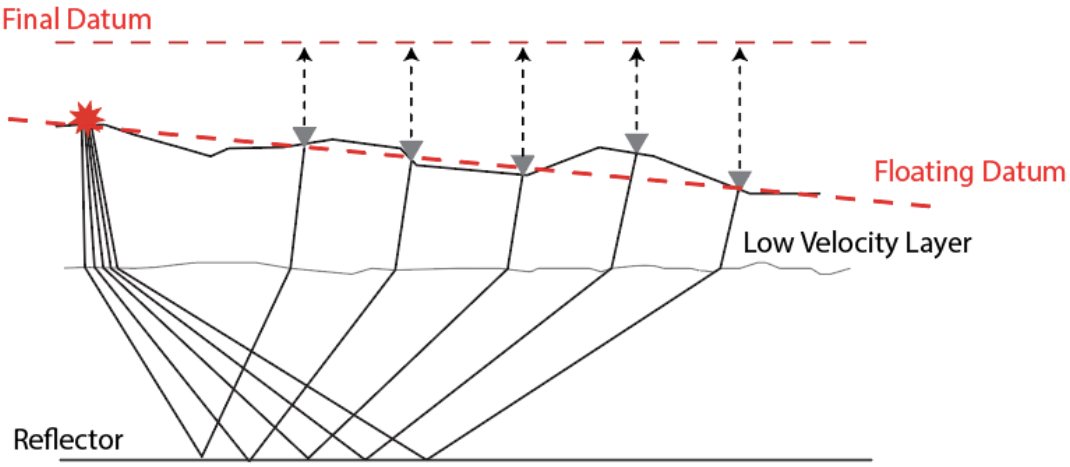

Figure 20. Diagram illustrating the impact of a low-velocity weathered layer and elevation fluctuations on the seismic wave ray-paths. After static corrections are applied, data is moved to a floating datum prior to stacking. Once stacking is applied, data is moved to a final datum level where reflections appear as if the sources and receivers had been on the one datum level.

To correct for short-wavelength variations, residual static corrections were calculated and applied prior to stacking. Residual static corrections are based on travel-time distortions associated with reflections on NMO-corrected CMP gathers (Taner et al. 1974). They were calculated by the cross-correlation of traces in a CMP gather with a pilot trace in order to compute residual static shifts within a specified time window. Several time windows were tested to determine which yielded the best result without distorting reflections outside the time gates. These corrections were carried out in rotation with velocity analysis and NMO correction. Improvements were made by recalculating the residual statics multiple times in conjunction with adjustments being made to NMO velocity model and corrections. This is due to the impact static corrections, NMO corrections and velocity analysis have on one another. Improvements in the static corrections allow for further improvements in the NMO corrections and velocity models. This cycle was repeated multiple times to obtain optimal results. The data was later corrected to a constant datum with final datum statics after the data was stacked.

3.2.2 Amplitude Corrections

As discussed in section 3.1.1, the amplitude of seismic waves is impacted by several factors, for example, absorption and signal scattering. Amplitude corrections were applied to the data to compensate for the effects of these various factors.

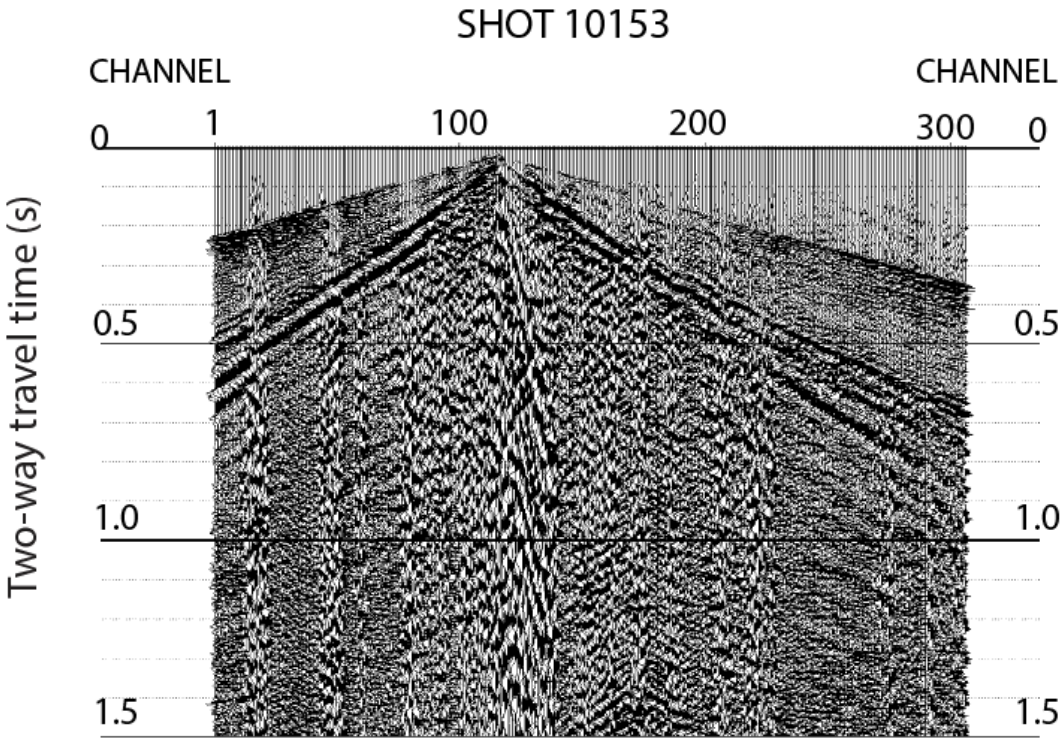

Figure 21. Shot gather (10153) from SM3 with static corrections and spherical divergence applied.

Spherical divergence is the effect geometrical spreading has on the amplitude of the wavefront (see section 4.1). The amplitude of the wavefront decreases substantially with depth as a result of this. The impact that this has on the data was compensated for by multiplying each trace with an exponential scaling function of time (Figure 21)

$$g(t) = t^{\alpha} \tag{3.11}$$

Where t is time and α is the absorption coefficient.

Air waves were removed from the data by surgically muting the area in the shot gathers (Figure 22). A velocity of 330 m/s was used for the muting interval.

High-amplitude S-wave arrivals were observed in seismic profiles SM2 and SM3. These S-waves greatly impacted the resulting stack and disguised areas of shallow subsurface reflectivity. The function which was used to mute the air waves was also used to test the

impact attenuating or muting these arrivals had on the final stack. Both muting and attenuating the S-waves were tested on both SM2 and SM3. A combination of muting and attenuation was found to yield the best results for SM. Muting was applied to the shots located in approximately the middle of the survey line. For the remaining shots, S-waves were attenuated. Similar tests were carried out on the data in profile SM3. However, the resulting stacks showed that attenuating and/or muting the S-wave arrivals had a negative impact, removing shallow reflections. As a result, the S-wave arrivals in profile SM3 were left untouched. The data quality of SM3 is poorer in comparison to SM2. The quality of the data varies along SM3, possibly due to the use of the bobcat source in approximately the middle of the survey line. The combination of the poor data quality and muting/attenuation of the S-waves may be why reflections in the stacks were so greatly impacted in SM3 in comparison to SM2.

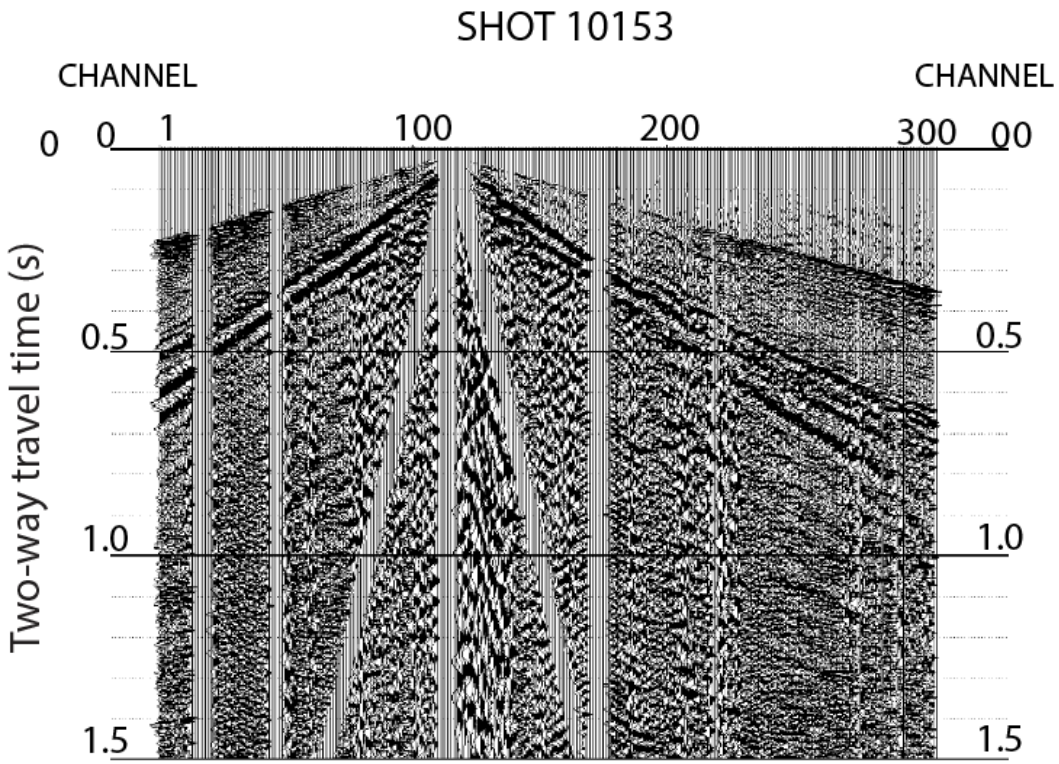

Figure 22. Shot gather (10153) from SM3 with automatic muting applied and airwaves have been muted. Manually picked noisy/dead traces have also been removed (in addition to the corrections applied in Figure 21).

Further amplitude corrections were also applied to both data sets to compensate for time-variant amplitude variations. Automatic gain control (AGC) was applied to balance out

amplitudes across traces by increasing the amplitude of weaker signals. This gain function is a time-variant scaling of amplitudes which adjusts the gain applied in accordance with the seismic signal amplitude level. It works by using a sliding window of a fixed length in which an average amplitude value is computed, the scale factor required to normalise this average to a fixed value (i.e. 1.0) is then calculated. This scaling factor is constant for each trace in the data, traces are scaled horizontally and vertically. The visualisation of reflective events was improved after the application of the AGC function. However, this gain function is a non-linear operator and as a result it alters the characteristic of the signal. For this reason, care had to be taken when apply AGC to the data and a time-invariant amplitude balancing function was tested on the data for a comparison. The balance function is a time-invariant scaling of amplitudes which was applied to the data to test its affect in comparison to AGC. The balance function differs from a gain function as trace balancing is typically based on root mean square (rms) -amplitude criterion (Yilmaz 2001). Whole-trace balancing was applied to the data. Similar results were produced with both approaches. To compare the visualisation of reflective events, both datasets were input into the GOCAD® 3D modelling environment. In this software, it was found that the AGC function produced better-balanced images for interpretation. Whole-trace balancing was later applied to improve visualization to the post-stack data.

3.2.3 Frequency Filtering

Frequency filtering was carried out to separate frequencies at which noise and unwanted energy, e.g. surface waves, dominate from the desired reflections. This improved the signal-to-noise ratio. Unwanted frequencies in seismic data can be both low-frequency, for example ground-roll, and high-frequency, for example ambient noise. Band-pass filtering was chosen for the data because it filters out both high and low frequencies outside a given bandwidth. A wide bandpass is desirable to keep as much wanted frequencies as possible. However, a compromise is required between the wanted signals and the unwanted noise.

Several band-pass filters were tested for both SM2 and SM3 to determine which frequencies were dominated by noise and which were reflected signals. As can be seen in Figure 23, the dataset from seismic line SM3 is dominated mostly by low-frequency noise (approximately 30 - 40 Hz). Similar observations were made for SM2. For SM2, despite

the low-frequency noise the optimal lower value for the bandpass filter was found to be 30 Hz. This was chosen in order to remove a large portion of the low-frequency noise and also preserve reflection events in the dataset. The upper frequency of the bandpass filter was set to 150 Hz. Taper values were also set in order to reduce the ringing effect caused by the Fourier transform used for filtering. A lower taper value of 10 Hz and an upper taper value of 170 Hz was used for profile SM2.

For seismic profile SM3, the low frequency of the bandpass filter was set to 40 Hz. This was found to give the optimal results in filtering out low-frequency noise and preserving reflection events. The high frequency was set to 150 Hz. As was the case for SM2, taper values were also set. A lower value of 25 Hz and higher value of 170 Hz was chosen. Figure 24 shows an example of a shot gather from SM3 with this bandpass filter applied. As can be seen, the level of noise in the gather has been significantly reduced.

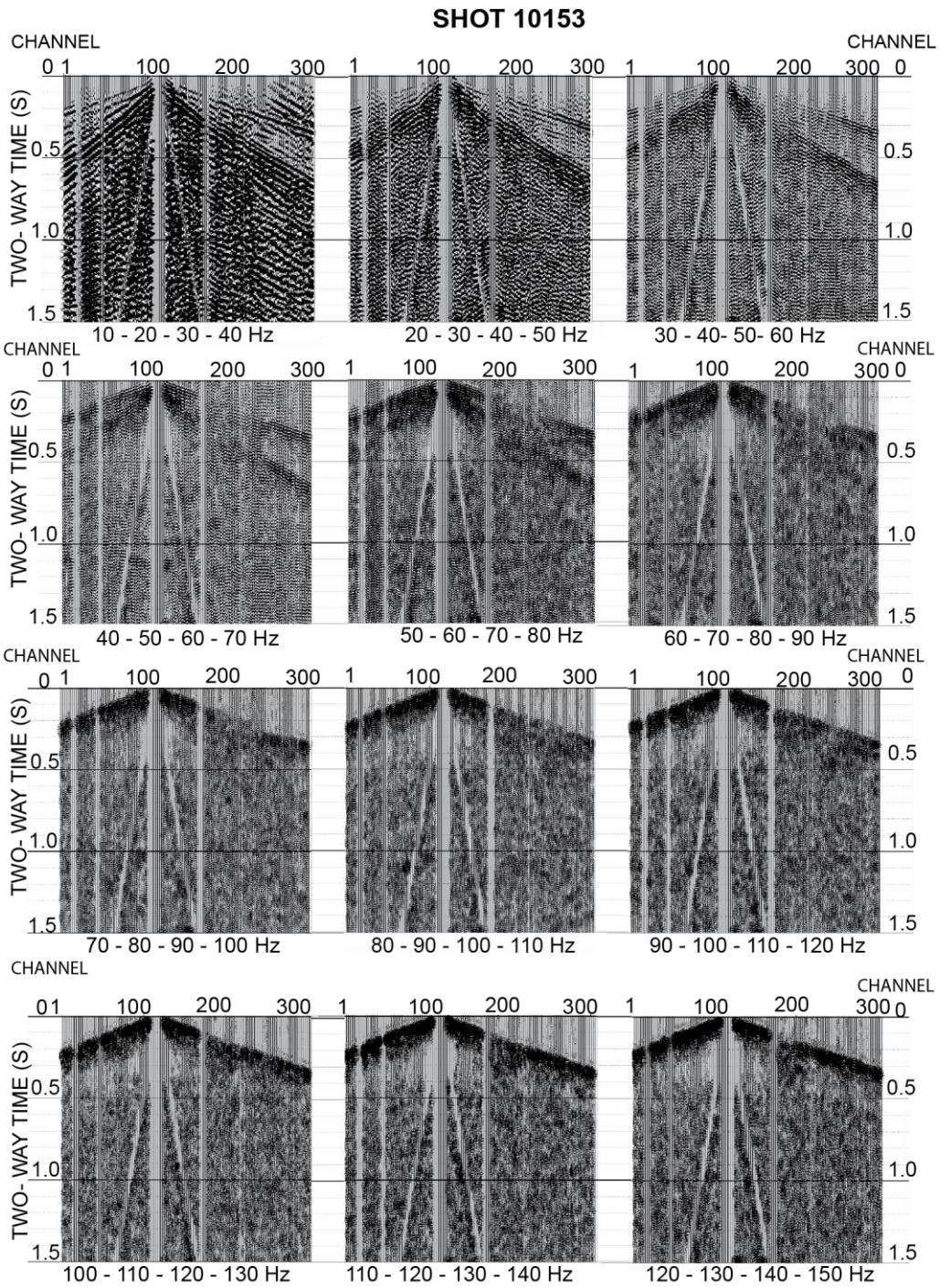

Figure 23. Comparison between different bandpass filters. Shot number 10153 from SM3 was used for this example.

Deconvolution is an additional processing step which can improve the signal-to-noise ratio. Deconvolution can improve the temporal resolution of the data by reversing the effects of successive convolutions to reconstruct the reflectivity function/ the shape of a waveform. Various algorithms, including spiking deconvolution and predictive deconvolution, were tested on the data but results were unsatisfactory, and deconvolution was not applied to the data as a part of the final processing workflow.

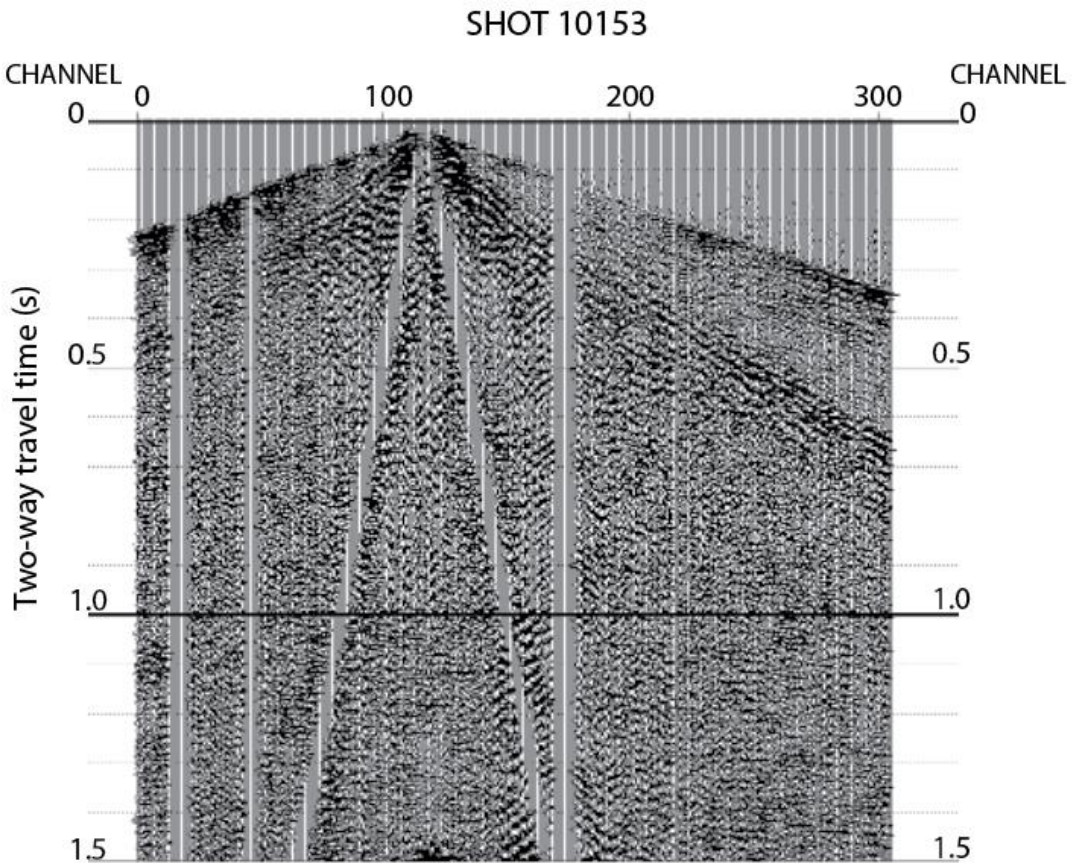

Figure 24. Shot gather from profile SM3 (shot 10153) with bandpass filter (20-40-150-170) applied (in addition to previous corrections shown in Figure 21 and 22).

3.2.4 Stacking and Velocity Analysis

CMP stacking is an effective way of improving the signal-to-noise ratio in the data. By summing traces from the same CMP, reflective signals are strengthened, and noise is dimmed. Prior to stacking, NMO correction needs to be applied to the data to compensate for travel-time delays caused by nonzero offsets. The NMO correction is obtained by the equation

$$\Delta t_{NMO} = t(x) - t_0 \approx \frac{x^2}{2V^2 t_0} \tag{3.12}$$

where $t(x)$ is the measured time, t_0 is zero-offset time, x is the offset distance and V is the seismic velocity. Therefore, velocity is required to carry out the NMO correction. A

constant velocity was used to create the first NMO velocity model required for stacking. As stated previously, this was carried out in a round with residual static corrections (see section 3.2.1). The velocity model which was used for the NMO correction for seismic profile SM2 is shown in Figure 25. The NMO correction was applied to the dataset and the data was CMP stacked (Figure 26).

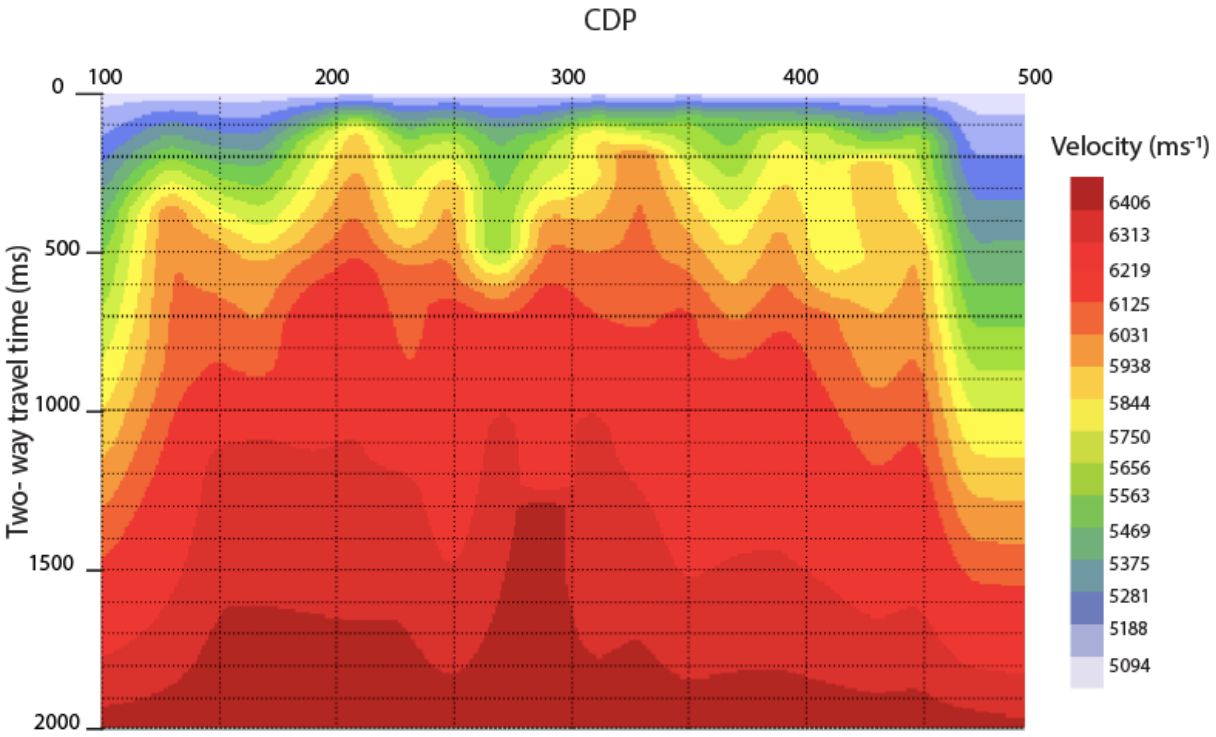

Figure 25. Final velocity model created for SM2 which was used for the NMO correction. Velocities in the model are represented with respect to the two-way travel-time and the CMP number.

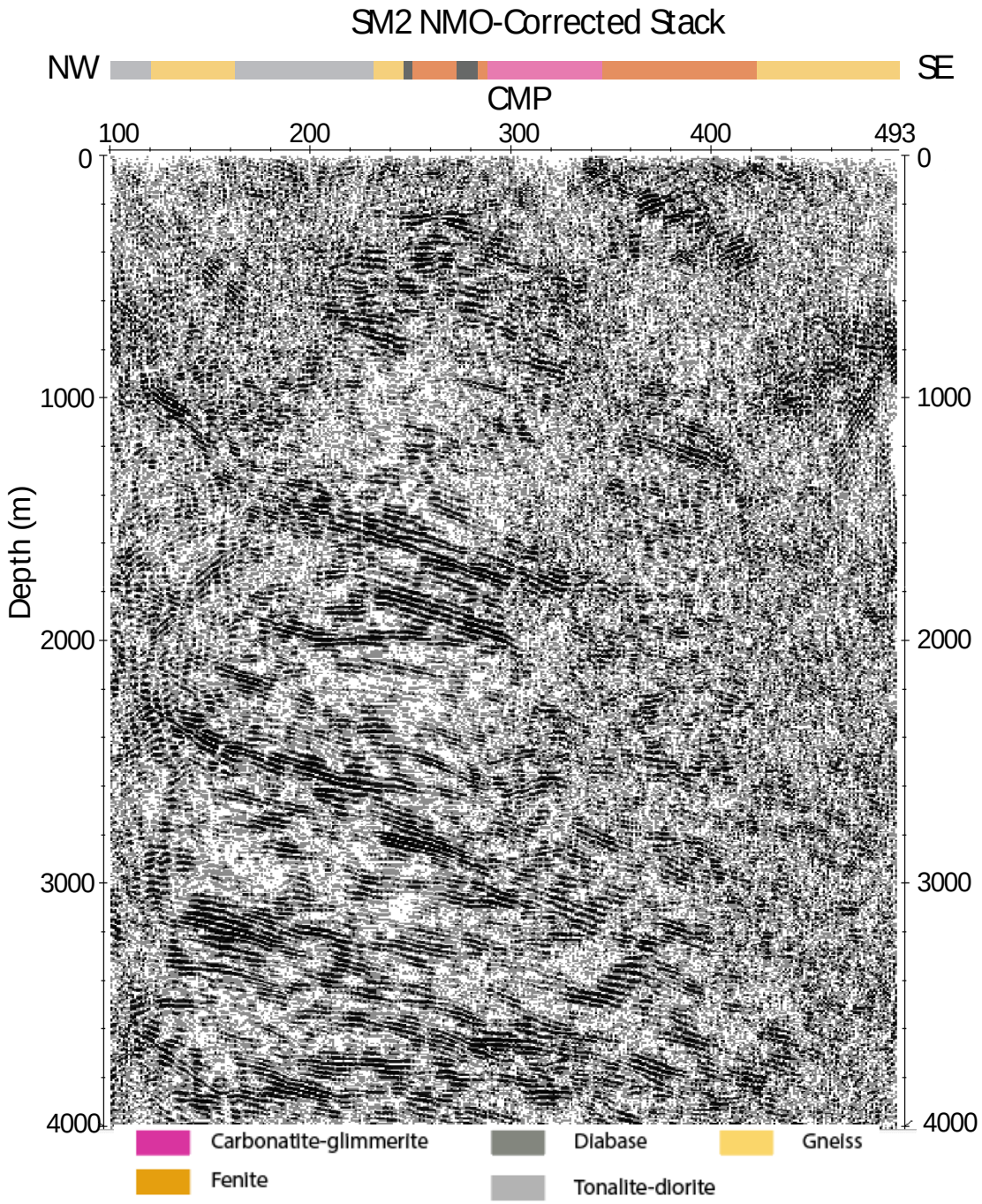

Figure 26. Unmigrated, NMO-corrected and CMP-stacked data from SM2. The velocity model presented in Figure 25 was utilised for the NMO correction. To improve the display, post-stacking processing tools such as f-x deconvolution, additional filtering, balancing and AGC have been applied to the stack. The geology bar displayed above the stack was extracted from the known surface geology (Figure 18). (Scale 1:2)

Similar processing steps were also applied to the dataset from seismic profile SM3. However, as previously mentioned S-wave were not supressed in the data from SM3 due to the negative impact this process had on the data. The resulting velocity model which was used for the NMO correction is shown in Figure 27 and the NMO-corrected CMP stack is displayed in Figure 28.

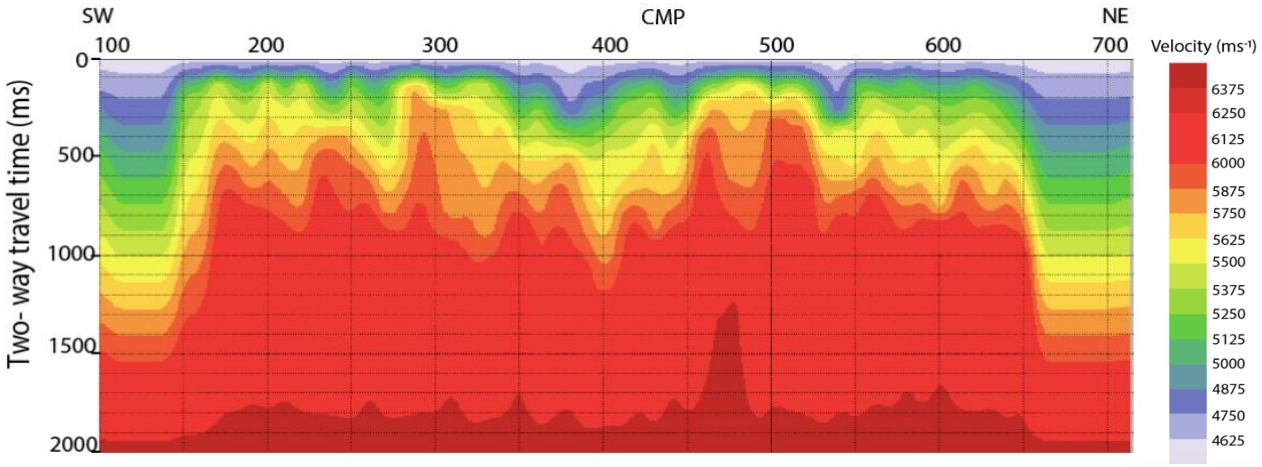

Figure 27. Final velocity model created for SM3 which was used for the NMO correction. Velocities in the model are represented with respect to the two-way travel-time and the CMP number

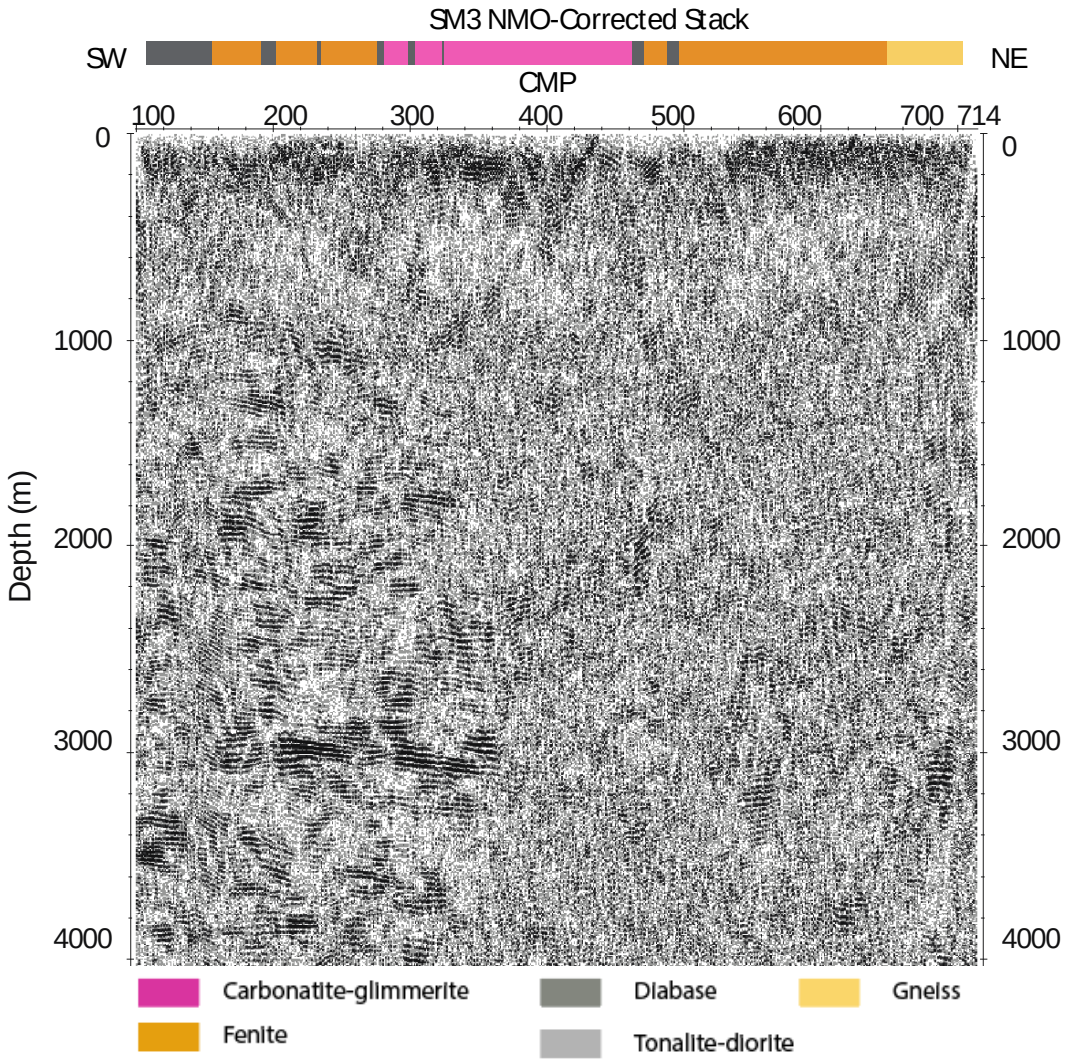

Figure 28. Unmigrated, NMO-corrected and CMP-stacked data from SM3. The velocity model presented in Figure 27 was utilised for the NMO correction. To improve the display, post-stacking processing tools such as f-x deconvolution, additional filtering, balancing and AGC have been applied to the stack. The geology bar displayed above the stack was extracted from the known surface geology (Figure 18).

3.2.5 Migration and Time-to-Depth Conversion

Migration was applied to the data to move dipping reflections to their true positions in the subsurface and to collapse diffractions (Figure 29). As a result of this, the spatial resolution of the data is increased. The aim of migrating the data is to obtain a section which resembles the geologic cross-section at depth along both seismic profiles. Prior to migration, dipping features in the subsurface appear as dipping reflectors. However, the slopes are different, with the true dip of the reflector being greater than what is observed in the seismic data. The relationship between the true dip (ξ) and the apparent dip (ξ_a) is:

$$\tan(\xi_a) = \sin(\xi) \tag{3.13}$$

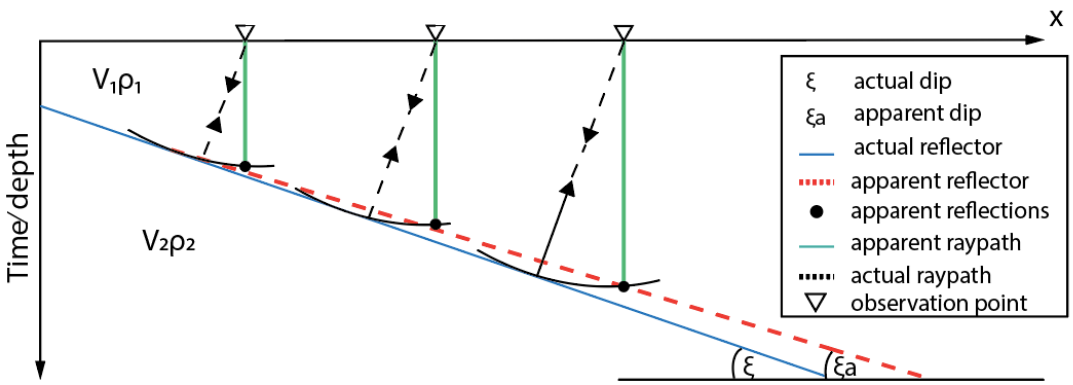

Figure 29. Diagram illustrating the principle of migration. The migration process moves dipping reflections to their true positions in the subsurface. Both the apparent and true positions of the reflector and their respective dipping angles ξ and ξa are illustrated in the diagram.

Migration can be done both pre-stack and post-stack. For a simple model without dips or lateral velocity various, both approaches would yield similar results. However, for a more complex model, consisting of large dips and significant lateral velocity various, pre-stack migration is more effective. For the Siilinjärvi study area, post-stack migration was adequate. The Kirchhoff migration algorithm was applied to both of the seismic profiles (SM1 and SM2) post-stack. Kirchhoff migration uses the Kirchhoff integral to integrate along diffraction curves and placing the results at the creases of the diffractions curves (Sheriff & Geldart (1995)).

Additional processing tools were applied after migration to visually improve the stacks and boost the reflections. This included additional frequency filtering, additional AGC, fx-deconvolution and semblance smooth and balancing. These tools were applied to aid in the data interpretation. However, it was important to be conscious of the effect each of these tools had on the stacks in order to prevent false reflections from appearing.

The final step in processing the seismic data was to convert the data into the depth domain. To do this, a time-to-depth conversion was applied to the stacks. This conversion was performed by using a constant velocity of 5500 ms^{-1}. This velocity was chosen so that the stacks of SM2 and SM3 would be comparable with the other reflection seismic profile, SM1, which also used this velocity for the conversion (Laakso 2019).

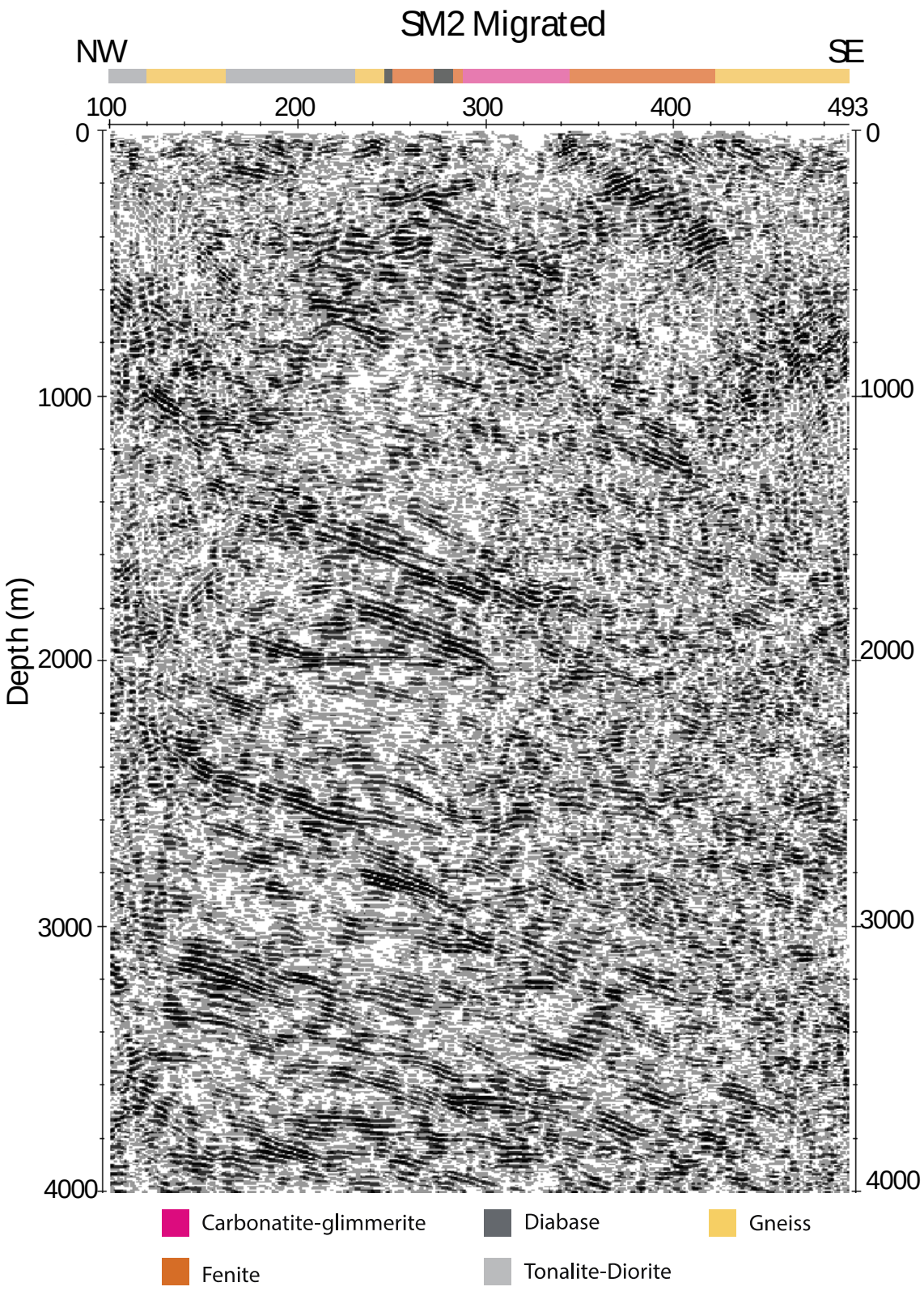

Figure 30. Migrated stack of seismic line SM2. Kirchoff's migration algorithm was utilised to migrate the data. To improve the visualisation, post-stacking tools such as f-x deconvolution and additional filtering, balancing and AGC have been applied to the stack. The geology bar has been extracted from the known surface geology. See Figure 18 for the geology and CMP locations. (Scale 1:2).

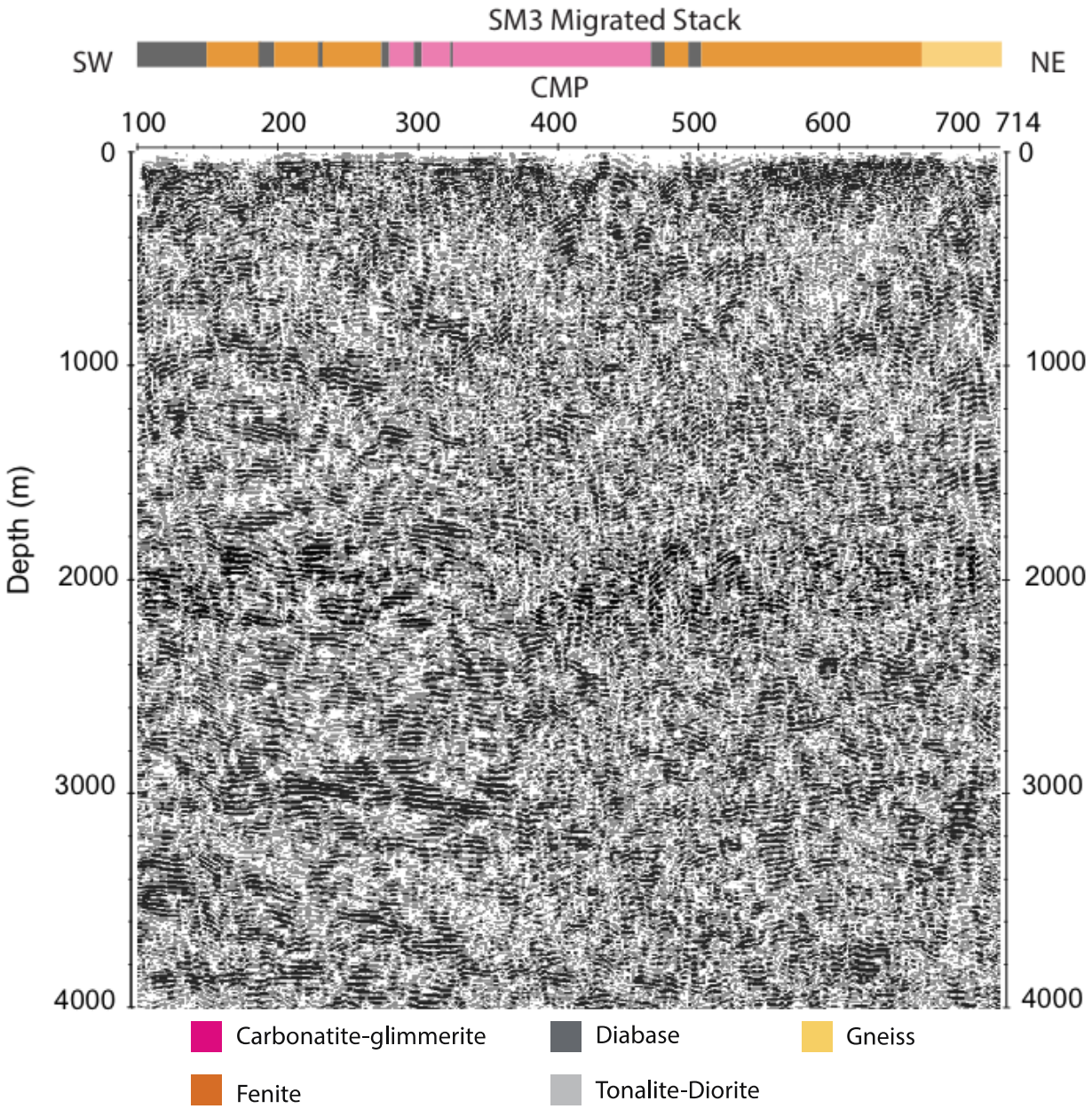

Figure 31. Migrated stack of seismic line SM3. Kirchoff's migration algorithm was utilised to migrate the data. To improve the visualisation, post-stacking tools such as f-x deconvolution and additional filtering, balancing and AGC have been applied to the stack. The geology bar has been extracted from the known surface geology. See Figure 18 for the geology and CMP locations. (Scale 1:1.5)

4 GROUND PENETRATING RADAR

4.1 Fundamentals of GPR

4.1.1 Background Theory

Ground penetrating radar (GPR) is a widely used geophysical technique with a diverse range of applications. The method utilises high-frequency pulsed electromagnetic (EM) waves, usually in the range of 20MHz – 2GHz, to create images of the shallow subsurface (Jol 2008 and Knight 2001). The response of a material to an EM wave is a function of the dielectric properties of the material. The physics of the propagating EM fields are described by Maxwell's equations, while material properties are quantified by constitutive relationships. A combination of both of these elements are the foundations for quantitatively describing GPR signals. This section presents aspects of GPR theory which are fundamental for this study. A more detailed description can be found for example in Jol (2008) and Reynolds (2011).

GPR exploits the electrical properties of a material. The electrical properties are described by the dielectric permittivity ε and electrical conductivity σ (Jol 2008). The propagation of an EM wave through a material is dependent on the dielectric properties of the material, but is also significantly affected by the electrical conductivity. Electrical conductivity is the property which controls the attenuation of the EM signal. It characterizes free charge movement when an electric field is present. The dielectric permittivity describes a material's ability to store and release EM energy in the form of electric charge. It is common practice in GPR to assume low-loss conditions (partially conducting medium), $\sigma \ll \omega\varepsilon$, where $\omega = 2\pi f$ is angular frequency and ε is the dielectric permittivity which can be defined as the product of the dielectric permittivity in a vacuum ε_0 and relative dielectric permittivity ε_r. In non-magnetic ($\mu_r = 1$), which are also typically assumed, low-loss materials, the relative dielectric permittivity controls the velocity v of EM waves. The velocity can be approximated by:

$$v = \frac{c}{\sqrt{\varepsilon_r}} \tag{4.1}$$

Where c is the speed of light in a vacuum ($c \approx 0.3$m/ns).

Electromagnetic waves propagate from a source through a medium as a growing cone, causing an exponential decrease in amplitude A from the original value A_0 as the wave

travels distance *z*. The decrease in amplitude of EM waves is a result of geometrical spreading and absorption of energy in the media. This decrease in amplitude can be expressed as

$$A = A_0 e^{-\alpha z} \tag{4.2}$$

where α is the attenuation constant (Jol, 2008). Attenuation is a frequency-dependent measure of the spatial rate of decay of the wave in the medium. The attenuation factor increases with increasing signal frequency resulting in stronger attenuation scattering of the signal. In low-loss conditions, however, the attenuation constant can be approximated to be independent from frequency, and can be expressed as

$$\alpha = \frac{\sigma}{2}\sqrt{\frac{\mu}{\varepsilon}} \tag{4.3}$$

Conductivity has therefore the greatest influence on the attenuation constant. Attenuation dictates how deep an EM wave can penetrate the medium. The distance through which the amplitude of an EM wave decreases by an amplitude of e^{-1} is referred to as skin depth (δ) of the medium. For low-loss conditions this can be determined by

$$\delta = \frac{\sigma}{2}\sqrt{\frac{\varepsilon}{\mu}} \tag{4.4}$$

In general, the skin depth is smaller with higher frequencies. It increases in materials with lower conductivities and/or higher dielectric permittivities. However, the skin depth does not equate to the depth of penetration of the GPR. A general rule of thumb is that the depth of penetration can be estimated to be approximately 5 times the skin depth. The use of high GPR frequencies results in better resolution but the depth of penetration is decreased.

4.1.2 EM Waves at an Interface

When an EM wave encounters an abrupt change in dielectric permittivity, a portion of the energy is reflected while another portion is transmitted across the interface. This

happens similarly to a seismic wave encountering a boundary (see section 3.1.2). The strength of the reflected wave is proportional to the magnitude of the contrast in dielectric permittivity of the two materials. The intensity of a reflected EM wave can be estimated by the reflection coefficient *R*. This occurs similarly to seismic waves encountering a boundary, as discussed in section 5.1.2. The EM waves in GPR measurements are treated as if they hit the interface at a normal incident angle (vertical), meaning that the reflected and transmitted waves travel vertically. Assuming low-loss conditions, non-magnetic media and a normal incidence, the reflection coefficient *R* can be estimated by

$$R = \frac{A_r}{A_i} = \frac{\sqrt{\varepsilon_{r2}} - \sqrt{\varepsilon_{r1}}}{\sqrt{\varepsilon_{r1}} + \sqrt{\varepsilon_{r2}}} \tag{4.5}$$

Where A_r is the amplitude of the reflected wave and A_i is the amplitude of the incident wave. ε_{r1} and ε_{r2} are the relative dialectic permittivies of the adjacent layers, 1 and 2. Typically, ε increases with depth so in general $\varepsilon_{r1} < \varepsilon_{r2}$ (Reynolds 2011). *R* lies within the range +1 to -1.

Vertical resolution ΔV is a measure of the ability to differentiate between two signals adjacent to each other in time. It is dependent on the centre frequency (f_c) of the antenna and the velocity of the EM wave. The vertical resolution can be estimated by

$$\Delta V = \frac{V}{4f_c} \tag{4.6}$$

It is evident from eqn. 4.6 that a higher centre frequency yields a higher vertical resolution.

Horizontal resolution ΔH is the measure of how close two reflecting points can be located horizontally and still be recognized as two separate points instead of one. As with the vertical resolution, the horizontal resolution depends on the centre frequency and EM wave velocity. However, in addition to these, depth *z* is also an important factor for horizontal resolution:

$$\Delta H = \sqrt{\frac{zv}{2f_c}} \tag{4.7}$$

Horizontal resolution decreases with depth, this is due to energy expanding laterally as it propagates downwards (Neal 2004). Reflectors which are smaller than the horizontal resolution generate diffraction hyperbolas in the data.

4.1.3 GPR Method

The most common form of GPR measurements is with a transmitter and a receiver in a fixed geometry, meaning that data is acquired with a common-offset setup. The transmitter emits pulses of high-frequency electromagnetic energy into the subsurface. Reflections occur when the propagating energy encounters interfaces of materials with a contrast in relative dielectric permittivity. The reflected waves are detected by a receiver antenna on the surface (Figure 32). Multiple pulses of signal are emitted at each survey point to obtain stacks of the data. The two-way travel time and the amplitude of the reflections are measured by the receiver and this can be then used to obtain a cross-section of the subsurface structure at depth.

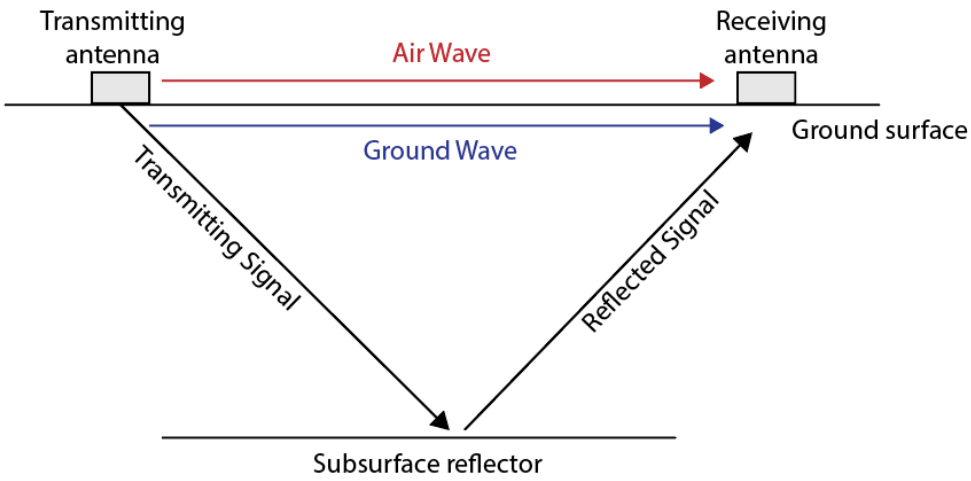

Figure 32. Diagram showing the ray paths of electromagnetic waves emitted from the transmitter of the GPR system. Ray paths of the air wave, ground wave and reflected wave associated with a common-offset GPR survey are displayed. Image is modified after Neal (2004).

4.2 Acquisition of GPR data in Siilinjärvi

GPR data was acquired along seismic profile SM2 (Figure 34). Weather conditions during data acquisition, temperatures varied between -5 and -10°C, meaning that the ground was frozen.

GPR data was collected along SM2 using a 30 MHz and 50 MHz antenna. Both datasets were processed, and the results were compared. The observation was that both frequencies yielded similar results. This study focuses on the 30 MHz data due to the greater depth of penetration.

The GPR system utilised for data acquisition was MALÅ ProEx system using the MALÅ rough-terrain 30 MHz unshielded antenna with fixed geometry (MALÅ GPR Australia 2009-2017). The acquisition system, which is owned by the University of Helsinki, was comprised of; MALÅ Professional Explorer control unit, MALÅ XV monitor, measuring wheel/ hip chain, GPS and antennas, transmitter and receiver (Figure 33). The data was acquired using a common-offset, single-fold survey design, meaning that the system was transported along the survey line with a fixed antenna geometry and measurements were made at regular station intervals. This type of survey mode maps the subsurface reflectivity versus spatial position (Jol, 2008).

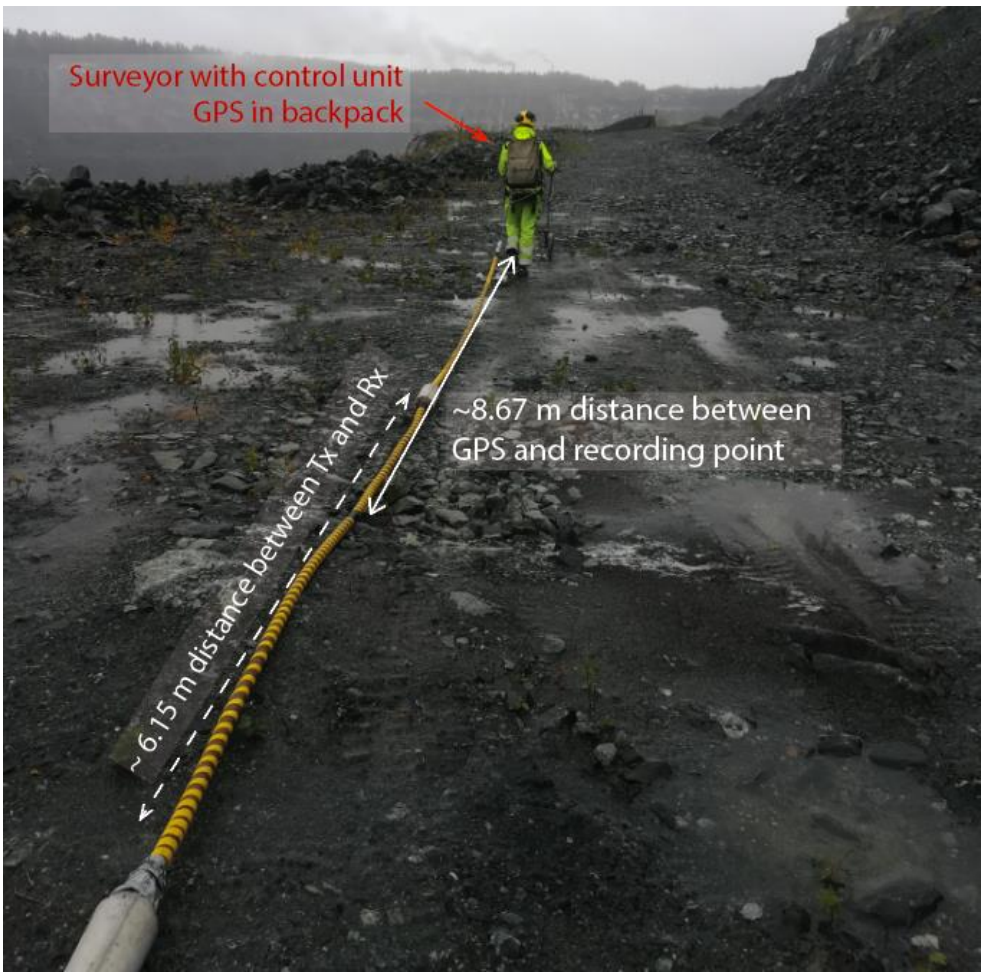

Figure 33. Field image of Smart Exploration team member operating the GPR system data acquisition in the Särkijärvi pit. The GPS is located in the backpack carried by the surveyor. The distance between the transmitter and receiver (~6.15 m) and the distance between the GPS and the measurement point (~8.67 m) are displayed on the image.

The goal of the GPR survey was to detect changes in the bedrock geology and image any shallow structures present in the bedrock. Low-frequency antennas (centre frequencies of 20-50 MHz) are required to attain a depth of penetration suitable for this type of survey.

GPR data was collected along the survey line by following the wooden pegs, which mark the locations of the seismic sources and receivers, as a guide. In some instances, where the terrain was not favourable or the forestation was too thick, a slightly different route was taken for the GPR, staying as close to SM2 as possible. The beginning of survey line SM2 was not surveyed by the GPR due to the rough, steep terrain. The data was collected in SE direction in three segments, data lines 207, 208 & 209 (Figure 34). Due to the presence of a road (national road 75), there is a gap in GPR data along the survey line. Parts of the survey were in dense forest, especially the line segment 208. An unshielded

GPR antenna can receive aerial signals due to the presence of powerlines, trees or metallic objects above the surface. Any possible causes of aerial reflections were therefore noted during data acquisition.

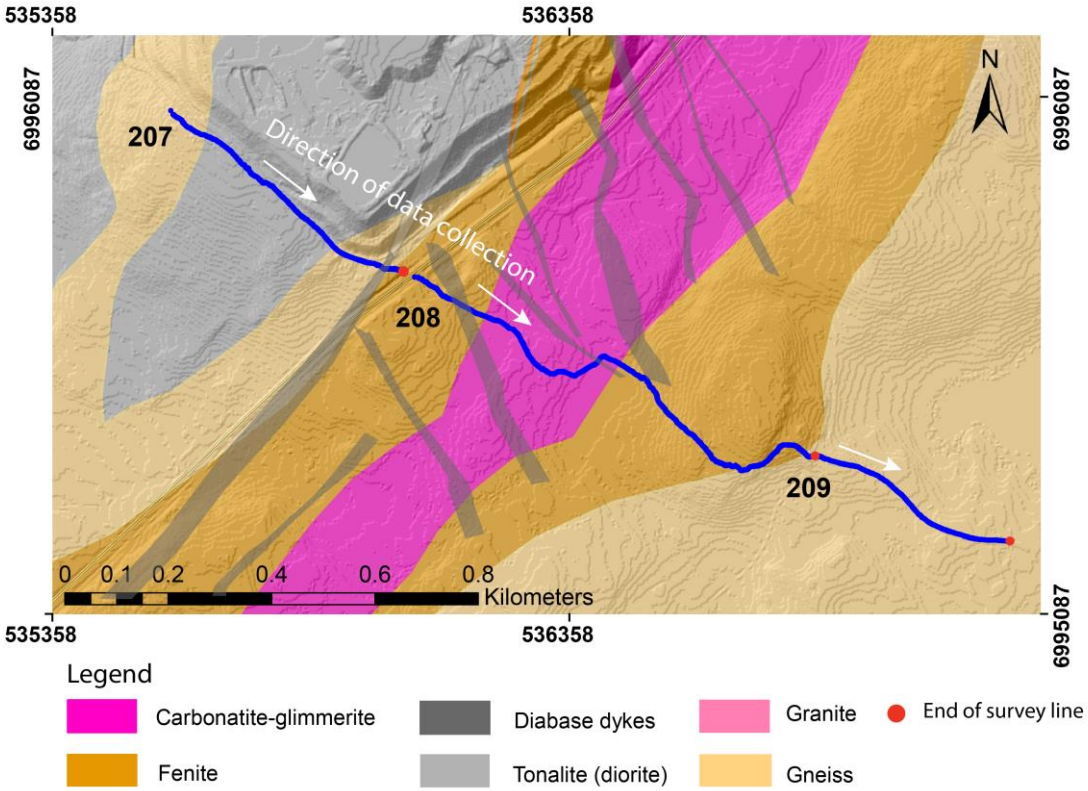

Figure 34. Location of GPR survey lines aquired at the Siilinjärvi mine site during Autumn 2018. The GPR lines were collected along the seismic survey line SM2 (line 207 was located along the cabled section of the seismic line, lines 208 and 209 were located along the wireless section). Coordinates are in the EUREF-FIN ETRS-TM35FIN system. Geology from Yara. Basemap: © National Land Survey of Finland.

The GPS was connected to the MALÅ monitor and continuous coordinate readings were taken during data acquisition. The GPS used in the survey was not of high accuracy and it was carried in the backpack of the surveyor (Figure 33). Prior to data processing, the coordinates acquired from the GPS located in the surveyor's backpack had to be switched with coordinates collected with a high-precision GPS.

A trace spacing of 0.83m was used, using a measuring wheel to measure the distance. The time window, which is the duration of measurements at each measurement point, was

set to 1311 ns. A running stack of 16 was applied. The parameters used for this survey are summarised in Table 2.

Table 2. GPR survey parameters for measurements acquired in Autumn 2008. The theoretical vertical and horizontal resolutions for the survey have been calculated using the equations 4.6 and 4.7. Electromagnetic wave velocities of 0.07-0.13 mns^{-1} were used to calculate the resolutions for the 30MHz frequency antenna.

Survey parameters	**Value**
Survey type	2D Ground Penetrating Radar common offset survey
Profiles	Lines 207, 208 & 209 (all along survey line SM2)
Total length of survey lines	~ 2.1 km
Equipment Information	
GPR unit	MALÅ Professional Explorer (ProEx)
Cabled receiver type	MALÅ rough-terrain 30 MHz unshielded fixed geometry antennae
Acquisition parameters	
Antenna separation	6.15m
Mode of distance measurement (for data collection)	Measuring wheel
Sampling interval	3.3ns
Time window (recording window)	1131ns
Stacks	16
Trace spacing	0.833m
Calculated (theoretical) survey resolution ***(using velocity range of 0.07-0.13mns^{-1} and 30 MHz frequency)***	
Horizontal resolution	2.8 -2.9 at 1m depth, 4.8 -6.4 at 5m depth and 8.3 - 11.0m at 15m depth.
Vertical resolution	0.8- 1.1m

The theoretical horizontal and vertical resolutions for the 30 MHz frequency antenna were calculated using equations 4.6 and 4.7. Electromagnetic wave velocities in the range of 0.07-0.13 mns^{-1} were used in the calculations. The velocity range was based on the typical dielectric constants of the geology/sediments found in the survey area. The theoretical vertical resolution was found to vary between 0.8-1.1 m. The horizontal resolution was

calculated to vary between 2.8-2.9 at a 1m depth, 4.8-6.4 m at 5m depth and 8.3-11.0 m at a 15 m depth.

4.3 Processing of GPR data

Processing of GPR data is similar to that of reflection seismic data, however it is much simpler in comparison. The goal of processing is to increase the signal-to-noise ratio of the data and present the GPR data in a format which accurately reflects the subsurface to aid in the interpretation. GPR data collected at Siilinjärvi was processed using Reflexw software, produced by Sandmeier geophysical research (Sandmeier geophysical research, 2020). The workflow that was performed on the data is summarised in Figure 35.

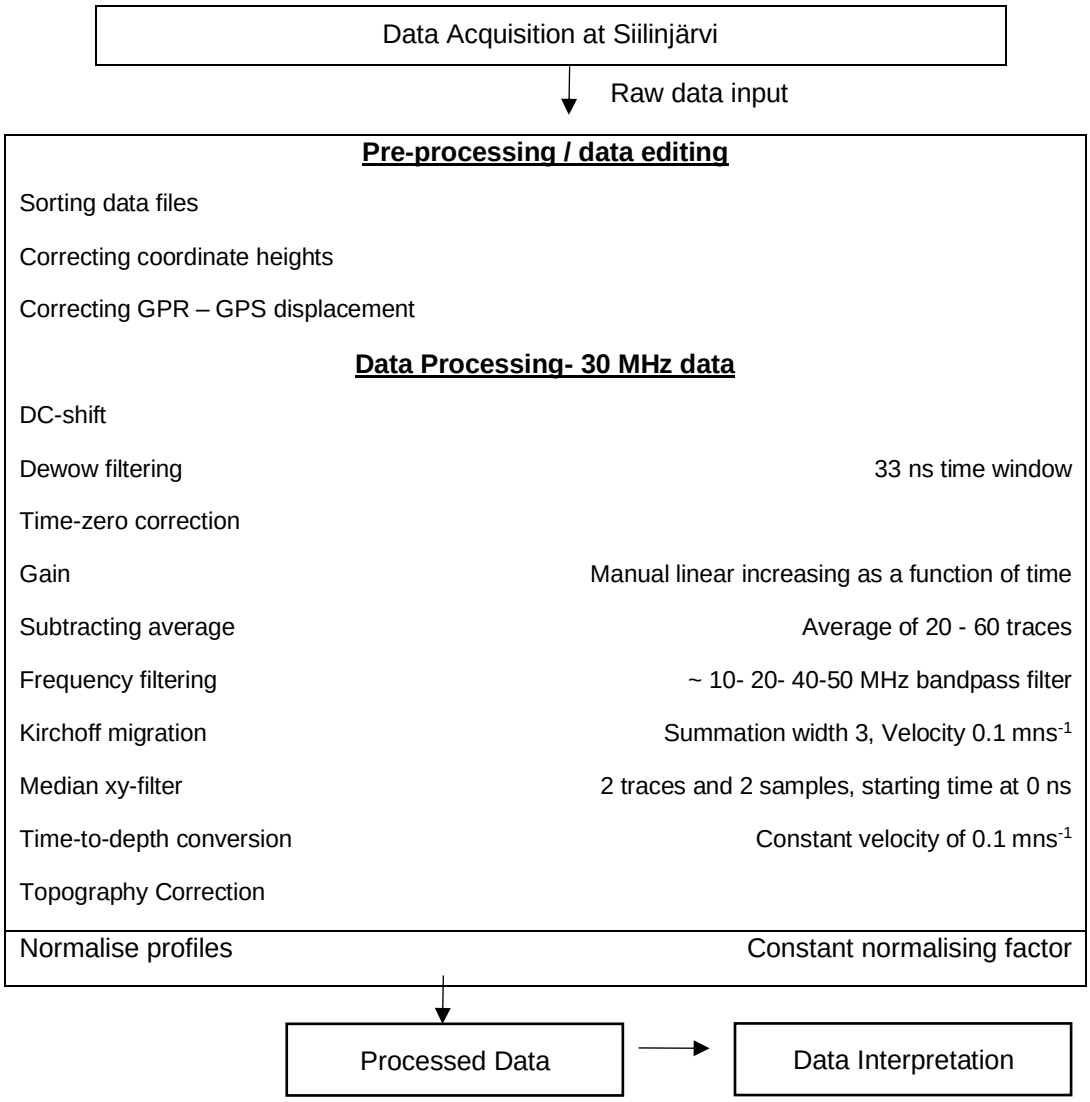

Figure 35.Processing flow used for seismic lines SM2 and SM3.

Prior to importing the raw data into the processing software, the data files and coordinate files were edited. As previously mentioned, the coordinates collected with the GPS in the surveyor's backpack were switched with coordinates collected with a high-precision GPS. The distance between the GPS and the middle of the transmitter and receiver, i.e. the measurement point, was measured to be approximately 8.67m. This distance needed to be accounted for to place each trace at a more accurate location. The correction was performed by increasing the number of each trace by 10 (the distance between the two points divided by trace spacing, 8.67/ 0.83 ≈ 10.4). The error margin between these corrected coordinates and the actual surface positions is approximately 30-40cm.

4.3.1 Time-zero Correction

Discrepancies in the arrival times of the first arrivals can occur due to factors such as cable length differences, thermal drift and variations in antenna airgap (due to obstacles such as areas of higher grass vegetation, rough ground surface etc.). Time-zero needs to be corrected to a common time-zero position, to prevent misalignment of first-arrivals and also of primary and secondary reflections beneath the air and ground waves. The correction considers the transmitter and receiver to be at the same position, i.e. zero-offset. The time delays associated with the antenna separation result in reflectors appearing at a greater depth than their true positions. However, the depth distortion of deeper primary reflections associated with GPR surveys is reasonably small. The effect of the discrepancy becomes more significant with larger antenna separations and less significant with depth. Therefore, NMO correction was not applied to the GPR data, meaning that time delays caused by the transmitter and receiver offset were not subtracted from the travel-times, instead the time prior to the first-break was removed. This concept is similar to the NMO correction applied to the seismic data (see section 3.2.4).

4.3.2 Amplitude Corrections and Filtering

As a result of the electronics of the GPR system, the mean amplitude of traces was slightly shifted from zero. This displacement from zero is referred to as a direct current offset (DC offset). DC shift was applied to move each whole trace to alternate around a mean of zero amplitude.

Signal saturation occurs in the data due to the large energy input to the GPR receiver from the airwave, groundwave and near surface reflections. The receiver is unable to adjust fast enough to the large variations in vertical stacks and as a result induces a low-frequency, slowly-decaying 'wow' in the data. To remove this from the data, the 'dewow' filter was used. This is a high-pass filter which allows the spectral peak for a specific antenna centre-frequency to pass but it supresses the low-frequency 'wow' (Neal 2004). The filter works by subtracting the mean of each trace from the central point. A time window of 33ns was set for the 30MHz data acquired at Siilinjärvi.

Gain was applied to the data to compensate for the decaying of signal amplitude due to signal attenuation and geometric spreading. A time-dependent manual gain function was designed for the data to boost and enhance the signals at later times.

Subtracting-average filter was used to suppress airwave and groundwaves in the data. This 2D filter subtracts the mean of all the traces from each individual trace. The filter also removed background noise and antenna ringing from the data. 20-60 traces were used to calculate the averaged traces. The starting time was set to 15 ns and the end time was set to 110 ns for line 207 and 90 ns for lines 208 and 209.

To remove unwanted high- and low- frequency noise from the data a bandpass filter was applied. This filter is a frequency domain filter which is a combination of both a high- and low-pass filter. Bandwidth values which vary around the centre-frequency (30 MHz) were chosen for the filter. A frequency spectrum was utilised to design an optimal bandpass filter. The high-pass frequency value was set to 40 MHz and the low-pass value was set to 20 MHz. As was the case for filtering the seismic data (section 3.2.3), to avoid undesirable ringing in the data, the filter slopes were tapered to create a softer edge. A lower taper value 10 MHz and a higher taper value of 50 MHz. was selected.

The acquired GPR profiles were moderately pixelated in the presence of noisy traces. To 'smooth' the profiles and make noisy traces less visible, a 2D Median filter was applied to the data post migration. The filter supresses trace- and time-dependent noise and spike events by acting as a low-pass filter in both the x- and y- direction (Sandmeier 2011). The median is calculated over a selected xy-area for each time step. The number of traces (x) selected for the data was 2 and the number of samples was 2. A disadvantage of this filter

is the possibility of decreasing data resolution, because of this a later starting time was used.

Profile normalisation was also applied to the unmigrated data. This is an enhancement tool used to improve the contrast of the radar profiles by 'stretching' the range of the intensity values. A linear scaling function is applied to the pixel values of the radar images to improve the visualisation of the data.

The effects which these various processing steps had on the dataset are illustrated in Figure 36.

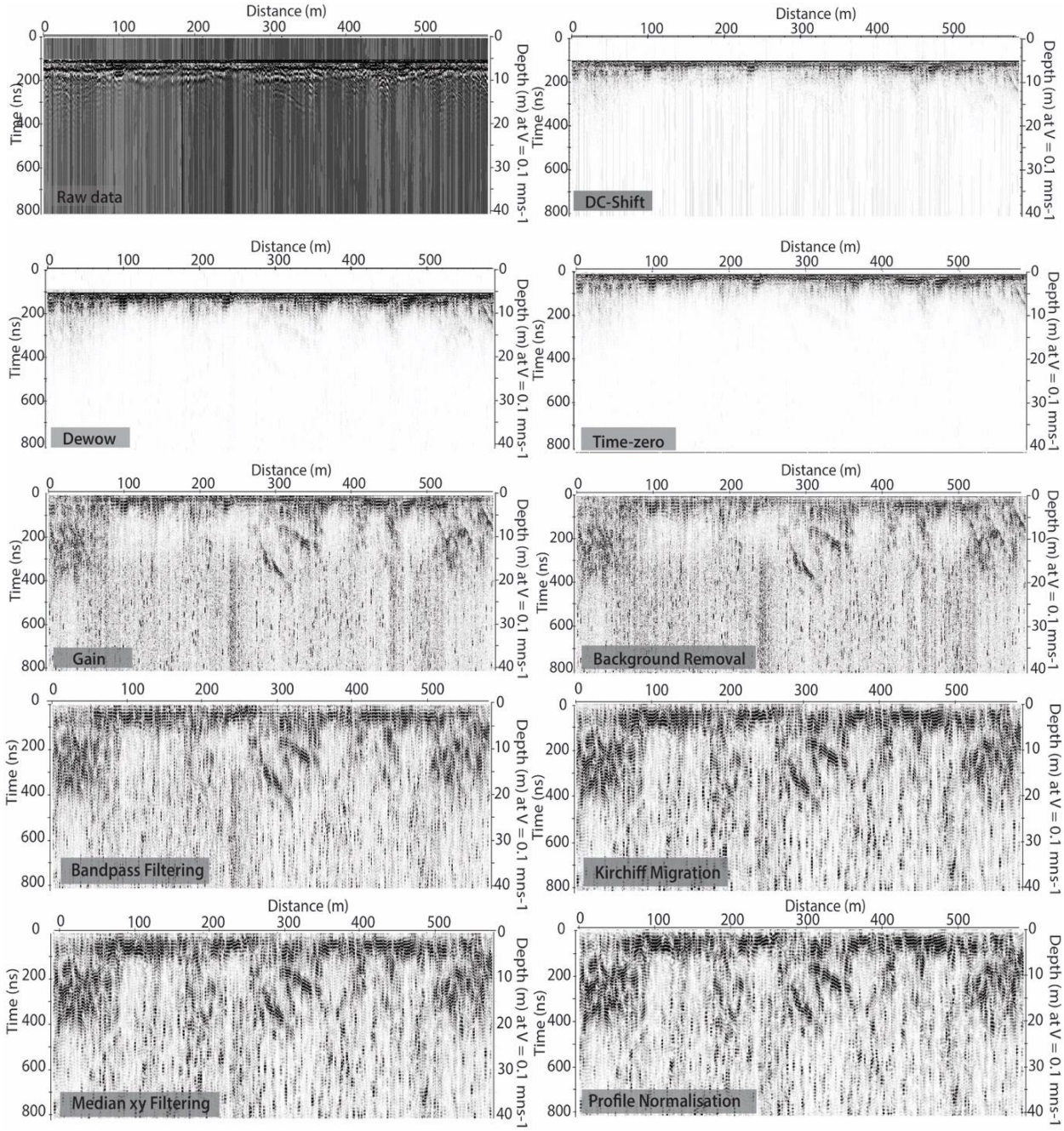

Figure 36. Processing steps applied to the GPR data. Profile 207 is shown to illustrate the impact of each processing step. The processing workflow is presented in Figure 35.

4.3.3 Velocity Analysis and Migration

Good quality subsurface-radar-wave velocity information is essential for accurately converting the data profiles from the time domain to the depth scale. Velocity analysis was carried out on the Siilinjärvi data to obtain this information. This was crucial for achieving accurate depth estimates and was also required for migration (see section 3.2.5). Velocity estimates were made by using hyperbola analysis in the common-offset profiles. Few hyperbolas were seen in the acquired GPR profiles and in the case where hyperbola analysis was not possible an assumed velocity of $0.1 mns^{-1}$ was used. The electromagnetic wave velocity was estimated, based on the dielectric relative permittivity of the materials in the area, to be in the range of $0.09 – 0.13\ mns^{-1}$. Migration was carried out based on the findings from the velocity analysis. Several migration algorithms were tested on the data, out of which the Kirchoff migration proved to be the most suitable choice (Figure 36).

Time-to-depth conversion was carried out on the acquired profiles using the velocity utilised for migration. The depth of penetration for the lines was seen to be approximately 22 to 23m. The topography of the lines was also added to the GPR profile to account for fluctuates in elevations which can cause significant distortions of the subsurface image if it is not corrected. For this correction, elevation information from coordinate files was added to the data.

The three processed lines are presented in Figure 37. Geology bars extracted from the surface geology information are displayed above each profile to aid in the interpretation.

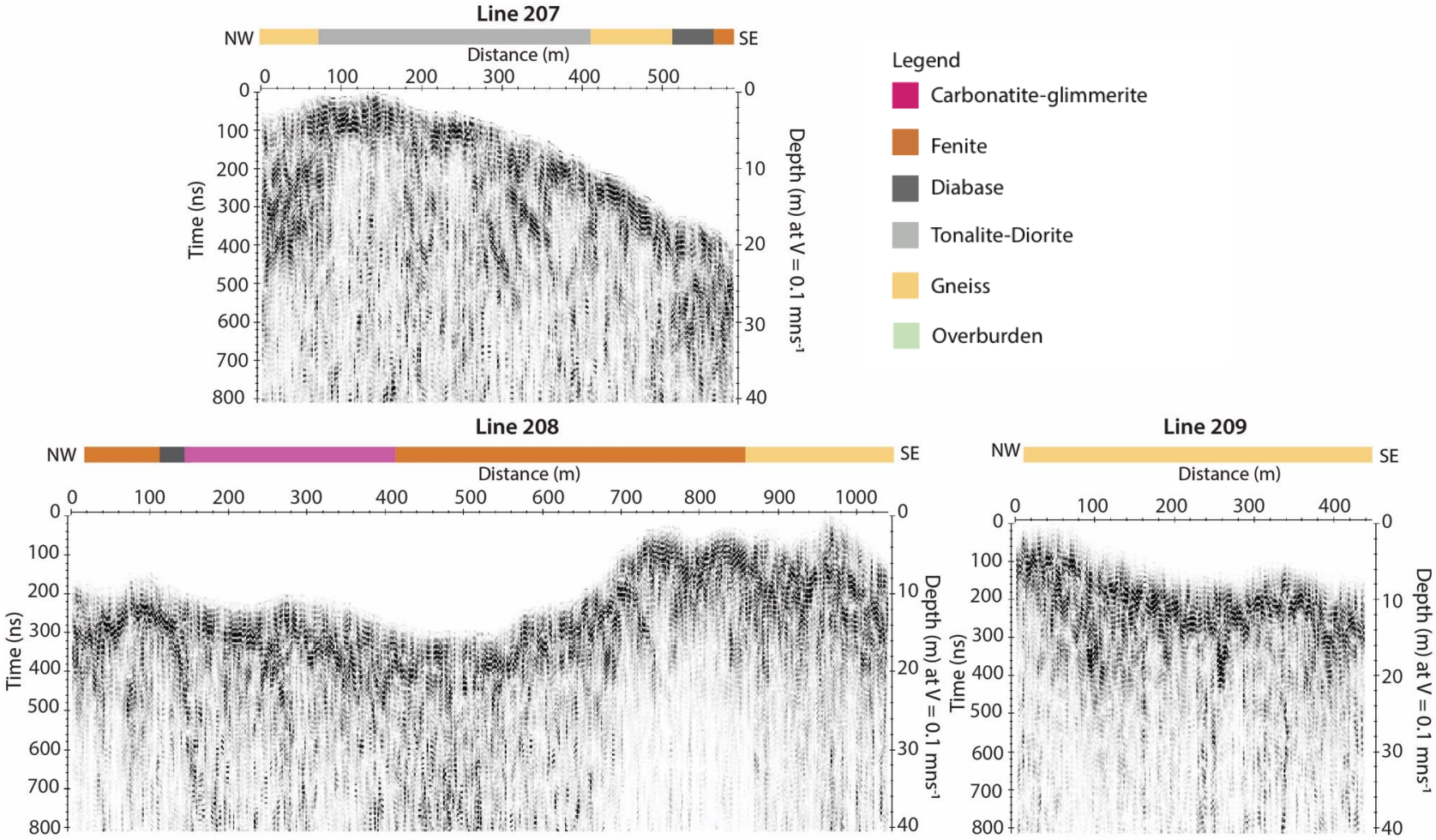

Figure 37. Processed GPR lines; 207 (upper), 208 (lower left) and 209 (lower right) acquired from along seismic profile SM2. Geology bar have been extracted from surface geology information. See Figure 34 for the geology and GPR line locations.

5 MAGNETIC METHOD

5.1 Fundamentals of Magnetic Method

5.1.1 Theoretical Background

Magnetism and magnetisation are the influential physical phenomena for the magnetic method. All rocks are magnetised to varying extents by the Earth's magnetic field. Magnetic methods measure the magnetic flux density, i.e. the B-field, of the Earth, which is composed of three main components: 1) Earth's main magnetic field (both internal and external), 2) induced magnetisation of Earth's materials and 3) remanent magnetisation of Earth's materials. The main magnetic field, which accounts for ~98% or more of the geomagnetic field (Hinze, et al. 2013, p. 216), originates from the Earth's fluid outer core (the internal field). It is generated and maintained by the convection flow of electric currents in the fluid outer core of the Earth. It can be approximated by a dipole in the centre of the Earth that is tilted 11.5º with respect to the rotational axis. The intensity of the main magnetic field varies and is strongest at the poles (~60,000 nT) and decreases towards there equator (~ 30,000 nT) (Campbell 2003, p.7).

Variations in the magnetic field can occur due to several different factors. The main magnetic field (internal field) is slowly changing through time due to the turbulent convection flow. Intense changes in the magnetic field arise when polar reversals occur (longer timescale of ~10,000 years). The externally produced portion of the Earth's magnetic field undergoes more rapid variations due to solar activity, Earth's rotation or human activity (Reynolds, 2011, p. 95). Spatial variations in the magnetic field are caused by inhomogeneities of the Earth's crust (e.g. ore deposits). These inhomogeneities produce anomalies in the Earth's magnetic field as a result of induced and remanent magnetisation. The background physics and theory of magnetics are discussed in greater detail by Campbell (2003) and Reynolds (2011).

The magnetisation of Earth's magnetic minerals by an external magnetic field is referred to as induced magnetisation. The magnetic susceptibility k is a measure of how

susceptible a material is to magnetisation. It specifies the degree of magnetisation $\boldsymbol{M}$ per unit volume (or intensity of magnetisation) as a response to the external field.

$$\boldsymbol{M_i} = k\boldsymbol{H} \tag{5.1}$$

The induced magnetisation $\boldsymbol{M}_i$ is proportional to the applied external magnetic field strength $\boldsymbol{H}$ and the magnetic susceptibility of the material k. This relationship is true for homogenous and isotropic materials.

The dependence between the magnetic field $\boldsymbol{B}$ and the magnetic field strength $\boldsymbol{H}$ is defined as the magnetic permeability in a vacuum ($4\pi \cdot 10^{-7}$ NA^{-2}):

$$\boldsymbol{B} = \mu_0 \boldsymbol{H} \tag{5.2}$$

where the magnetic susceptibility is $k = 0$ and relative permeability is $\mu_r = 1$.

The magnitude of the induced and remanent magnetic fields is dependent on the magnetic susceptibility, spatial distribution and concentration of the local crustal magnetic materials. Materials can be classified based on their magnetic properties, as being dia-, para-, ferro, or ferri-magnetic. Dia- and paramagnetism only exist in the presence of an external field, therefore the magnetisation is linear in relation to the field strength (Schön, 2011, p. 375). (Reynolds 2011. Both dia- and paramagnetism result in low magnetic susceptibilities. Ferro- and ferri-magnetic materials have the highest magnetic susceptibilies. In addition, they may also acquire a remanent magnetisation, i.e. be permanently magnetised in the absence of an applied, external field (Reynolds 2011, p. 85). The magnetisation and susceptibility of ferro- and ferri-magnetic materials is largely dependent on temperature. When the temperature reaches above Curie temperature for ferro- and ferromagnetic material, the material then has paramagnetic properties (Schön 2011, p.376).

Variations in the induced and remanent magnetisation create magnetic anomalies. These characteristics can be utilised for mineral exploration purposes. The magnetic method can be used to detect local changes in the magnetic field, which indicates variations in the

concentration of magnetic minerals in the subsurface. The induced anomalies are dependent on the direction of the Earth's magnetic field. The anomalies can have both positive and negative peaks, due to the dipolar nature of the Earth's magnetic field. Several factors can impact the shape of a magnetic anomaly in addition to the magnetic susceptibility that controls the strength of the anomaly, e.g. the latitude, depth, strike and dip angle of the detected magnetic body. Sharp anomalies occur if the magnetic body is small and is close to the surface, whereas broader and smoother anomalies occur if the magnetic bodies are deeper. Therefore, it is possible to estimate the depth to a magnetic body based on the shape of the anomaly. However, if remanent magnetism is also present, the shape of the anomaly can be affected significantly which will complicate the interpretation (Reynolds, 2011, p. 112, Green, 1960). To prevent misinterpretation, the intensity and direction of the remanent magnetism should be determined.

5.2 Acquisition of Magnetic Data at Siilinärvi

Near-surface magnetic data was collected along the seismic profile SM2 (Figure 38). Two magnetometers were used in the survey; one to acquire the total field magnetic data along the survey line, and another one was set up as a base station to record the total field daily variation (Figure 39). Data collection was carried out by MSc students from Uppsala University who then provided the data for this thesis.

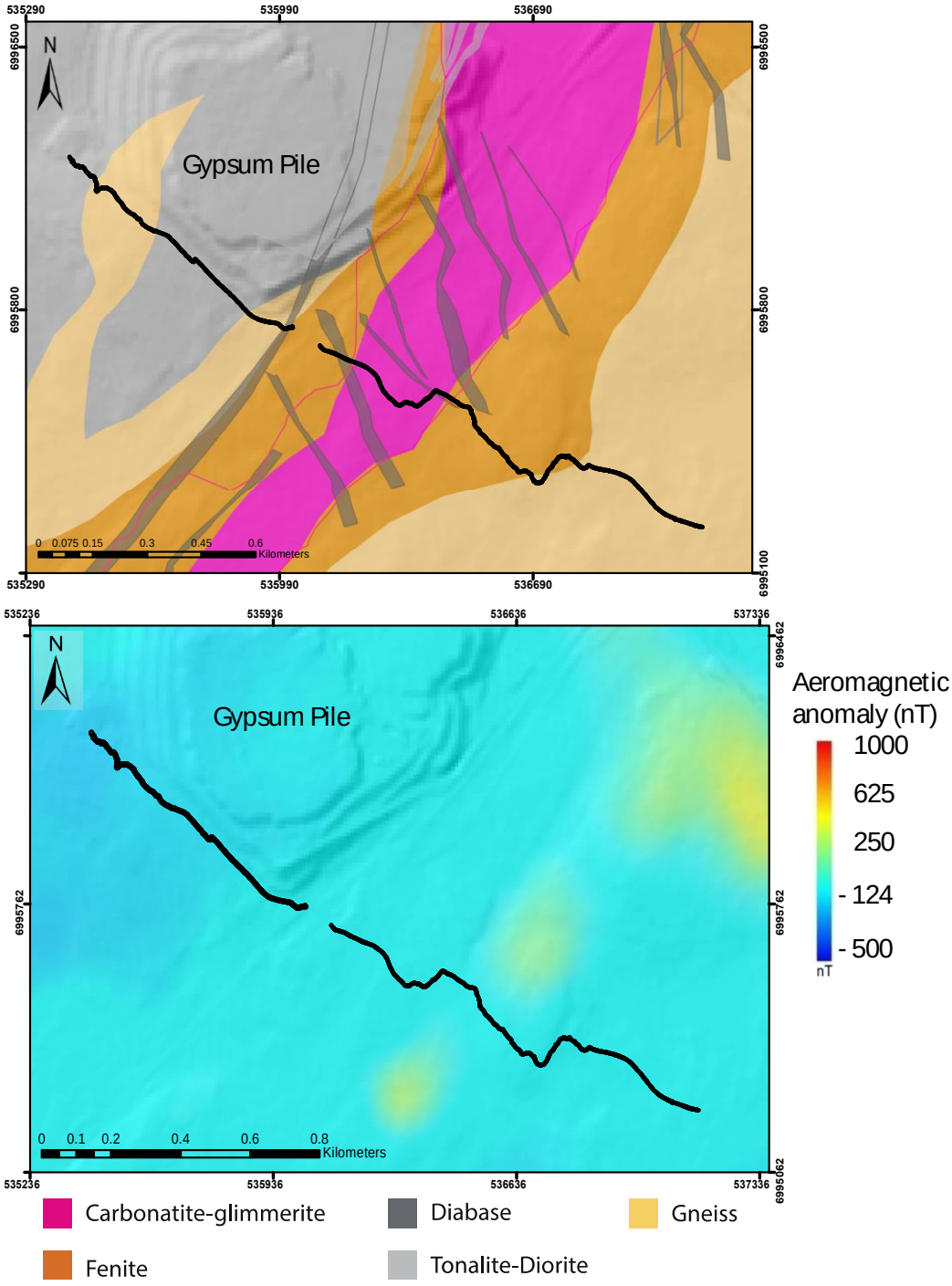

Figure 38. Magnetic survey line acquired along SM2 (upper) overlain on a geology map of the survey area and (lower) overlain on an Aeromagnetic anomaly map. Coordinates are in the EUREF-FIN ETRS-TM35FIN system. Geology from Yara. Aeromagnetic anomaly map of Finland © Geological survey of Finland 2007. Base map: Elevation model 2008-2019, 2 m x 2 m, © National Land Survey of Finland.

A GEM GSM-19 Overhauser magnetometer owned by the Uppsala University was used to carry out the measurements. This magnetometer works by exploiting the nuclear Overhauser effect by utilising a radio frequency (RF) magnetic field. A liquid containing

free, unpaired electrons is combined with hydrogen atoms and the mixture is exposed to the external RF magnetic field. This causes the unpaired electrons in the liquid to transfer energy to the protons (Overhauser effect) which results in the alteration of the spin state of the protons, thus polarizing the liquid. When the external field is removed, the protons precess and realign with the Earth's magnetic field. The frequency of precession f_p, known as Larmor precession frequency, is proportional to the total magnetic field *B*.

$$B = 2\pi f_p / \Upsilon_p \qquad (5.3)$$

Where $\Upsilon_p$is the gyromagnetic ratio of the proton and $2\pi f_p / \Upsilon_p$ is equal to 23.487 ± 0.002 nTHz^{-1}.

Figure 39. Field photograph of magnetometer used as base station to records daily fluctuations in the total magnetic field.

The GEM GSM-19 Overhauser magnetometer has a resolution of 0.01 nT and an absolute accuracy of +/- 0.1 nT. Total field measurements were taken along the survey line using "walking" mode and a single sensor with a sampling rate of 1s. An AC filter of 50 Hz was used. A high-resolution (0.6 m) GPS which is integrated within the magnetometer

was utilised to record the coordinates of the acquired measurements. The parameters used for this survey are summarised in Table 3.

Table 3. Survey parameters of magnetic measurements carried out by Uppsala University students in Siilinjärvi, 2018.

Survey Parameters	
Type of survey	Single sensor, 2D total field (nT) magnetic profiles
Total length of survey lines	~ 2 km
Survey Equipment	GEM GSM-19 Overhauser magnetometer
Survey Mode	Walking mode
Measurement sampling rate	1 s
Base station sampling rate	20 s
AC filter (survey and base station equipment)	50 Hz

5.3 Processing of Magnetic Data

For the magnetic data, it was essential to remove noises caused by elements unrelated to the subsurface magnetism. To do this, the processing flow presented in Figure 40 was applied to the dataset.

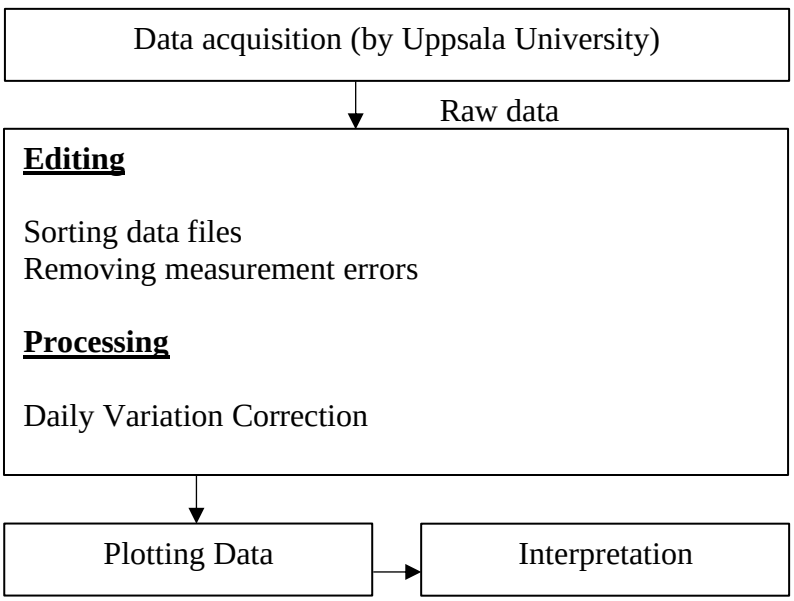

Figure 40. Processing flow for magnetic data acquired at the Siilinjärvi mine site.

The recordings from the base station how that the total magnetic field (nT) fluctuated with time (Figure 41). These measurements were used to correct the survey measurements for the daily variations in the magnetic field. Deviations of the total magnetic field were interpolated with time to obtain the correction required to remove this variation from the measurements acquired along SM2. Additional editing of the dataset was required to remove spikes, possibly caused by surface artefacts such metal pipes.

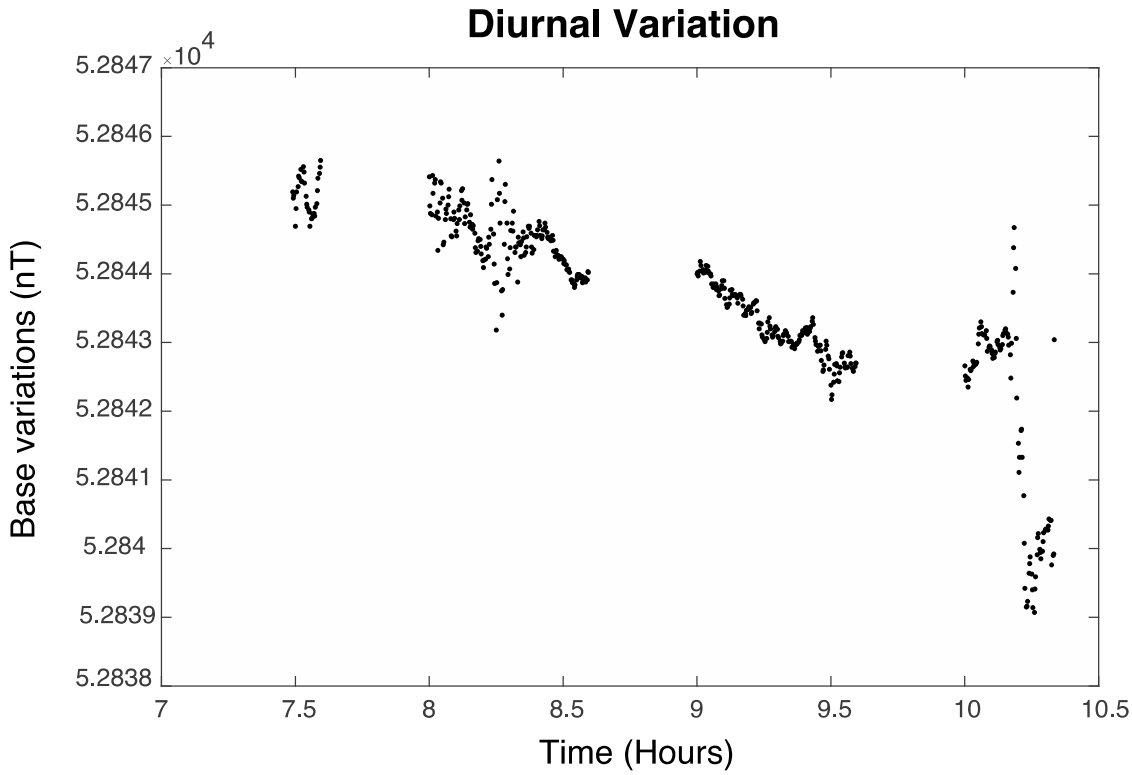

Figure 41. Magnetic total field (nT) measurements recorded by the base station showing fluctuations in the measurements with time.

The uncorrected and corrected measurements are presented in Figure 42. A geological bar based on the surface geology is displayed above the plot to aid in the interpretation. The gap in the data observed at approximately 800m along the survey line is due to the presence of a road.

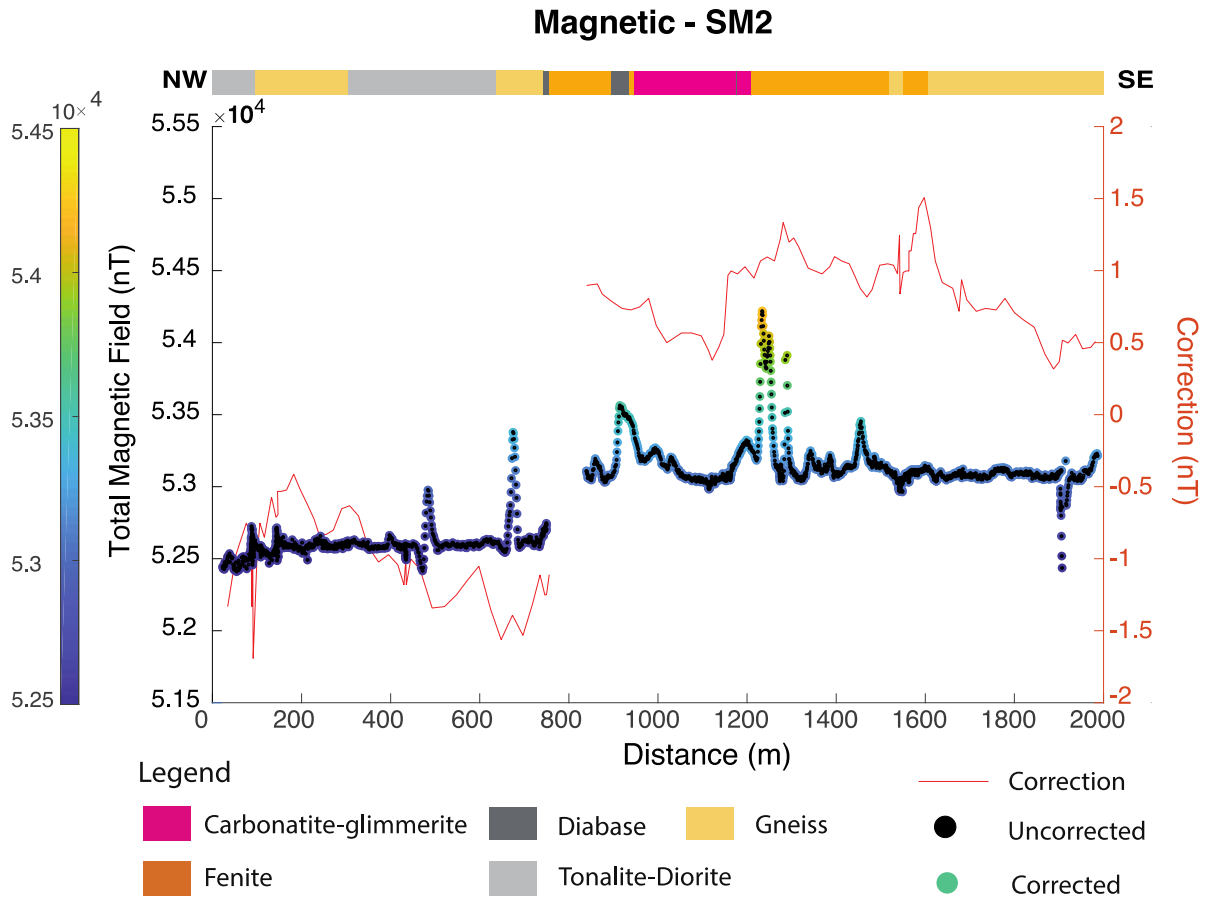

Figure 42. Magnetic total field (nT) measurements acquired from the magnetic survey along survey line SM2. Uncorrected data and corrected data are plotted along with the correction of the daily variation of the magnetic field. The survey line location is shown in Figure 39.

6 RESULTS AND INTERPRETATION

In this chapter, the processed seismic, GPR and magnetic data are presented, and interpretations of the results are presented in conjunction with the available geological data from the survey area. The geological data include: borehole information and surface geology information.

6.1 Reflection Seismic Data

As discussed in section 3.1.2, seismic reflections may occur at interfaces of contrasting physical properties such as lithological contacts or shear zones. The occurrence of a reflection is dependent on the magnitude of contrast across the interface, specifically on the contrast in acoustic impedance. Seismic profiles SM2 and SM3, are known to cross several lithological boundaries (Figure 18). From the physical property study conducted by Malehmir et al. (2017) (see section 2.2.2), typical acoustic impedances of the various rock types found in the study area were estimated based on the P-wave velocity and density measurements (Table 4).

Table 4. Estimated P-wave velocity (ms^{-1}) and density (kgm^{-3}) values for the rock types found in the Siilinjärvi mine area. Values were taken from the physical property study carried out in the mine area by Malehmir et al. (2017) (Figure 6).

Rock Type	P-wave Velocity (ms^{-1})	Density (kgm^{-3})
Carbonatite-Glimmerite ore	5000 - 6500	2800-2950
Fenite	5200- 6100	2500-2700
Diabase	4600- 6500	2750-3200
Diorite	5400- 6400	2600-2900
Granite	4200-5800	2500-2800
Gneiss	3200-4800	2500-2900

Reflection coefficients of possible geological contacts in the study area were calculated from the available P-wave velocity and density estimates (section 3.1.2) using Equation 3.7. These calculations indicate whether or not reflections are theoretically possible at the various rock interfaces. As discussed in section 3.1.2, the approximate minimum value

for a reflection to occur is 0.06 (Salisbury et al. 1996). The estimated reflection coefficients (Table 4) indicate that reflections should occur where carbonatite-glimmerite and diabase are in contact with tonalite-diorite, fenite, granite, gneiss and each other. An interface of fenite and diorite is estimated to have the lowest average reflection coefficient, indicating that reflection event will not occur at this boundary. As can be seen in Table 4, there is a wide range of variability in density and seismic velocity within the same group of samples, resulting in a range of reflection coefficient estimations (Table 5). Therefore, in some cases the velocity and/or density values across an interface may be similar and will not result in a reflection. One factor which was by Malehmir et al. (2017) noted to have an impact the acoustic impedance of the materials was porosity. Areas of fracturing or shear zones therefore could produce reflections if the contrast in acoustic impedance is large enough (Malehmir et al. 2017). Carbonatites in the Siilinjärvi mine area, which are not next to fenite, generally show better rock quality in comparison to diabase (Malehmir et al. 2017).

Table 5. Estimated reflection coefficients for seismic waves at interfaces of different rock types. Calculations were carried out with Equation 3.7 using the P-wave velocity and density values presented in Table 4.

Lithological Interface	Reflection Coefficient R (-1 to +1)	Average R
Diabase - Diorite	± 0.03 to ± 0.05	0.05
Diabase - Gneiss	± 0.17 to ± 0.22	0.2
Diabase - Granite	± 0.09 to ± 0.1	0.1
Diabase - fenite	± 0.09 to ± 0.14	0.5
Ore - Diorite	± 0.0 to ± 0.02	0.01
Ore - Diabase	± 0.04 to ± 0.05	0.05
Ore - Gneiss	± 0.15 to ± 0.27	0.22
Ore – Granite	± 0.07 to ± 0.14	0.11
Ore - Fenite	± 0.04 to ± 0.16	0.11
Fenite- Diorite	± 0.01 to ± 0.09	0.05
Fenite - Granite	± 0.01 to ± 0.11	0.06
Diorite - Granite	± 0.07 to ± 0.14	0.11

6.1.1 Seismic line SM2

Multiple reflection events are visible along seismic profile SM2. Upon inspection of the final migrated stack (Figure 43), lateral variations in reflectivity behaviour are observed across the profile. Based on these lateral variations, the profile can be divided into three separate parts; the western side of the profile where we see a ‘wedge’ of high reflectivity (TD, Figure 43) surrounded by lower reflectivity (G1, Figure 43), the low reflectivity area in the eastern section of the profile (G2, Figure 43) and then the more complex reflective section in the centre (CG1, CG2 and M, Figure 43). The depth extent achieved is much greater than what was required for this survey and deeper than the mineable depths (< 1 km). Intense reflections are seen to continue to a depth of approximately 4 km.

The most intensely reflective area on profile SM2 is observed in the centre of the profile (CG1, Figure 43). In this area, a complex reflective pattern, which includes multiple sub-

horizontal and dipping reflections in the near surface, is observed. Based on the surface geology, borehole lithology and reflective response, this area is interpreted as carbonatite-glimmerite. Boreholes in this area are relatively shallow in comparison to boreholes in and close to the mine area, therefore, borehole lithology information in this area is limited. However, near-surface borehole information shows that the carbonatite-glimmerite unit is intruded by several diabase dikes, some of which correlate with the location for dipping reflections in the data (DD2, Figure 43). A similar reflective pattern was observed along seismic profile SM1 by Laakso (2019), where near surface reflections were found to correlate well with features in the waste-rock dike network 3D model created by Kauti et al. (manuscript in preparation). By comparing the reflective pattern to what is observed along SM1, the sub-horizontal reflections on SM2 are interpreted as being a network of diabase dikes which cut through the carbonatite-glimmerite deposit. The physical properties of diabase and carbonatite-glimmerite (Table 5) indicate that the occurrence of a reflection event is possible at the interface these two lithologies. The reflective package is constrained at a depth of approximately 600 m by a SE dipping bottom reflector. It is unclear as to what this feature is and boreholes in the area do not reach this depth to determine the nature of it (Figure 43).

Within the area of carbonatite-glimmerite, a seismically quiet area is observed between approximately CMP 300 and CMP 340 and extending to a depth of approximately 400 m (CG2, Figure 43). The lack of reflection events in this area may be due to the presence of more homogenous carbonatite-glimmerite.

To the west of the reflective package, a NW dipping feature is observed in the data (DD3, Figure 43). Based on the physical properties (Table 5), this feature is interpreted as a possible diabase dike. However, there is no borehole information in this. It is possible that it is a possible fault or fracture zone. Further information from drill holes, such as RQD and lithology information, is required to confirm the nature of the reflection.

In contrast to the highly reflective area in the centre of the profile, a less reflective area is observed to the west (G1, Figure 43). In the near surface, a zone of increased reflectivity occurs (TD, Figure 43). Based on the surface geology, this zone is interpreted as being a wedge of tonalite-diorite which has intruded into an area of gneiss. Unfortunately, there

is no borehole information available in this area to confirm the presence of these units in the subsurface. However, the occurrence of a reflection at the interface of these two rock units is expected based on the values obtained in Table 5. Contacts of the gneiss and tonalite-diorite occur further west away from profile SM2 and therefore are not visible in the data. It is also possible that the gneiss continues deeper than what is outlined in Figure 43, however, the interpretation of the data is focused in the upper section of the seismic profile.

Borehole information from this area shows that the western extent of the carbonatite-glimmerite is complex and is composed of an assortment of various rock units, altering between carbonatite-glimmerite, fenite and granite-gneiss, with granite-gneiss being most abundant (M, Figure 43). This variation in rock units may also account for some of the reflections observed in the complex reflectivity package associated with the carbonatite-glimmerite area. As can be seen in Table 5, reflections are likely to occur at interfaces of these rock types. There is no sharp boundary observed in the area west of the deposit.

On the eastern side of SM2, the carbonatite-glimmerite deposit an area of high amplitude reflections is observed between approximately CMP 360 and CMP 420 (Fe, Figure 43). This area dips towards the SE and extends to a depth of approximately 500 m. It is unclear what causes these reflections. Based on the surface geology, the high amplitude reflections are interpreted as possibly being an area of fenite which is in contact to the eastern side of the deposit. There is no borehole information in this area to confirm this contact. This boundary east of the deposit seems to be sharper in comparison to what is observed to the west. Physical property information indicates that if the boundary is sharp, strong reflections are possible at a boundary of cabonatite-glimmerite and fenite, as can be seen in Table 5.

Lower-reflectivity is observed to the east of stack (G2, Figure 43). This area of is interpreted as being gneiss, based on the borehole lithology and surface geology. A possible dipping feature is seen to cut through this section, dipping in roughly a western direction (F2, Figure 43). This feature seems to break through the surrounding reflectors. Based on this behaviour, the feature is interpreted as being a possible fault or shear zone.

However, there is no evidence of this observed on the surface. It is also possible that the feature is a diabase dike.

A dipping feature is observed cutting through the carbonatite-glimmerite and 'mixed' zone (F1, Figure 43). It is not clear as to what this feature is, possibly a fault or shear zone or a diabase dike.

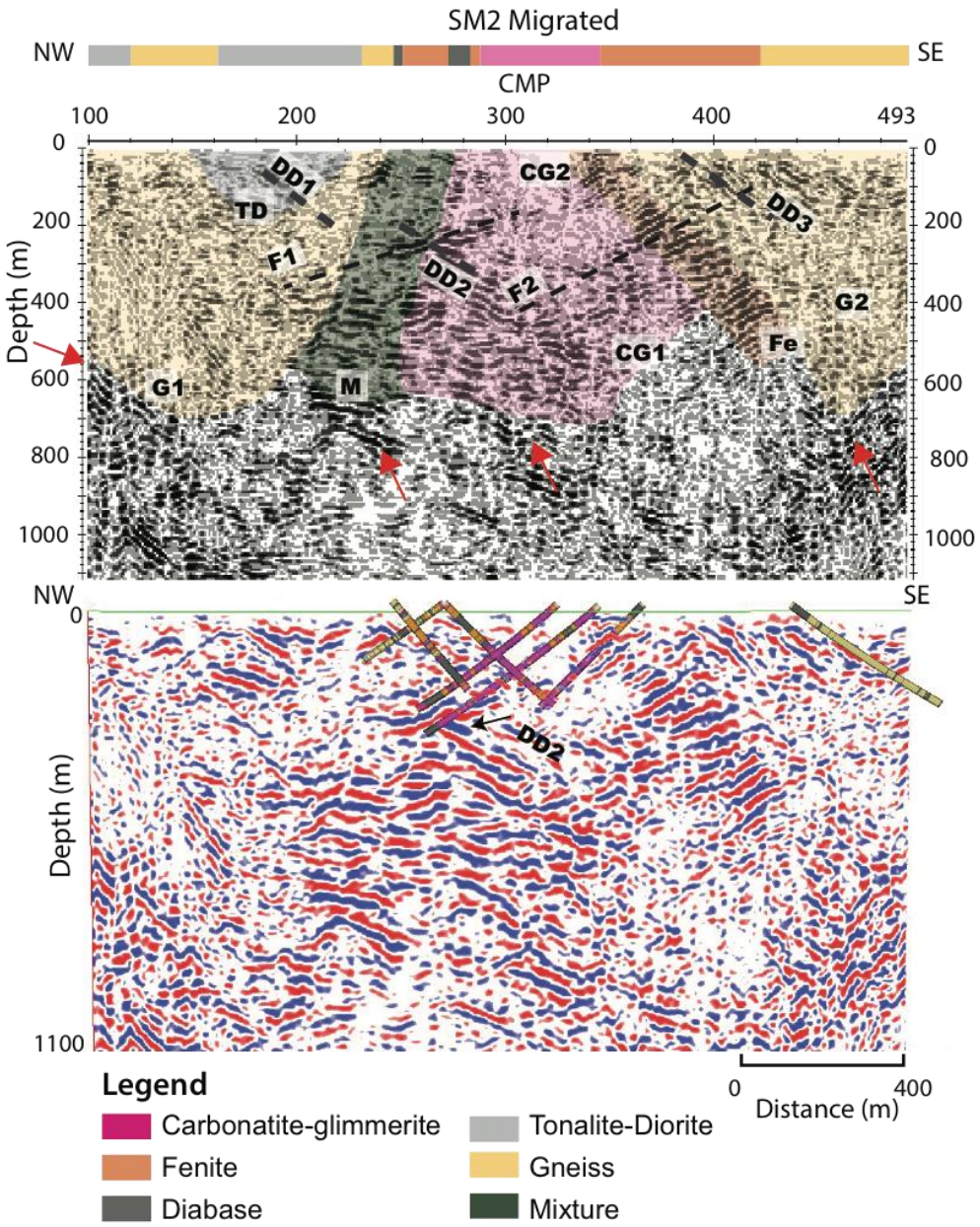

Figure 43. (Upper) Migrated stack from survey line SM2. Kirchhoff's migration algorithm was used for migration. To improve the display, post-stack processing tools such as f-x deconvolution, additional filtering, balancing and AGC have been applied. Interpretation labels; DD: Possible Diabase Dike, CG: Carbonatite-Glimmerite, F: Fenite, G: Gneiss, TD: Tonalite-Diorite F: Possible Fault or Fracture zone and M: area where there is a mixture of rock units). Red arrows indicate unknown bottom reflectors. The geology bar displayed

above the stack was extracted from the known surface geology (Figure 18). (Lower) SM2 with the available borehole information.

6.1.2 Seismic line SM3

Seismic profile SM3 is less reflective in comparison to profile SM2 (section 6.1.1). The most intense reflections appear at a depth of 2.5 km to 3.5 km (Figure 31). Reflection events are mainly confined to the SW section of the profile and the occurrence of events decreases towards the NE. This result was anticipated for seismic line SM3 as the contact to the carbonatite-glimmerite complex curves away from the line towards the west when moving northwards. Data quality of the profile is also lower in comparison to that of profile SM2. One possible explanation for this is that the profile was located next to the road, which may have affected the signal-to-noise ratio. The change in the seismic source along the survey line may have also impacted the signal-to-noise ratio of the profile (Figure 13).

On the profile, a highly reflective area composed of multiple sub-horizontal reflections occurs in the SW section (CG, Figure 44). This end of the profile perpendicularly crosses the middle of profile SM2 (Figure 18), where a similar reflective package is also observed. These reflective areas correlate well with one and other and are interpreted as a part of the carbonatite-glimmerite unit based on the borehole information (section 6.1.1). As was discussed previously, the sub-horizontal reflections associated with the carbonatite-glimmerite, are interpreted as being caused by a diabase dike network within the complex. As was the case for SM2, boreholes show the occurrence of fenite and gneiss within the carbonatite-glimmerite which may also account for some of the reflectors. The reflective package associated with carbonatite-glimmerite is observed between approximately CMP 100 and 500, due to the curving of the deposit. Surface geology between CMP 100 and 300 alternates between fenite and diabase. However, borehole information reveals that fenite and diabase occur only in the near surface and the carbonatite-glimmerite deposit is present at deeper depths below these units (Figure 44). The fenite and diabase at the surface are not observed in the reflection seismic data due to the scale.

The NE side of the profile is quieter in terms of seismic reflections, which based on the

surface geology, is interpreted as being due to the presence of fenite.

A clear dipping reflector is observed at approximately CMP 420 (R1, Figure 44). It is unclear if this reflection is caused by the presence of a diabase dike or a fracture zone.

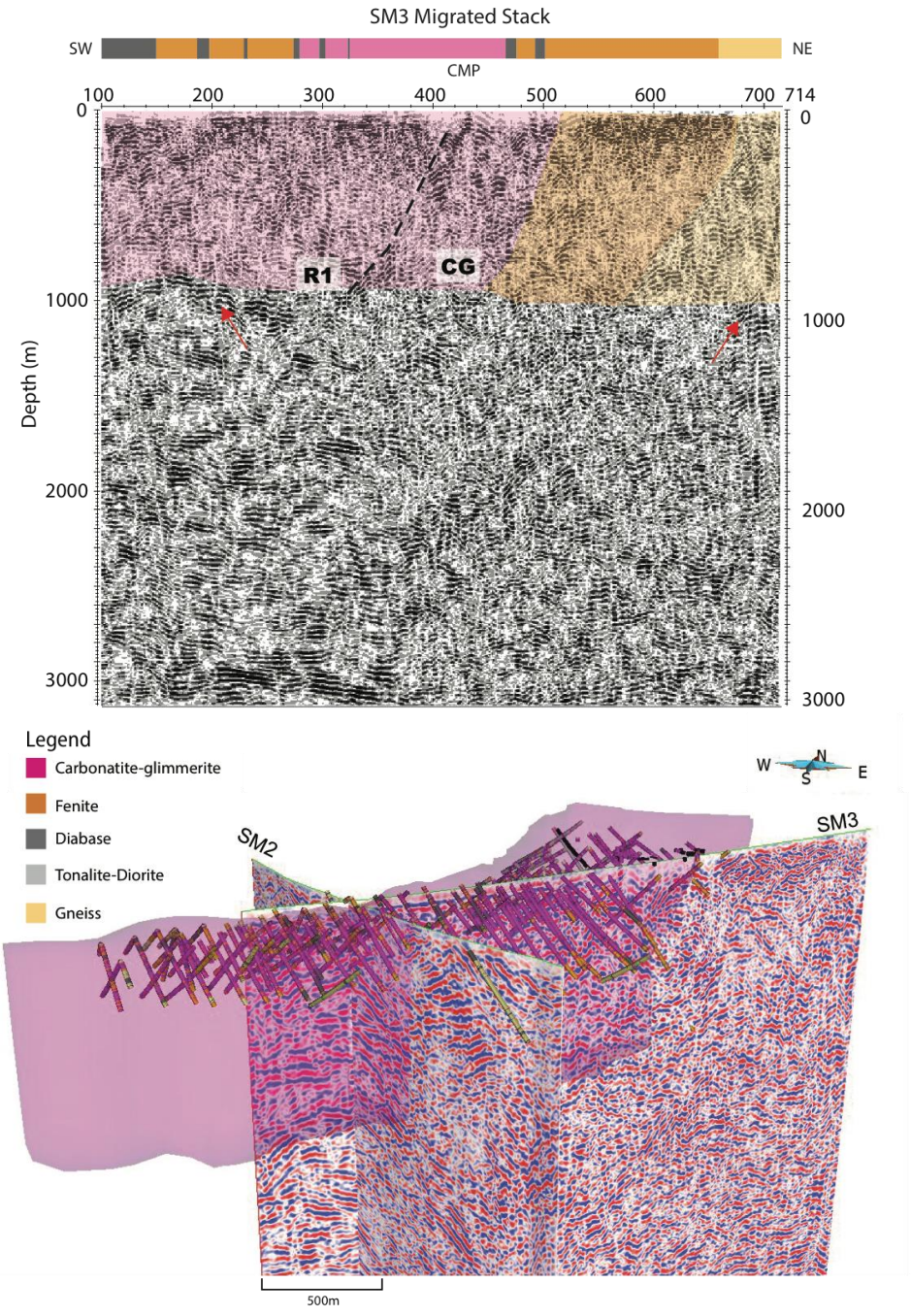

Figure 44. (Upper) Migrated stack from survey line SM3. Kirchhoff's migration algorithm was used for migration. To improve the display, post-stack processing tools such as f-x deconvolution, additional filtering, balancing and automatic-gain control have been applied. CG: Carbonatite-Glimmerite, R1: dipping reflector. The geology bar displayed above the stack was extracted from the known surface geology (Figure 18). (Lower) Profile SM3 and SM2 with borehole lithology information and previous 3D model of the carbonatite-glimmerite deposit (provided by Yara).

6.2 GPR Data

As was discussed in section 4.1.2, reflection events can occur when an EM wave encounters a boundary of contrasting dielectric properties, such as variations in the water content, density and/or lithology. The degree of contrast in the dielectric properties across the boundary dictates if a reflected wave will be produced. Typical relative dielectric permittivity values associated with the rock units in the survey area are presented in Table 6.

Table 6. Estimated relative dielectric permittivity values for the rock types found in the Siilinjärvi mine area. Values were obtained from Maijala, (1991) and Schön (2011a). The relative dielectric permittivity for the carbonatite-glimmerite found in the Siilinjärvi mine area was estimated based on the mineral compositions from O'Brian et al. (2015) (Mica: 5%, Amphibole: 8%, Calcite: 6.35%, Dolomite: 7.46 %, apatite 11.7%). The relative dielectric permittivites of the minerals are from Olhoeft, (1981), Schön (2011a) and Dye & Hartshorn (1924).

Rock type	**Relative Dielectric Permittivity (ε_r)**
Carbonatite-glimmerite (Ore)	5.8-6.8
Diabase	9 - 13
Diorite	5.9 -11.5
Fenite	-
Granite	4.5 - 9
Gneiss	8 -15

GPR data acquired along survey line SM2, crosses several changes in lithology. Reflection coefficients of possible geological contacts were calculated with equation 4.5 using the estimated values of relative dielectric permittivities (Table 6), to determine if reflections should theoretically occur at the various interfaces.

Table 7. Calculated reflection coefficient values for different lithological boundaries. Values were carried with Equation 4.5, using the estimated relative dielectric permittivity values presented in Table 6.

Rock type	Reflection Coefficient (+1 to -1)
Diabase- Granite	± 0.12 to 0.17
Diabase- Diorite	± 0.06 to 0.11
Diabase- Gneiss	± 0.03 to 0.04
Ore-Diabase	± 0.11 to 0.14
Ore-Gneiss	± 0.08 to 0.15
Ore-Granite	± 0.02 to 0.06
Ore-Diorite	± 0.00 to 0.13
Diorite-Granite	± 0.06 to 0.07

Based on the estimated reflection coefficients presented in Table 7, the largest contrasts are seen to be between carbonatite-glimmerite and diabase, carbonatite-glimmerite and gneiss, diabase and granite and diabase and diorite. Therefore, a reflection is likely to occur at these interfaces. Fenite is not represented in Table 7, however similar values to granite can be assumed due to granite being the protolith rock. Based on Table 7, there would be a contrast in properties at a contact of fenite and carbonatite-glimmerite or fenite and diabase and therefore, a reflection may occur.

As can be seen in Table 7, for each rock unit there is a range of possible values. Additional factors such as fracturing or water content can further impact the dielectric properties and the resulting reflection coefficient. Therefore, in instances where the dielectric properties across the boundary are too similar, a reflection event will not occur.

6.2.1 GPR along SM2

The GPR profiles acquired along seismic line SM2 revealed several areas of complex reflectivity. The overburden layer seems to fluctuate along the line and was interpreted as being approximately 1-2m thick (Figure 45). This correlates with the Quaternary

deposit thickness map presented by Luoma et al. 2014 (see section 2.2.3), where the overburden thickness in the areas beside the gypsum pile is stated to vary between approximately 1 to 6m. The Quaternary sediment in the areas around the gypsum pile is reported as being predominantly fine-grained sediment, mostly clay. The water content in this area is reported as being relatively high, based on the information from the nearby wells. The highly conductive media present in this area may have impacted the penetration of the GPR signal. However, a good depth of penetration was still achieved. The depth of penetration along the line was approximately 20m. The depth is based on a velocity of 0.1 $mns^{-1.}$

Interpretation of the GPR profiles is based on the surface geology. Lateral variations in reflectivity occur across the GPR profiles. Changes in reflectivity seem to coincide with changes in the surface geology. Areas of high reflectivity are observed within fenite and carbonatite-glimmerite (CG, Figure 45). As discussed in section 6.1.1, the available borehole information along survey line SM2 shows complex variations in the geology on the western side of the carbonatite-glimmerite deposit. Reflections within the fenite and carbonatite-glimmerite possibly result from these variations in geology or the occurrence of diabase dikes.

Reflections are also observed within the gneiss (G1a, G1b and G2, Figure 45). Borehole lithology logs show diabase dikes within the gneiss, and these reflections may be caused by diabase dikes intruding into the gneiss. In addition, reflections may also occur as a result of fracturing and/or weathering of the gneiss. There is a contrast between the highly reflective gneiss and a less reflective area of tonalite-diorite (TD, Figure 45). The tonalite-diorite may be less weathered or fractured in comparison. Two prominent dipping reflectors are observed within the area the area of tonalite-diorite (DD1 and DD3, Figure 45). There is no borehole information for this location however, based on the physical property information (Table 7), the features are interpreted as being possible diabase dikes.

As illustrated Figure 45, additional dipping reflectors are observed in the GPR data which also interpreted as diabase dikes (e.g. DD3, Figure 45). Two of the features coincide with the locations of diabase dikes in the surface geology (DD4 and DD5, Figure 45).

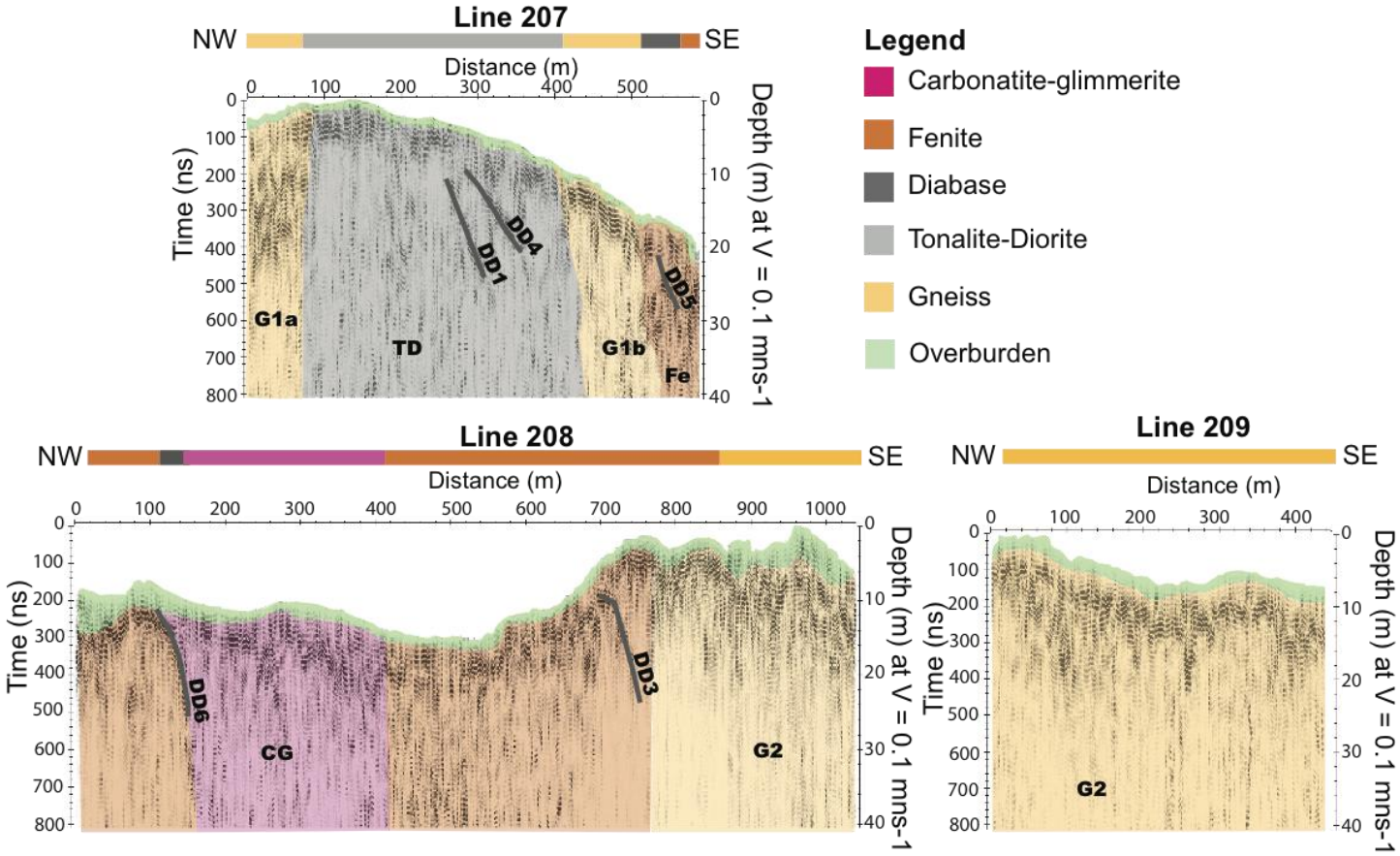

Figure 45. Interpreted GPR lines 207, 208 & 209, acquired along seismic line SM2. Lettering based on interpretation: G: Gneiss, DD: possible Diabase Dike, F: possible fault or fracture zone Fe: Fenite, CG: Carbonatite-Glimmerite, TD: Tonalite-Diorite

6.3 Magnetic Data

The magnetic method is sensitive to variations in magnetic susceptibility and remanent magnetism of the subsurface geology (section 5.1.1). Magnetic susceptibility measurements were acquired as part of the physical properties study carried out by Malehmir et al. (2017) (section 2.2.1). Higher values of magnetic susceptibilities are associated with carbonatites (Figure 7). Magnetite is the most common accessory mineral in the carbonatite-glimmerite in Siilinjärvi, which accounts for these elevated values of magnetic susceptibility. The effect of remanent magnetization on the total magnetic field measurements was not considered for this work as no data was available.

The magnetic profile obtained along survey line SM2 shows that the total magnetic field fluctuates along the line. The results were combined with surface geology information to determine the magnetic signature associated with each rock type (Figure 46). Overall, the magnetic response along the line shows an increase in values towards the carbonatite-glimmerite deposit. In comparison, the beginning of the profile is relatively stable where the surface geology is tonalite-diorite and gneiss, and the end of the profile where gneiss occurs. The elevated values associated with the carbonatite-glimmerite deposit, therefore makes it easily distinguishable from the surrounding tonalite-diorite and gneiss.

The increase in the magnetic total field measurements associated with the carbonatite-glimmerite deposit is likely due to the magnetite content of the deposit. Fluctuation within the deposit indicates variations in the magnetite content. As can be seen in the results (Figure 46), the largest peak in the magnetic profile, with values in the range of 5.3-5.35 x 10^4 nT, occurs at approximately 1250m.

At approximately 1490 m along the survey line, elevated values are observed at a contact between fenite and gneiss. Other fluctuations along the profile are possibly due to contacts in the geology or diabase dikes crosscutting the rock in the subsurface. Possible signatures of DD1 and DD4 interpreted in the GPR data (Figure 45) have been indicated in Figure 46. The general trend across the profile is an overall increase in the magnetic response along the profile, from NW towards the SE.

As can be seen in Figure 46, a ‘step’ in the measured values occurs after the gap in the survey line (at approximately 800 m). It is unclear as to what caused this shift in values.

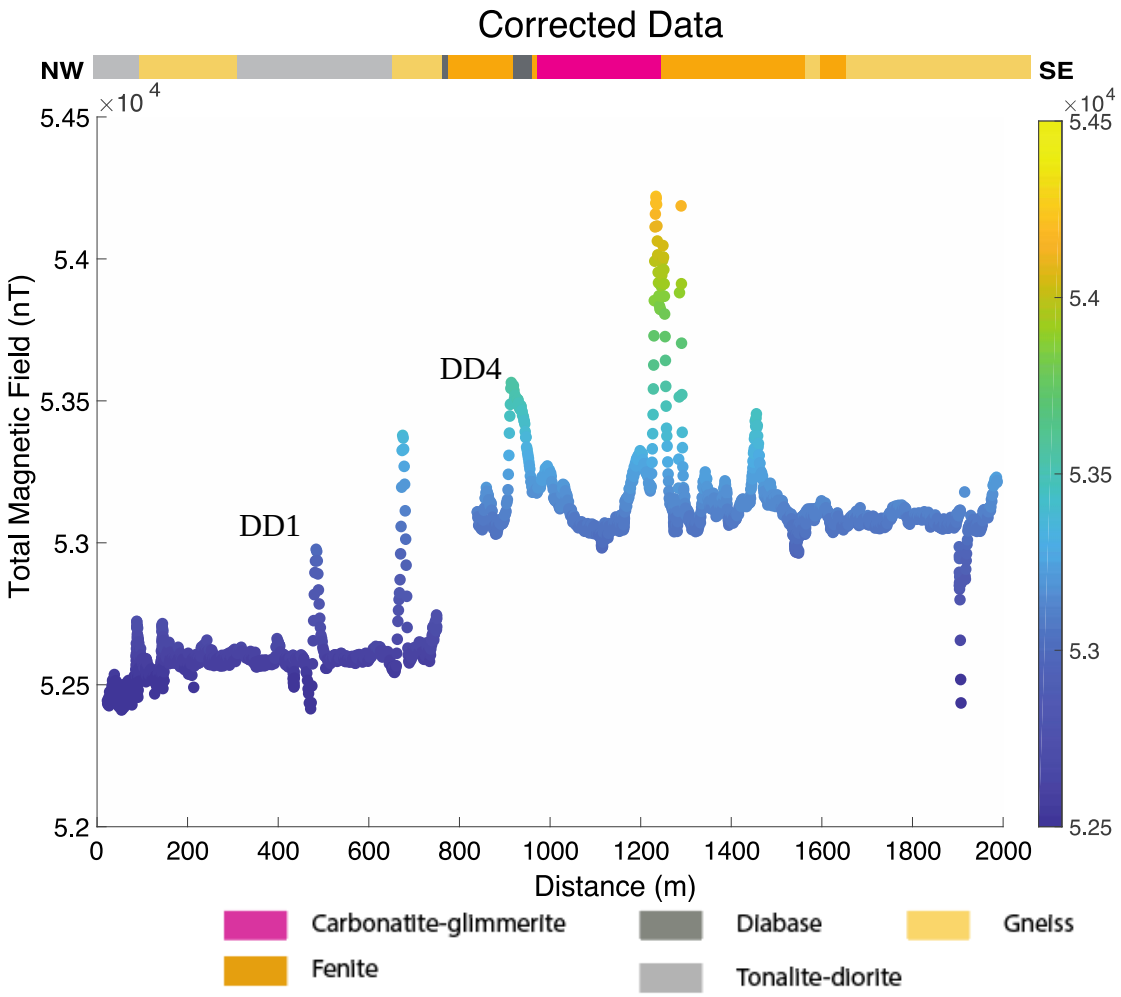

Figure 46. Plot of corrected magnetic data acquired along survey line SM2. The geology bar has been extracted from the surface geology.

7 DISCUSSION

A previous geological model of the southern continuation of the carbonatite-glimmerite deposit was created based on borehole information obtained from earlier exploration efforts carried out in the Siilinjärvi mining area. The survey conducted by Smart Exploration in Autumn 2018 was designed with the aim of expanding on this previous geological model and obtaining further information on the continuation of the deposit south of the main pit. As previously mentioned, the continuation of the deposit under the gypsum pile was of particular interest for this work as this area cannot be reached with drilling. In this chapter, the results obtained from this study will be discussed in further detail. Results obtained from all three of the 2D active-source seismic lines acquired by Smart Exploration (SM1, SM2 and SM3) will be combined in order to obtain a 3D interpretation on the extent of the deposit. A combined interpretation of reflection seismics, GPR and magnetic data will also be discussed in this section.

As stated previously, the MSc thesis work completed by Laakso (2019) tested the applicability of the reflection seismic, GPR and magnetic methods in the survey area. The obtained results were compared with the detailed 3D model of waste-rock dike network created by Kauti et al. (manuscript in preparation). The dibase dike model is based on the exposed geological features observed in the Särkijärvi pit and was created independently of the geophysical data. This provided Laakso (2019) with the opportunity to directly correlate geophysical signals with known geological features, in particular the diabase dikes. Therefore, the geophysical results presented by Laakso (2019) along survey line SM1, acts as an excellent reference for the geophysical results obtained in this work.

7.1 Reflection Seismics and 3D model of the southern extension of the Siilinjärvi deposit

The earlier geological model indicates that the carbonatite-glimmerite deposit extends south of the main pit, perpendicularly crossing seismic lines SM1 and SM2, extending further south beyond the location of SM2 (Figure 47). Seismic profile SM3 runs alongside

the deposit, however as illustrated in the geological model in Figure 47 when looking south, the deposit is seen to curve westwards away from the line.

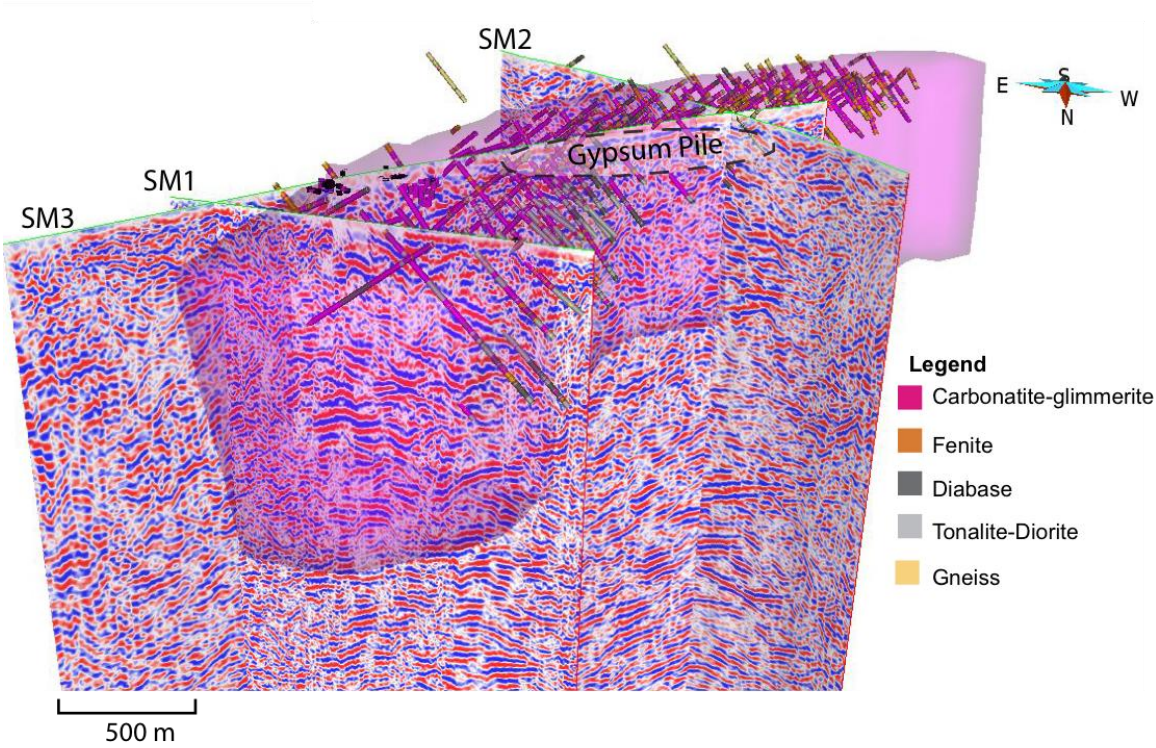

Figure 47. 3D view of the Smart Exploration active-source seismic data (SM1, SM2 and SM3) overlain with the drill hole logs and carbonatite-glimmerite deposit model from the previous geology model (provided by Yara) (View angle to the S). The general location of the gypsum pile is illustrated in the figure for a point of reference.

As can be seen in Figures 47 and 48, the location of the carbonatite-glimmerite deposit in this previous geological model, coincides with areas of complex reflectivity on the seismic profiles (features labelled CG in Figures 43 & 44). The complex reflectivity associated with carbonatite-glimmerite is observed on both profiles where the two survey lines cross perpendicularly. The location at which the profiles cross is situated next to the gypsum pile and occurs outside the extent of carbonatite-glimmerite deposit from the previous geology model (Figure 18). Boreholes are shallow in this area and do not reach deeper reflective areas to confirm the lithology. However, the location of the deposit also coincides with a similar reflectivity pattern observed on profile SM1 (Laakso et al. 2019), where deeper boreholes confirm the presence of carbonatite-glimmerite. Based on the

surface geology, borehole data and physical properties (Table 5), the reflective pattern related to the carbonatite-glimmerite is interpreted as being due to a network of diabase dikes. A connection between the sub-horizontal dike network and near-surface reflections within the carbonatite-glimmerite was observed by Laakso (2019), by correlating the reflection seismic data with the waste-rock dike model created by Kauti et al. (manuscript in preparation).

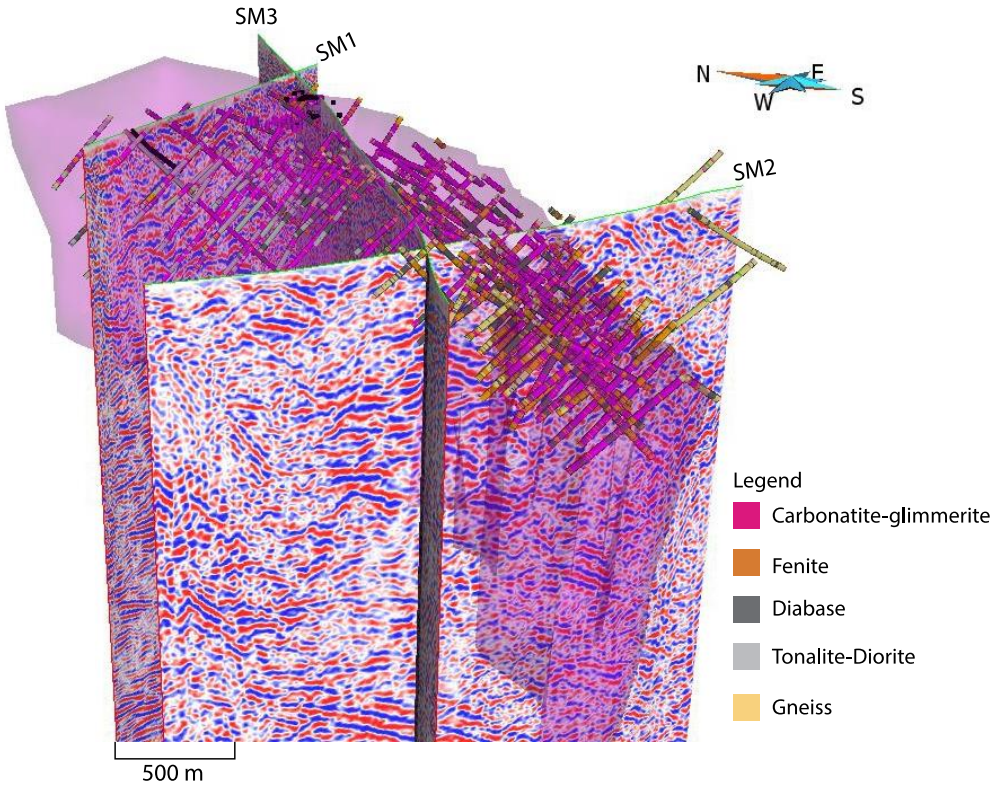

Figure 48. 3D view of the Smart Exploration active-source seismic data which is overlain with borehole information and the carbonatite-glimmerite deposit from the previous geological model (provided by Yara). (Viewing angles is to the NE).

In addition to the diabase dike network, the presence of tonalite-diorite, gneiss and/or fenite within the carbonatite-glimmerite may also account for some of the observed reflections, especially on the western side of the deposit along profile SM2, where the boreholes show significant variations in geology.

Due to the reflective nature of the carbonatite-glimmerite deposit, the extent of the deposit could be picked from all three of the 2D active source seismic profiles (SM1, SM2 and SM3). This, in addition to borehole information, enabled us to create a new updated 3D

model of the carbonatite-glimmerite deposit (Figure 49). The model shows that the southern extension of the deposit is wider in comparison to the previous model. The new model shows that the deposit extends further towards the NW, under the gypsum pile. It is important to note that the new model includes other lithologies, especially the area of complex geology on the western margin of the carbonatite-glimmerite deposit (m, Figure 43). Based on the seismic data, there is not enough information to make reliable predictions on the ore grade at depth.

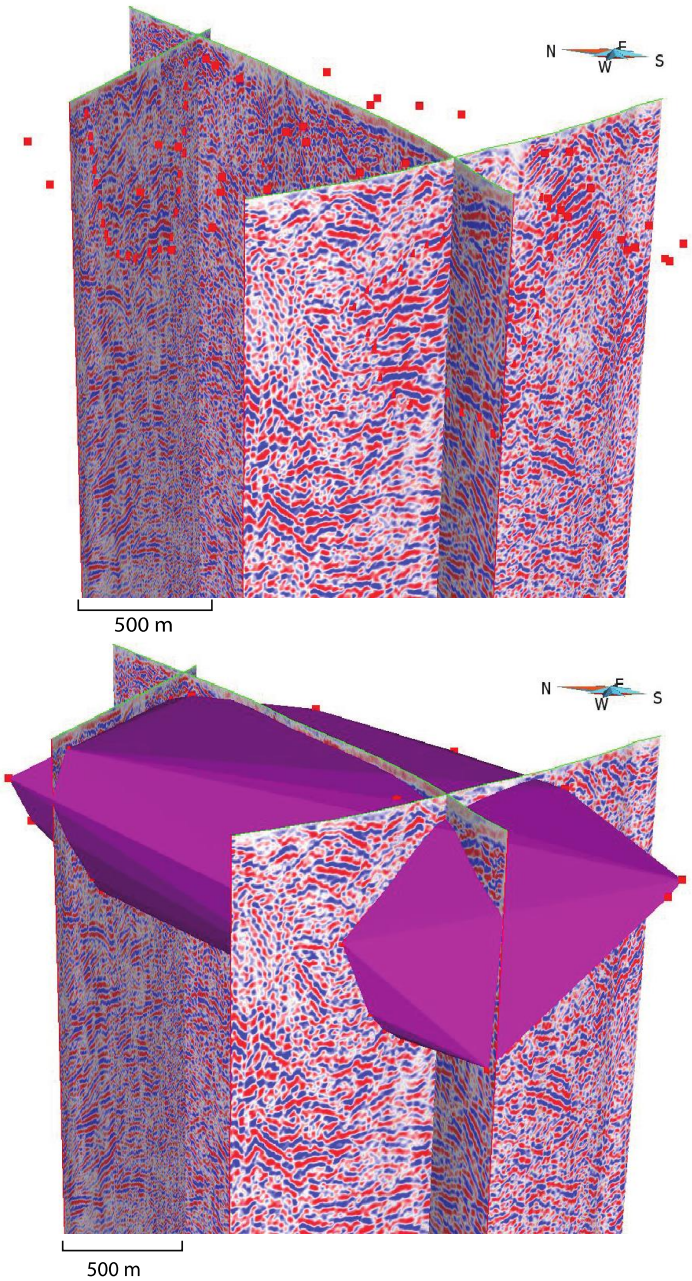

Figure 49. (Upper) 3D view of the seismic data with markers representing the extent of the carbonatite-glimmerite deposit based on the seismic profiles and borehole information (Lower) 3D view of the seismic data overlain with the new 3D model of the carbonatite-glimmerite deposit based on the 'picks' (from seismic data and borehole data) illustrated in the upper image. (Viewing angles is to the NE).

A surface-wave tomography model of the area south of the main Särkijärvi pit was created by Da Col et al. (2019) from the 3D seismic active-source data which was acquired as part of the Smart Exploration field campaign. Both lateral and vertical variations in S-wave velocities were observed in the tomography model. The lateral variations observed by Da Col et al. (2019) generally agree with what was observed in the 2D-active source

seismic lines. In Figure 50, a depth section of the 3D volume at 90 m depth is overlain with the seismic profiles (SM1, SM2 and SM3) and the previous geological model. Lateral variations can be clearly observed in this depth slice. As can be seen in Figure 50, higher velocities occur on the SE section of slice, coinciding with the location of the host rock, granite-gneiss (G2, Figure 50). This is similar to what is observed in seismic profile SM2 (G2, Figure 43) and GPR data (G2, Figure 45). In contrast, lower values are observed in the location of the carbonatite-glimmerite deposit (CG1, Figure 50). This area coincides with the area of complex reflectivity observed on seismic profile SM2 (CG1, Figure 43). The decrease in velocities toward the centre of the complex may be due to carbonatite-glimmerite being more susceptible to weathering and fracturing in comparison to granite and gneiss and thus resulting in a lowering of velocities. Areas of higher velocities are observed within the carbonatite-glimmerite area. Some of these areas coincide with the locations of known diabase dikes (Da Col et al. 2019). One area of higher velocity observed within the carbonatite-glimmerite is seen to correlate with a reflection in seismic reflection profile SM2 (DD, Figure 50). This is possibly a diabase dike. Further research is required to determine if the other areas of increased velocities are due to unmapped dikes.

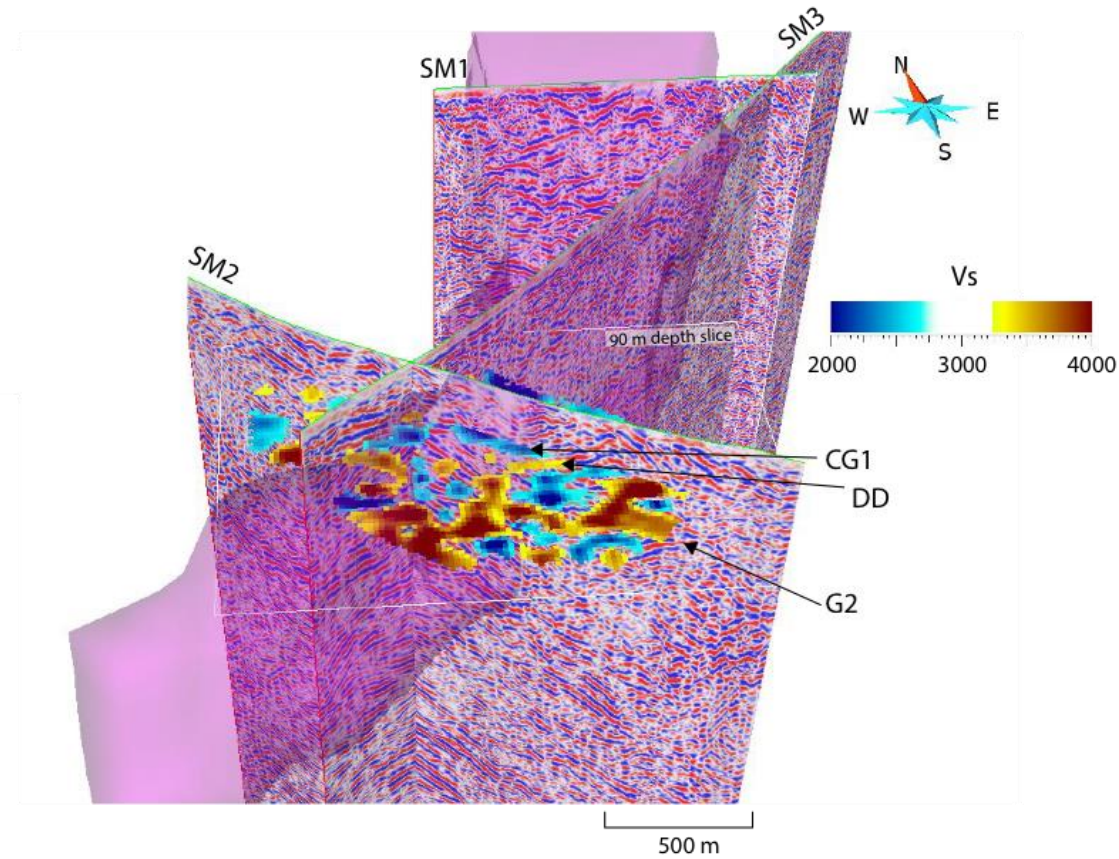

Figure 50. A plot of a horizontal section (90 m depth) of the 3D volume result of the tomography model obtained from the 3D seismic data by Da Col et al. (2019), displayed with the three active-source seismic profiles (SM1, SM2 and SM3) and the 3D carbonatite-glimmerite deposit from the previous geological model (provided by Yara). Observed features are labelled, CG1: Carbonatite-Glimmerite, G2: Granite on eastern side of deposit and DD: Possible diabase dike. (Viewing angles is to the N).

7.2 GPR and Magnetic Data

In this study, the seismic data was crucial for imaging the extent of the carbonatite-glimmerite. The additional geophysical measurements (GPR and magnetic) acquired along profile SM2, were also found to be beneficial for supporting and expanding on the interpretation.

GPR data acquired along profile SM2 proved to be valuable as it allowed for the interpretation to be brought to the surface. A connection was made in certain places between the reflections observed in GPR data with dipping reflectors in the seismic data. The reflection labelled DD1 in Figures 43 and 45 are interpreted as being the same

dipping feature based on their locations and orientation. The feature is possibly a diabase dike, based on the reflective behaviour.

A clear link can also be made between a dipping feature observed on GPR line 208 (DD3, Figure 45) and a dipping reflection observed in the near surface of seismic profile SM2 (DD3, Figure 43), even though there is a significant difference in the scale of the two datasets (Figure 51). This feature is interpreted as being a diabase dike based the physical property information. However, there is no borehole information in this area to confirm this interpretation.

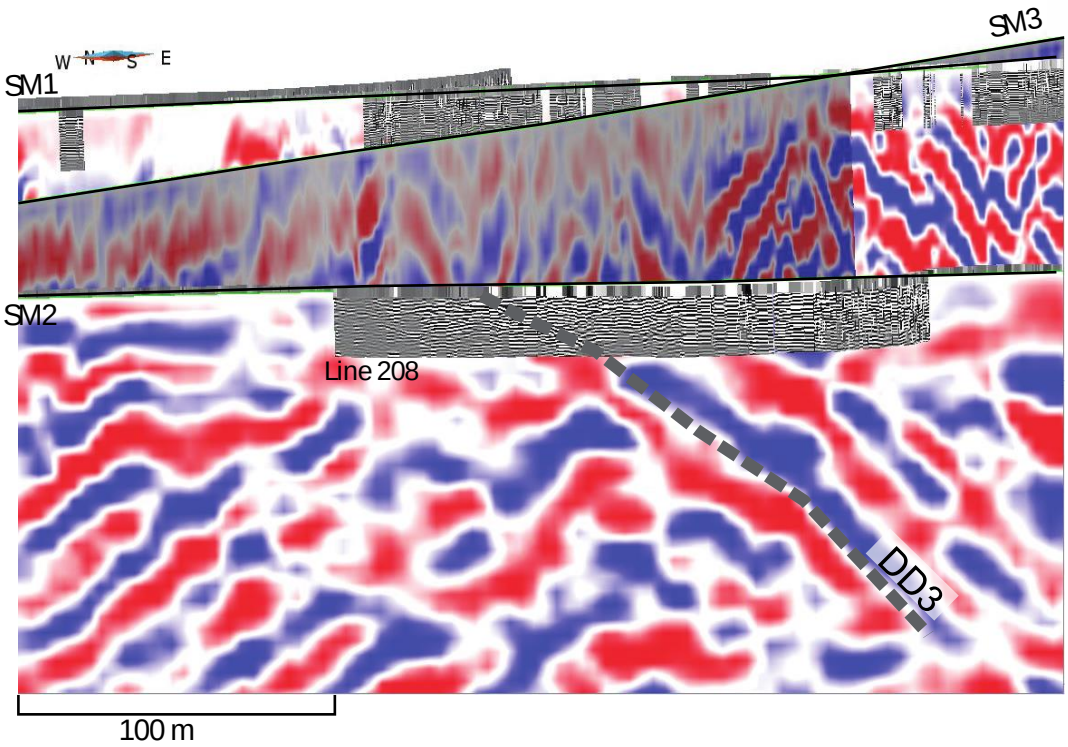

Figure 51. GPR results overlain on the seismic profiles. Dipping reflection (DD3) observed in both GPR profile 208 and seismic profile SM2.

The magnetic line (Figure 46), shows that carbonatite-glimmerite deposit is easily distinguishable from the lower values associated with the surrounding tonalite-diorite and gneiss, due it's magnetite content. The magnetic values increase towards the carbonatite-glimmerite deposit, as is observed in the aeromagnetic map (Figures 8 and 38). As can be seen in Figure 52, this trend is also seen in the magnetic data acquired along survey line

SM1 and in the area south of the Särkijärvi pit (Laakso, 2019). Magnetic measurements are therefore proven to be a good indicator for determining the boundaries of the carbonatite-glimmerite deposit.

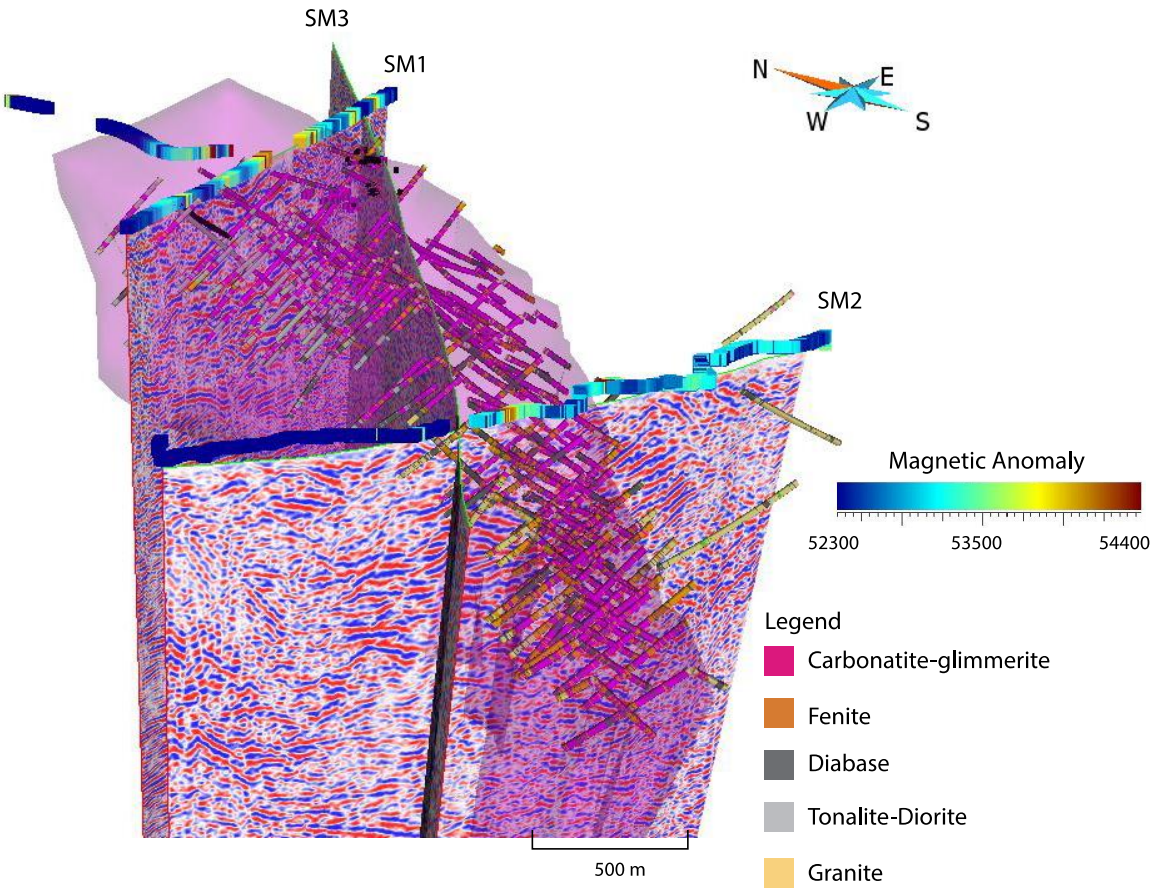

Figure 52. Magnetic lines along survey lines SM1 and SM2 and from the southern part of the main pit displayed with the 3 2D-active source seismic profiles. The carbonatite-glimmerite deposit from the previous geology model (provided by Yara) is overlain on the data. (View angles is towards the NE).

8 CONCLUSIONS

A new 3D model, illustrating the depth and lateral extent of the Siilinjärvi carbonatite-glimmerite deposit, was created based on the results obtained from the active-source reflection seismic data and borehole information. The new model shows that the southern end of the deposit is wider in comparison to what was previously depicted and it extends further towards the NW. The carbonatite-glimmerite deposit is distinguishable from the surrounding rocks due to the complex reflectivity pattern associated with the intruding diabase dike network. A contact was observed to the east of the deposit, between the carbonatite-glimmerite and fenite. The geology in the western side of the deposit was more chaotic, with alternating lithologies. This area was included in the new 3D model as it could not be separated based on the seismic signal. Several possible diabase dikes were detected in the reflection seismic and GPR data. Elevated magnetic total field values were associated with the carbonatite-glimmerite deposit. Information obtained from this study will be helpful to guide future drilling in the area.

Recommendations for future work include a GPR survey along the location of seismic line SM3. GPR data acquired along SM2 proved to be valuable in providing information in the near surface. Data quality along SM3 was inferior to that of SM2 and therefore, a GPR survey could provide further information on the subsurface. GPR data could also be utilised to improve on the statics models created during seismic processing. This was not executed as part of this work due to time constraints. Further physical property studies, which include dielectric property measurements, would also be beneficial for future studies.

Borehole information is limited in the areas along seismic line SM2. Deeper boreholes would be valuable for confirming the origin of the deeper reflections observed in the seismic profile.

The processing flow, which was used in this study for the seismic data, could be used as a good reference for future work. New methods and more innovative approaches to data processing could be developed and tested on this data. In particular, further work could be carried out in improving the statics models for both seismic lines, for enhancing the

signal-to-noise ratio of SM3 in particular, and also for suppressing the high-amplitude S-waves.

Acknowledgments

First and foremost, I would like to thank the Smart Exploration project for allowing me the opportunity to take part in this project and for funding this thesis. I am very thankful for having the privilege of working with such an amazing team during the field work period at the Siilinjärvi mine site. I would like to thank the staff at Yara, in particular Aleksi Salo and Mikko Savolainen, for making the survey possible. I would like to express the deepest appreciation and gratitude to my supervisors Emilia Koivisto and Pietari Skyttä for all their guidance and support. Thank you, Emilia for all your patience and encouragement throughout this process; I am grateful for your assistance from the start to the end of this thesis work. I would like to thank Alireza Malehmir and the Master's students at Uppsala University for providing me with magnetic data, making it possible for me to further my interpretation. Thank you to the software providers of Globe Claritas, ReflexW and GOCAD® for providing academic licenses, making it possible for me to complete this work. In particular, thank you to Andy Juniper from Globe Claritas for providing an additional license when access to the office was restricted due to Covid-19.

I would like to thank my friends and all my student associates for making my experience in Finland so amazing.

Finally, I would like to thank my family for all their love and support. Go raibh míle maith agaibh!

Smart Exploration has received funding from the European Union's Horizon 2020 research and innovation programme under grant agreement No. 775971.

References

Airo, M-L. 2005. Aerogeophysics in Finland 1972–2004: Methods, System Characteristics and Applications. Geological survey of Finland, Special Paper 39. 197 pp.

Annan, A., 2003. Ground Penetrating Radar Principles, Procedures & Applications. Sensors & Software Inc. Workshop notes, 286 p

Balestrini, F., Draganoy, D., Malehmir, A., Marsden, P. and Ghose, R. 2019. Improved target illumination at Ludvika mines of Sweden through seismic-interferometric surface-wave suppression. Geophysical prospecting.

Basu, A.R., Puustinen, K., 1982. Nd-isotopic study of the Siilinjärvi carbonatite complex, eastern Finland and evidence of early Proterozoic mantle enrichment. Geological Society of America. Abstracts with Programs 14 (7), 440.

Bayanova, T.B., 2006. Baddeleyite: a promising geochronometer for alkaline and basic magmatism. Petrologiya 14, 203–216.

Campbell, W. H., 2003. Introduction to geomagnetic fields. Cambridge University Press.

Carlsson, M., 2020. Mineralogical Characterisation and Petrographic Analysis of Fenites in the Northern Siilinjärvi Alkali Complex. MSc thesis, University of Helsinki.

Colombero, C., 2020, Extraction of surface-wave dispersion curves from ambient noise data in a mineral exploration site in Finland, EAGE Annual 82nd Conference and Exhibition.

Da Col, F., Papadopoulou, M., Koivisto, E., Sito, Ł., Savolainen, M. and Socco, L.V., 2020. Application of surface-wave tomography to mineral exploration: a case study from Siilinjärvi, Finland. Geophysical Prospecting, 68 (1-Cost-Effective and Innovative Mineral Exploration Solutions), pp.254-269.

Donczew, A., Malehmir, A., Koivisto, E., Savolainen, M. and Brodic, B. 2019. Mine Bench-Tunnel Seismic Data Acquisition for Characterizing Shear Zones in the Siilinjärvi Phosphate Mine, Finland. Conference paper: Near Surface Geoscience Conference & Exhibition 2019 8–12 September 2019, The Hague, Netherlands.

Dye, D. W., & Hartshorn, L. (1924). The dielectric properties of mica. Proceedings of the Physical Society of London, 37(1), 42.

European Commission. 2017a. Communication from the commission to the European parliament, the council, the European economic and social committee and the committee of the regions on the 2017 list of Critical Raw materials for the EU. COM/2017/0490 final. 8 pp.

European Commission. 2017b. Study on the review of the list of Critical Raw Materials. Critical Raw Materials Factsheets. Written by Deloitte Sustainability, British Geological Survey, Bureau de Recherches Géologigues et Minières, Netherlands Organisation for Applied Scientific Research. EU publication. 517 pp.

GLOBE Claritas. 2020. Seismic Processing Software. Webpages visited 15.04.2020. http://www.globeclaritas.com

Green, R., 1960. Remanent magnetization and the interpretation of magnetic anomalies. Geophysical Prospecting, 8(1), pp.98-110.

Hinze, W. J., Saad, A. H. & Von Frese, R. R. B. 2013. Gravity and Magnetic Exploration: Principles, Practices, and Applications. Cambridge University Press, Cambridge, 512 pp.

Jol, H. M. (Ed.)., 2008. Ground penetrating radar theory and applications. elsevier.

Kauti, T., Skyttä, P. and Savolainen, M. Manuscript in preparation. Assessment of the structural geometry of the complex dike network (Siilinjärvi, Finland) utilizing data integration and scalability. Implications for the spatial distribution of the dikes within the subsurface. (Working title).

Knight, R., 2001. Ground penetrating radar for environmental applications. Annu. Rev. Earth Planet. Sci. 29, 229–255.

Koivisto, E., Malehmir, A., Hellqvist, N., Voipio, T., & Wijns, C. (2015). Building a 3D model of lithological contacts and near-mine structures in the Kevitsa mining and exploration site, Northern Finland: constraints from 2D and 3D reflection seismic data. Geophysical Prospecting, 63(Hard Rock Seismic imaging), 754-773.

Kouvo, O., 1984. GTK internal report to H. Lukkarinen 4p.

Kukkonen, I. T., Heinonen, S., Heikkinen, P., & Sorjonen-Ward, P., 2012. Delineating ophiolite-derived host rocks of massive sulfide Cu-Co-Zn deposits with 2D high-resolution seismic

reflection data in Outokumpu, Finland Ophiolite-derived massive sulfide host rocks. Geophysics, 77(5), WC213-WC222.

Laakso, V., 2019. Testing of Reflection Seismic, GPR and Magnetic Methods for Mineral Exploration and Mine Planning at the Siilinjärvi Phosphate Mine Site in Finland. MSc thesis, University of Helsinki.

Luoma, S., Majaniemi, J., Kaipainen, T., & Pasanen, A. (2016). GPR survey and field work summary in Siilinjärvi mine during July 2014. Geological Survey of Finland. Archive report, 66.

Maijala, P., 1991. Maatutkaluotausaineisto ja sen käsittely. Oulun yliopisto, Geofysiikan laitos. Master thesis. 120 p. In Finnish.

MALÅ GPR Australia. 2009-2017. MALÅ ProEx system – Modular full-range Ground Penetrating Radar (GPR) system for the advanced professional user. Webpages visited 08.03.2020. https://www.malagpr.com.au/mala-professional-explorer.html.

Malehmir, A., Bellefleur, G., Koivisto, E., & Juhlin, C. (2017). Pros and cons of 2D vs 3D seismic mineral exploration surveys. First Break, 35(8), 49-55.

Malehmir, A., Heinonen, S., Dehghannejad, M., Heino, P., Maries, G., Karell, F., ... & Salo, A. (2017). Landstreamer seismics and physical property measurements in the Siilinjärvi open-pit apatite (phosphate) mine, central Finland. Geophysics, 82(2), B29-B48.

Malehmir, A., Holmes, P., Gisselø, P., Socco, L.V., Carvalho, J., Marsden, P., Verboon, A.O. and Loska, M. 2019. Smart Exploration: Innovative ways of exploring for the raw material in the EU. 81st EAGE Conference & Exhibition 2019. 3–6 June 2019, London, UK.

Malehmir, A., Juhlin, C., Wijns, C., Urosevic, M., Valasti, P., & Koivisto, E., 2012. 3D reflection seismic imaging for open-pit mine planning and deep exploration in the Kevitsa Ni-Cu-PGE deposit, northern Finland. Geophysics, 77(5), WC95-WC108.

Manzi, M., Cooper, G., Malehmir, A., Durrheim, R., & Nkosi, Z., 2015. Integrated interpretation of 3D seismic data to enhance the detection of the gold-bearing reef: Mponeng Gold mine, Witwatersrand Basin (South Africa). Geophysical Prospecting, 63(Hard Rock Seismic imaging), 881-902.

Neal, A. and Roberts, C.L., 2000. Applications of ground-penetrating radar (GPR) to sedimentological, geomorphological and geoarchaeological studies in coastal environments. Geological Society, London, Special Publications, 175(1), pp.139-171.

O'Brien, H., Heilimo, E., & Heino, P. 2015. The Archean Siilinjärvi carbonatite complex. In: Wolfgang, D. M., Lahtinen, R. and O'Brien, H. (Eds.) Mineral deposits of Finland. Elsevier, 327–343.

Olhoeft, G. R., 1981. Electrical properties of rocks. Physical properties of rocks and minerals, 2, 257-297.

Orica Limited. 2019. Uni tronicTM 600 Detonator. Webpages visited 17.10.2019. http://www.oricaminingservices.com/fi/fi/product/products_and_services/electronic_blasting_systems/uni_tronic_600/uni_tronic_600_detonator/1365.

Papadopoulou, M., Da Col, F., Mi, B., Bäckström, E., Marsden, P., Brodic, B., Malehmir, A. and Socco, V. 2019. Surface-wave analysis for static corrections in mineral exploration: a case study from central Sweden. Geophysical prospecting.

Pasanen, A., 2009. Radar stratigraphy of the glaciotectonically deformed deposits in the Isoniemi area, Haukipudas, Finland. Bulletin of the Geological Society of Finland 81, 39–51.

Pretorious, C.C., Muller, M.R., Larroque, M., and Wilkins, C. 2003. A Review of 16 Years of Hardrock Seismics on the Kaap- vaal Craton. In Hardrock seismic exploration. Edited by D.W. Eaton, B. Milkereit, and M.H. Salisbury. Society of Exploration Geophysicists, Tulsa, Okla., pp. 247–268.

Pretorius, C. C., and W. F. Trewick, 1997, Application of 3D seismics to mine planning at Vaal Reefs Gold Mine, number 10 shaft, Republic of South Africa: Proceedings of Exploration 97: Fourth Decennial Interna- tional Conference on Mineral Exploration, Prospecting and Development Associates of Canada, 399–408.

Pretorius, C.C., Trewick, W.F., Fourie, A. and Irons, C., 2000. SEISMIC, ELECTROMAGNETICS, AND PHYSICAL PROPERTY STUDIES-Application of 3-D siesmic to mine planning at Vaal Reefs gold mine, number 10 shaft, Republic of South Africa. Geophysics, 65(6), pp.1862-1870.

Pretorius, CC., Chunnett, GK, Chalke, TWJ., Gibson, M. 2007. 3D data integration for Exploration and Mine Planning: Proc. of Exploration 07: 5th Decennial International Conference on Mineral Exploration, Prospectors and Developers Association of Canada.

Puustinen, K., 1971. Geology of the Siilinjärvi carbonatite complex, Eastern Finland. Bulletin of the Geological Society of Finland 249, 1–43.

Reynolds, J.M., 2011. An introduction to applied and environmental geophysics. John Wiley & Sons.

Robinson, D.A., Jones, S.B., Wraith, J.M., Or, D. and Friedman, S.P., 2003. A Review of Advances in Dielectric and Electrical Conductivity Measurement in Soils Using Time Domain Reflectometry. Published in Vadose Zone Journal 2, 444–475.

Sadiku, M., 2014. Elements of electromagnetics, 6th edition. Oxford University Press, 896 p.

Sandmeier geophysical research. 2020. Reflexw – GPR and seismic processing software.

Webpages visited 14.06.2020. https://www.sandmeier-geo.de/reflexw.html.

Salisbury, M., Milkereit, B. and Bleeker, W. 1996. Seismic imaging of sulfide deposits: Part I. Rock properties. Economic Geology. 91, 821–828.

Salisbury, M., Snyder, D., & Goodfellow, W. D., 2007. Application of seismic methods to mineral exploration. Mineral deposits of Canada: A synthesis of major deposit types, district metallogeny, the evolution of geological provinces, and exploration methods: Geological Association of Canada, Mineral Deposits Division, Special Publication, 5, 971-982.

Sandmeier, K., J., 2011. REFLEXW manual, version 9.0.

Schön, J., 2011. Chapter 10- Magnetic Properties. Physical properties of rocks: A workbook. Elsevier, Oxford, 373-381.

Sercel. 2020. UNITE cable-free seismic aquisition. Webpages visited 08.06.2020. https://www.sercel.com/products/Pages/unite.aspx.

Sheriff, R.E. 1975. Factors affecting Seismic Amplitudes. Geophysical prospecting. 23, 125–138.

Sheriff, R. E., & Geldart, L. P., 1995. Exploration seismology. Cambridge university press.

Shuey, R. T., 1985. A simplification of the Zoeppritz equations. GEOPHYSICS50, 609-614.

Smart Exploration, 2020. Webpages visited 05.06.2020. https://smartexploration.eu

Taner et al., 1974, Taner, M. T., Koehler, F., and Alhilali, K. A., 1974, Estimation and correction of near-surface time anomalies: Geophysics, 41, 441–463.

Tichomirowa, M., Grosche, G., Götze, J., et al. 2006. The mineral isotope composition of two Precambrian carbonatite complexes from the Kola alkaline province—alteration versus primary magmatic signatures. Lithos 91, 229–249.

Wright, C., Wright, J. A., & Hall, J. (1994). Seismic reflection techniques for base metal exploration in eastern Canada: Examples from Buchans, Newfoundland. Journal of Applied Geophysics, 32(2-3), 105-116.

Yara Suomi Oy, 2019. Webpage visited 10.09.2020. https://www.kaivosvastuu.fi/en/yrityskortti/yara-suomi-oy/

Yilmaz, Ö. 2001. Seismic data analysis: Processing, inversion, and interpretation of seismic data. Volume 1–2. 2. Edition. Society of Exploration Geophysicists, Tulsa, 2065 pp.

Zozulya, D.R., Bayanova, T.B., Serov, P.N., 2007. Age and isotopic geochemical characteristics of Archaean carbonatites and alkaline rocks of the Baltic shield. Doklady Earth Sciences 415A (6), 874–879.